

# A Search for $ZH$ Production in $p\bar{p}$ Collisions at $\sqrt{s} = 1.96$ TeV with the Full Pass2 Data Set.

## Version 5.7

J. Heinmiller, A. Stone, and N. Varelas

December 5, 2006

### Abstract

This note describes a search for a standard model Higgs boson produced in association with a  $Z$  boson through the decay mode  $ZH \rightarrow e^+e^- + b\bar{b}$  in  $p\bar{p}$  collisions at  $\sqrt{s} = 1.96$  TeV at the Fermilab Tevatron Collider. The data sample used in this analysis corresponds to  $452 \text{ pb}^{-1}$  of integrated luminosity accumulated by the DØ detector. Good agreement between data and standard model predictions is observed using single or double tagged samples. A 95% C.L. upper limit of the  $\sigma(p\bar{p} \rightarrow ZH) \times \text{BR}(H \rightarrow b\bar{b})$  is set as 3.2-8.2 pb for Higgs Masses of 105 to 145 GeV.

## 1 Introduction

The second most sensitive production channel at the Tevatron for a Higgs mass below 140 GeV is the associated production of a Higgs boson with a  $Z$  boson. The  $Z$  boson decays into hadrons  $69.81 \pm 0.02\%$  [1] of the time, but this four jet event (assuming  $H \rightarrow b\bar{b}$ ) is overwhelmed by multi-jet production. A search for  $ZH$  production in the  $\nu\nu b\bar{b}$  decay channel, the next largest branching ratio, using  $260 \text{ pb}^{-1}$  of data has been performed [2]. We present the first results of  $ZH \rightarrow e^+e^- b\bar{b}$  channel using the entire corrected Pass2 data set, corresponding to an integrated luminosity of  $452 \text{ pb}^{-1}$ . Two electrons identifying the  $Z$  boson and two jets with one or two jets being b-tagged are required. The dominant backgrounds to  $ZH$  production is  $Zb\bar{b}$ ,  $Zjj$  (light-jet mistags), and  $t\bar{t}$ . No excess of events is observed in data and cross section exclusion limits are derived.

## 2 Data

### 2.1 Data

The Pass2 EM1TRK dataset used for this analysis was collected between April 2002 (Run 151,817) and August 2004 (Run 196,584). Events in this analysis were recorded using highly efficient, unscaled, single high- $p_T$  triggers which capitalized on the two electrons decaying from the  $Z$  boson. Each raw data event was reconstructed using the p14 version of the DØ reconstruction software with version 2 of the TMB fixer applied, and then skimmed down into the EM1TRK skim. The 64 million events entering the EM1TRK skim have: at least one object with  $ID = 10$  or  $\pm 11$ ,  $p_T > 8$  GeV, and a track object with  $p_T > 5$  GeV within  $\Delta\phi$  of 0.1 of one of the selected EM objects. Athena [3] p16.06.00 with d0correct tag p16-br-07 v8.2 and JES v5.3 was used to produce the analysis root-tuples. Using the run quality database, runs for which the SMT, CFT, and Calorimeter subsystems were flagged as “bad” were excluded from the analysis. Events that were flagged as “bad” by the luminosity or CalJetMet group were excluded by LBN (luminosity block number). Runs in which the L1Cal trigger coverage was  $|\eta_{detector}| < 0.8$  (pseudorapidity) were excluded. Events which passed the  $Z$  boson invariant mass cuts but failed calorimeter event quality were removed by their LBN. The primary vertex is required to be within  $\pm 60$  cm of the detector center along the beam pipe (z-axis). The triggers are grouped into similar trigger requirements and periods of time: v8–10, v11, v12, and v13 trigger lists. The trigger efficiency was studied using the trigger mapping scheme as shown in Table 1.

The trigger names are defined in Table 2. A reconstructed electron object passes a trigger if the object passes all three trigger levels. The reconstructed electron object passes the Level 1 requirement if there is a trigger tower within  $\Delta R = \sqrt{(\Delta\phi)^2 + (\Delta\eta)^2} < 0.4$ , using detector coordinates, and the trigger tower has enough electromagnetic energy to pass the Level 1 threshold. Similarly, L2 and L3 trigger objects need to be above the trigger threshold and within  $\Delta R < 0.4$  of the reconstructed electron. Using these triggers, the measured luminosity is  $L = 452$  with a 6.5% uncertainty [4].

Trigger Name
E1_SHT20   E2_SHT20   E3_SHT20   E1_SH30 all unrescaled
E1_SHT20   E2_SHT20   E1_SH30 all unrescaled
E1_SHT20   E1_SH30 all unrescaled
E1_SHT20
E1_SHT22   E2_SHT22   E3_SHT22   E1_SH30 all unrescaled
E1_SHT22   E2_SHT22   E1_SH30 all unrescaled
E1_SHT22   E1_SH30 all unrescaled
E1_SHT22
EM_HI_SH   EM_HI_2EM5_SH all unrescaled
EM_HI_SH
EM_HI
EM_MX_SH
EM_MX

Table 1: Unrescaled single high  $p_T$  electron trigger map. This map is used to select triggered events and to determine trigger efficiencies, based on which triggers were unrescaled during data taking periods. The first line indicates that if an event has all four of these triggers unrescaled, then check if any of the four triggers pass their individual trigger requirements (L1, L2, and L3). If any of the four triggers pass, the event is kept in the analysis. The second line is missing the E3\_SHT20 requirement, which fires more often than the other three due to its lower threshold requirement. Therefore, this table actually has an “and” between all of the triggers in the same row, based on being unrescaled, and then once a row is chosen, this table has an “or” between the all triggers in the same row to see if the event makes it into the analysis.

Trigger	L1	L2	L3
E1_SHT20	CEM(1,11)	EM(1,15) v13 only	ELE_NLV_SHT(1,20)
E2_SHT20	CEM(2,6)	EM(1,15) v13 only	ELE_NLV_SHT(1,20)
E3_SHT20	CEM(1,9)CEM(2,3)	EM(1,15) v13 only	ELE_NLV_SHT(1,20)
E1_SH30	CEM(1,11)	EM(1,15) v13 only	ELE_NLV_SH(1,30)
E1_SHT22	CEM(1,11)	EM(1,15)	ELE_NLV_SHT(1,22)
E2_SHT22	CEM(2,6)	EM(1,15)	ELE_NLV_SHT(1,22)
E3_SHT22	CEM(1,9)CEM(2,3)	EM(1,15)	ELE_NLV_SHT(1,22)
EM_HI_SH	CEM(1,10)	EM(1,12)	ELE_LOOSE_SH_T(1,20)
EM_HI_2EM5_SH	CEM(2,5)	EM(1,12)	ELE_LOOSE_ST_T(1,20)
EM_HI	CEM(1,10)	EM(1,12)	ELE_LOOSE(1,30)
EM_MX_SH	CEM(1,15)	none	ELE_LOOSE_SH_T(1,20)
EM_MX CEM	CEM(1,15)	none	ELE_LOOSE(1,30)

Table 2: Single high  $p_T$  electron triggers used in this analysis. The CEM(1,11) term is defined as requiring one electromagnetic trigger tower  $0.2 \eta \times 0.2 \phi$ , and as having at least 11 GeV of transverse energy. The EM(1,15) term is defined as requiring two electromagnetic trigger towers side by side in either  $\eta$  or  $\phi$  and as having at least 15 GeV of transverse energy. The ELE\_NLV\_SHT(1,20) term is defined as requiring a cone of electromagnetic trigger towers within  $0.25$  and as having at least 20 GeV of transverse energy [8].

### 3 Event Selection

This analysis is based on the selection of events with two electrons of  $p_T > 20$  GeV, an invariant mass of the two electrons between 75 and 105 GeV, and at least two jets with  $p_T > 20$  GeV (after jet energy scale correction). The electrons are required to be within  $|\eta_{detector}| < 2.5$  and outside the inter-cyostat region of  $1.1 < |\eta_{detector}| < 1.5$ , with at least one electron in the central region of the detector  $|\eta_{detector}| < 1.1$ , and to have at least one track match. The jets are required to be within  $|\eta| < 2.5$  and  $|\Delta R_{jet,electron}| > 0.50$  from the two electrons. The primary vertex is required to be within  $\pm 60$  cm of the detector center along the beam pipe (z-axis).

#### 3.1 Electrons

Electromagnetic objects in the analysis have to satisfy the following requirements:

- ID = 10 or  $\pm 11$ ;
- EM Fraction  $> 0.9$ ;
- Isolation  $< 0.15$ ;
- $\chi^2$  of H-Matrix(7)  $< 12$  if  $|\eta_{detector}| < 1.1$ ;
- $\chi^2$  of H-Matrix(7)  $< 20$  if  $1.5 < |\eta_{detector}| < 2.5$ ;
- $p_T > 20$ ;
- No fiducial restrictions in  $\phi$ ;
- At least one electron is  $|\eta_{detector}| < 1.1$ ;
- At least one electron with a track match  $P(\chi^2) > 0.01$  (using  $\Delta\phi$ ,  $\Delta\eta$ , and  $E/p$ ).

Figure 1 shows the comparison of the  $\chi^2$  H-matrix 7 and 8 for the same electrons in the central region. Figure 2 shows the comparison of  $\chi^2$  H-matrix 7 and 8 for the same electron in the forward region. The forward region shows equivalent values of  $\chi^2$  H-matrix 7 and 8. The amount of QCD+Drell-Yan background contamination using  $\chi^2$  H-matrix 7 or 8 was comparable.

#### 3.2 Jets

The Run II cone algorithm jets [15] with a radius of  $R = 0.5$  in  $\eta$  and  $\phi$  quality requirements are:

- $p_T > 20$  GeV (after JES correction);
- $|\eta| < 2.5$ ;
- $0.05 < \text{EMfraction} < 0.95$ ;

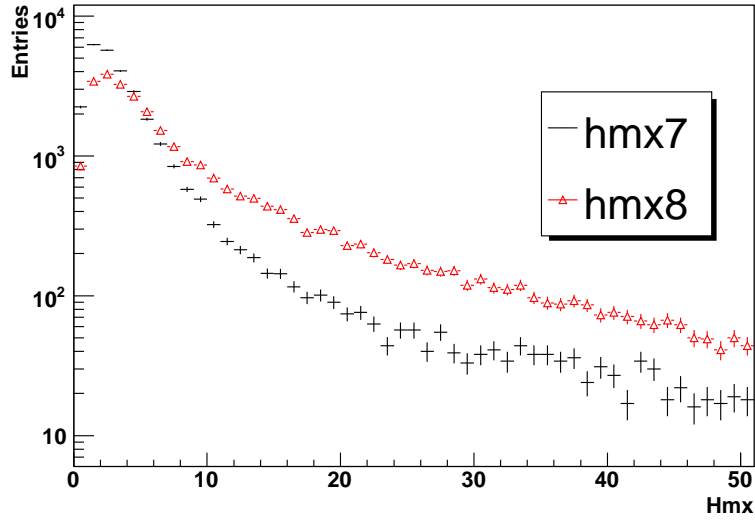


Figure 1: H-Matrix 7 and 8 distributions for reconstructed electrons in the central region of the calorimeter ( $|\eta_{detector}| < 1.1$ ). The cut on H-Matrix 7 in the central region is 12.

- coarse hadronic fraction  $< 0.4$ ;
- hot fraction (leading tower  $E_T$  / second leading tower  $E_T$ )  $< 10$ ;
- n90 (number of towers making 90% of the energy)  $> 1$ ;
- Confirmation of jets using Level 1 trigger towers. L1 trigger confirmation is based on a comparison of the energies in the EM and fine hadronic precision readout with the energies from L1 trigger electronics. For the jest to pass L1 confirmation, the ratio of the tower energy in L1 to the jet  $p_T$  must be  $> 0.2$  in the ICR region, and  $> 0.4$  in the other regions.;
- $\Delta R > 0.50$  between jet and electron decaying from the  $Z$  boson.

### 3.3 Taggable Jets

Jet “taggability” is a track confirmation quality cut needed to have stable b-tagging performance. To be taggable, a jet is required to be matching within 0.5 in  $\Delta R$  with a “track jet” which is reconstructed using a simple cone clustering algorithm of  $\Delta R = 0.5$  on tracks satisfying:

- at least one seed track with  $p_T > 1$  GeV;
- at least one or more tracks with  $p_T > 0.5$  GeV;
- tracks have at least 1 SMT hit (defined as SMT ladders + F disk wedges);
- track dca (distance of closest approach in x-y plane)  $< 0.2$  cm;

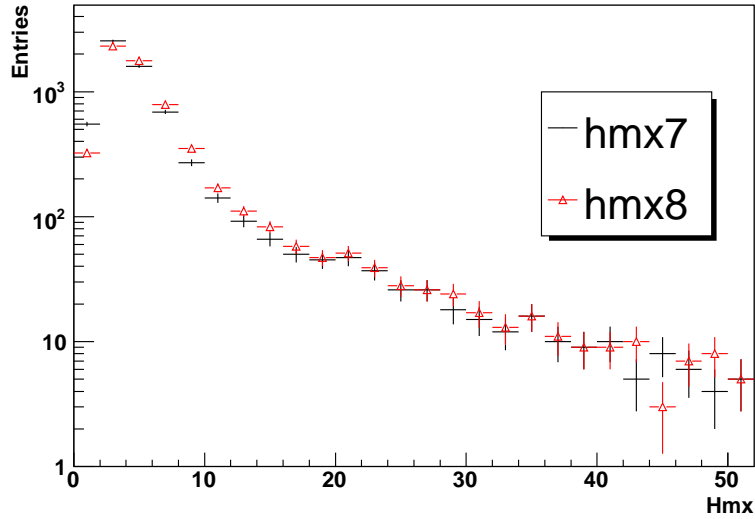


Figure 2: H-Matrix 7 and 8 distributions for reconstructed electrons in the forward region of the calorimeter ( $1.5 < |\eta_{detector}| < 2.5$ ). The cut on H-Matrix 7 in this forward region is 20. Unlike the central region of the calorimeter, H-Matrix 7 and 8 of the electrons are nearly identical in the forward region.

- track zdca (distance of closest approach along the Z axis)  $< 0.4$  cm;
- $\Delta z < 2.0$  cm to the current track-jet z position (the track-jet direction and z position are updated upon the addition of each track).

### 3.4 B Tagging

In order to distinguish  $Zb\bar{b}$  and  $ZH$  candidates from  $Z + 2$  light quark-jet events, the certified p14 pass2 jes 5.3 JLIP algorithm [29] is used to tag b-jets. The JLIP algorithm utilizes a “jet lifetime probability”, which is constructed from the tracks associated with jets that have positive impact parameters in the transverse plane. The sign of the impact parameter is defined by the scalar product  $\vec{d}_{perigee} \cdot \vec{p}_{T(jet)}$ , where  $\vec{d}_{perigee}$  is the distance vector in the transverse plan between the primary vertex and the point that defines the impact parameter. JLIP gives the probability that a jet originated from a light quark jet (u,d,s), therefore very low JLIP probability values are highly likely to originated from b quarks.

## 4 Monte Carlo

Simulated Monte Carlo (MC) samples were used to estimate signal acceptance and the total expected background. Instrumental background is estimated separately from the data. Table 4 lists the cross sections of the signal and background samples used in this analysis. Next-to-leading order (NLO) MCFM [9] [10] cross sections were used for the ALPGEN [13] + PYTHIA [33] samples. PYTHIA generated WZ and ZZ inclusive NLO/LO K-factors were used [11]. PYTHIA generated ZH signal samples have a NLO/LO K-factor = 1.26 applied

[12]. The Zbb cross section was obtained at NLO using the MCFM program version 4.1 with CTEQ6M pdfs. The ALPGEN+PYTHIA Zjj has a Zbb contribution excluded from the analysis. The simulated background is normalized according to the cross section. The normalization factor is  $L_{data}/L_{mc}$  or  $L_{data} \cdot \sigma_{MC}/$  (initial number of simulated events). The ALPGEN+PYTHIA Zjj cross section was normalized so the total number of simulated events equalled the total number of events in data after the selection of the Z boson candidates with two or more jets ( $Z + \geq 2j$ ). After the  $Z + \geq 2j$  selection cut, Zjj is the dominate process, therefore any mismatch in the number of simulated events compared to data is due to the Zjj process. Since the full response of the detector is not well modeled in the MC, scale factors for electrons, tracks, jets, taggability, and b tagging are applied. Instead of weighting each event by the event scale factors, physics objects are randomly removed based on their scale factor. Since every scale factor is between 0 and 1, a random number is generated for each physics object, and if the random number is larger than the scale factor value, the physics object is dropped from the simulated event.

Process	Generator	$\sigma \times B$ (pb)	number of events	SAM request ID
$ZH \rightarrow e\bar{e}b\bar{b}(M_H = 105GeV)$	PYTHIA	0.0040	5000	11661
$ZH \rightarrow e\bar{e}b\bar{b}(M_H = 115GeV)$	PYTHIA	0.0028	5000	11662
$ZH \rightarrow e\bar{e}b\bar{b}(M_H = 125GeV)$	PYTHIA	0.0018	5000	11663
$ZH \rightarrow e\bar{e}b\bar{b}(M_H = 135GeV)$	PYTHIA	0.0011	5000	11664
$ZH \rightarrow e\bar{e}b\bar{b}(M_H = 145GeV)$	PYTHIA	0.0005	5000	11665
$Zbb \rightarrow e\bar{e}b\bar{b}$	ALPGEN+PYTHIA	0.513	98000	11407 11408
$t\bar{t} \rightarrow 2b + 2l$	ALPGEN+PYTHIA	0.671	154000	16157 16158 16159
$t\bar{t} \rightarrow 2b + 1l + 2j$	ALPGEN+PYTHIA	2.676	314050	15325 15326 15344-14346
$ZZ_{incl}$	PYTHIA	1.56	107000	15528 21609
$WZ_{incl}$	PYTHIA	3.68	203250	21607 21608
$Zjj \rightarrow e\bar{e}jj$	ALPGEN+PYTHIA	29.4	272450	10717 – 10720
				13855 – 13858
				13860 14177
$Z \rightarrow e\bar{e} + X$	PYTHIA	266.7	400000	12018
				120298 – 12030

Table 3: Summary of Monte Carlo samples used in this analysis.

Since the resolution of the electrons in data is not correctly described by the MC simulation, additional energy smearing is applied to the MC electrons. The  $p_T$  (as well as px, py, pz, and energy) of the electrons is replaced by  $p_T \rightarrow p_T \cdot c \cdot \text{Gauss}(1, f)$  where Gauss(1, f) is the smearing parameter which is randomly chosen from a Gaussian distribution with mean of 1 and a width of  $f \cdot c$  as an overall calibration factor. For this analysis the following values were used for central electrons  $|\eta_{detector}| < 1.1$  [17]:

- $f = 0.045$ ;
- $c = 1.003$ .

The following values were used for the forward electrons  $|\eta_{detector}| > 1.1$ :

- $f = 0.034$ ;
- $c = 0.996$ .

Since the resolution of jets in data is not correctly described by the MC simulation, additional jet resolution smearing is applied to the MC jets [18]. Equation 1 shows the resolution parameterization where  $N$ ,  $S$ , and  $C$  denote the noise, sampling, and constant terms, respectively.

$$\frac{\sigma(p_T)}{p_T} = \sqrt{\frac{N^2}{p_T^2} + \frac{S^2}{p_T} + C^2}. \quad (1)$$

Table 4 summarizes all coefficients for different detector regions. Using the  $p_T$  and  $\eta_{detector}$  of the MC jets, the data and MC resolutions are calculated. For a given jet, if the data resolution is better than the MC resolution, no additional smearing is applied. If the resolution is worse in data than in MC, a multiplicative smearing factor (Equation 2) is applied to the  $p_T$  of the jet.

$$\text{Smearing Factor} = Gauss\left(1, \sqrt{\left(\frac{\sigma(p_T)}{p_T}\right)_{data}^2 - \left(\frac{\sigma(p_T)}{p_T}\right)_{MC}^2}\right). \quad (2)$$

Coefficient	$ \eta_{det}  < 0.5$	$0.5 <  \eta_{det}  < 1.0$	$1.0 <  \eta_{det}  < 1.5$	$ \eta_{det}  > 1.5$
$N_{data}$	5.05	$9.06 \cdot 10^{-9}$	2.24	6.42
$S_{data}$	0.753	1.2	0.924	$4.5 \cdot 10^{-10}$
$C_{data}$	0.0893	0.087	0.135	0.0974
$N_{MC}$	4.26	4.61	3.08	4.83
$S_{MC}$	0.658	0.621	0.816	$5.13 \cdot 10^{-7}$
$C_{MC}$	0.0436	0.0578	0.0729	0.0735

Table 4: Jet resolution parameters in data and MC [18].



## 4.1 Trigger Efficiencies

The trigger efficiency per electron is studied with a tag-and-probe method using  $Z$  boson candidate events with an invariant mass between 70 and 110 GeV. For this method, both  $Z$  candidate electrons are considered as possible “tags”. An electron becomes a “tag” if it passes the trigger requirements for a given trigger which fired the event. Both tag and probe electrons must satisfy the following requirements:

- $p_T > 20$  GeV;
- EM Fraction  $> 0.9$ ;
- Isolation  $< 0.15$ ;
- $\chi^2$  of H-Matrix(7)  $< 12$  if  $|\eta_{detector}| < 1.1$ ;
- $\chi^2$  of H-Matrix(7)  $< 20$  if  $1.5 < |\eta_{detector}| < 2.5$ ;
- Track match with  $P(\chi^2) > 0.01$  (using  $\Delta\phi$ ,  $\Delta\eta$ , and  $E/p$ ).

The trigger efficiency is then measured on the probe electron. An efficient probe electron has trigger objects within  $\Delta R < 0.4$  and above their energy thresholds. The trigger efficiencies for various inclusive jet multiplicities, after QCD subtraction, are shown in Table 5. The trigger efficiency curves are in Figures 5 through 9. The trigger efficiency applied to MC is the “combined” efficiency, using v8 through v13. The combined efficiency has an average value of 95% for one of the  $Z$  boson electrons. The trigger efficiencies were measured as a function of jet multiplicity and are summarized in Table 5, Figure 3, and Figure 4. Since the trigger versions 8 to 10 only make up about  $50 \text{ pb}^{-1}$  of the  $452 \text{ pb}^{-1}$  of collected data, this 4% drop in efficiency (at higher jet multiplicities) has a negligible contribution. A 1-dimensional (1D) parameterization curve was made for electrons with  $|\eta_{detector}| < 1.1$  and a 2-dimensional (2D) parameterization ( $p_T, \eta$ ) for the forward electrons. Figure 5 shows a representative fit to the electron  $p_T$  spectrum. Figure 9 displays how well the parameterization curves, applied to the probe electron, match to the measured efficiency. The parameterization curves applied to the MC were determined from the inclusive  $Z$  sample. The single object trigger efficiency for  $Z$  with 0 or more jets ( $Z+ \geq 0j$ ) falls within the statistical uncertainty of the efficiency for  $Z+ \geq 2j$ . Since there are two electrons coming from the  $Z$  boson, event trigger efficiency is evaluated by Equation 3 yielding an overall combined event trigger efficiency of  $\sim 100\%$ .

$$\epsilon_{trigger} = \epsilon_1 \cdot (1 - \epsilon_2) + \epsilon_2 \cdot (1 - \epsilon_1) + \epsilon_1 \cdot \epsilon_2. \quad (3)$$

The trigger efficiency uncertainty was calculated by adding together the statistical and systematic uncertainty. The statistical event uncertainty was found to be 0.1%. One systematic uncertainty was measured by turning off the track match requirement for the probe electron. The average efficiency was lower by 0.2%. Another systematic uncertainty was estimated to be 1% from the uncertainty in the measurement of the efficiency of the  $Z+ \geq 2j$  sample. The three uncertainties are added in quadrature, propagated through the analysis code by raising and lowering the combined trigger efficiency, and give an uncertainty on the measurement of 1% for the amount of signal and background events passing all the selection cuts.

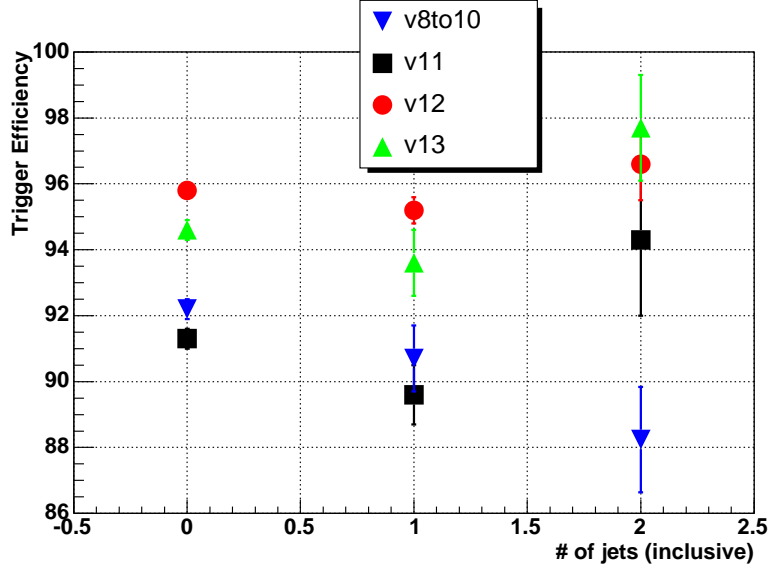


Figure 3: Trigger efficiencies as a function of jet multiplicity.

Trigger Version	$\geq 0$ jets	$\geq 1$ jet	$\geq 2$ jets
v8to10	$92.2 \pm 0.3$	$90.7 \pm 1.2$	$88 \pm 4$
v11	$91.3 \pm 0.4$	$89.6 \pm 1.3$	$94 \pm 3$
v12	$95.8 \pm 0.1$	$95.2 \pm 0.4$	$97 \pm 1$
v13	$94.6 \pm 0.3$	$93.6 \pm 1.0$	$98 \pm 2$
Combined	$95.0 \pm 0.1$	$93.4 \pm 0.4$	$95 \pm 1$

Table 5: Average trigger efficiencies with respect to trigger version and jet multiplicity.

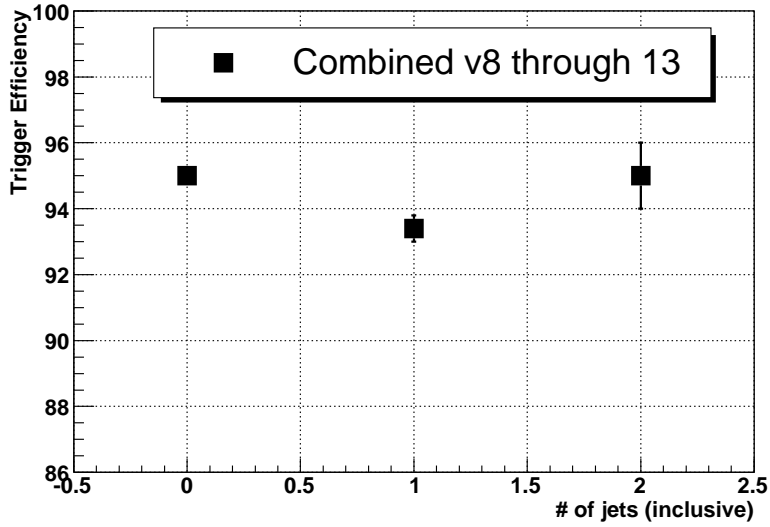


Figure 4: Trigger efficiencies as a function of jet multiplicity for the combined data sample.

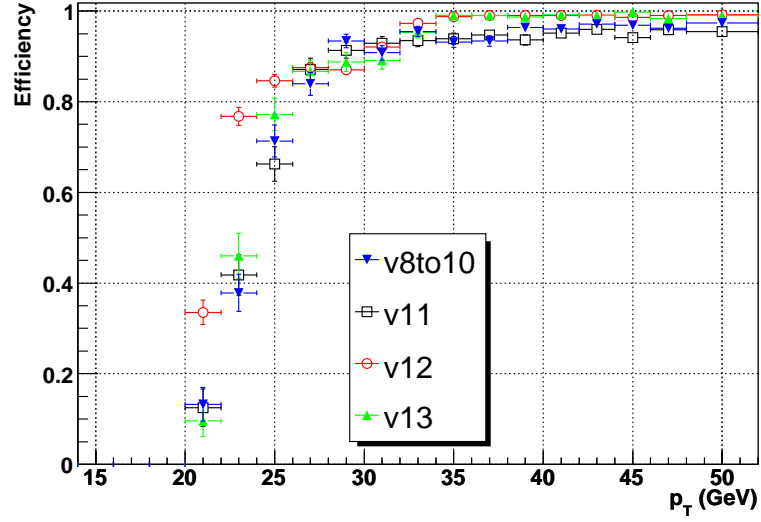


Figure 5: Trigger efficiencies vs electron  $p_T$  with zero or more jets in each event for different versions of the trigger.

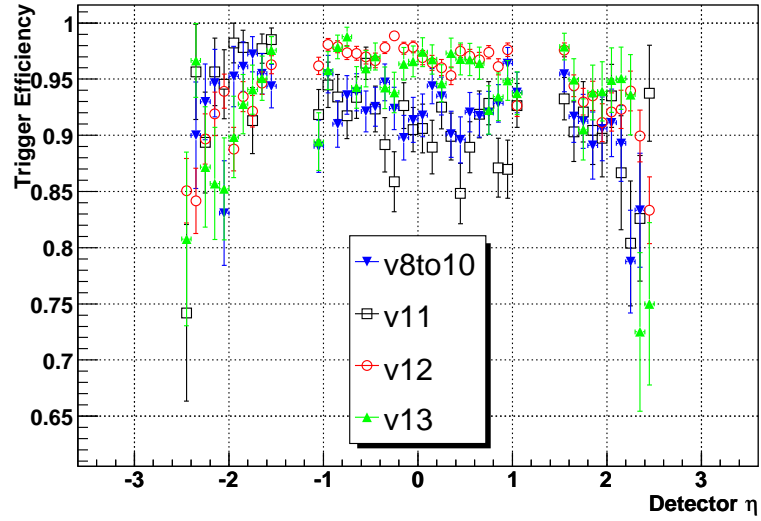


Figure 6: Trigger efficiencies vs electron  $\eta_{detector}$  with zero or more jets in each event for different trigger versions.

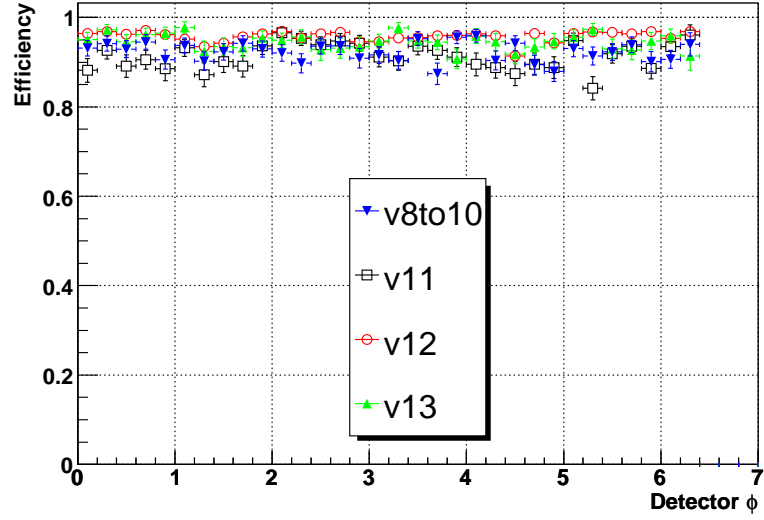


Figure 7: Trigger efficiencies vs electron  $\phi_{detector}$  with zero or more jets in each event for different trigger versions.

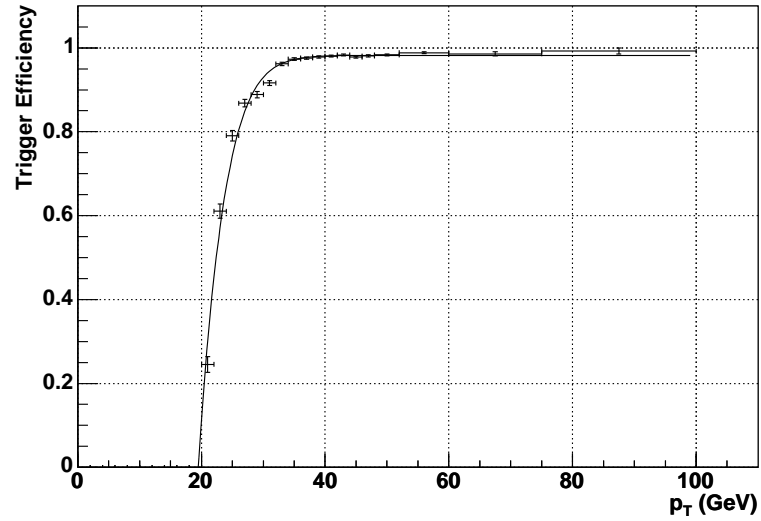


Figure 8: Overall trigger efficiency vs electron  $p_T$  for the  $Z$  inclusive sample. The line represents a fit to the data points.

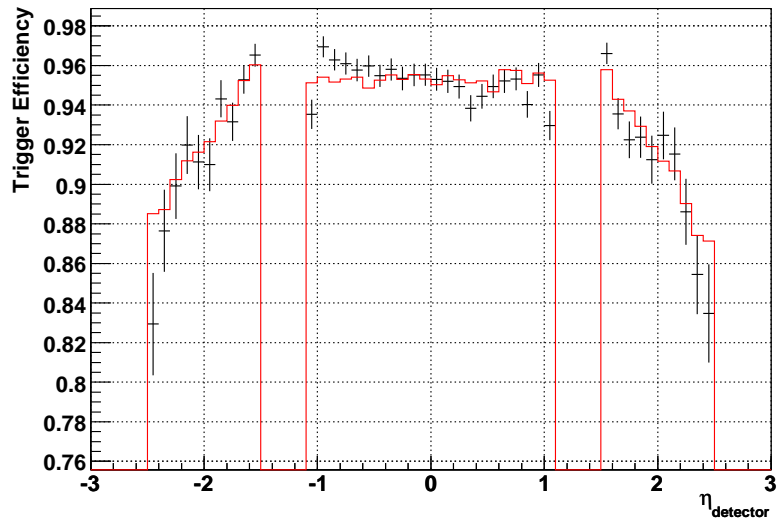


Figure 9: Overall measured trigger efficiency vs electron  $\eta_{\text{detector}}$  for the  $Z$  inclusive sample. The points correspond to the measured trigger efficiency in data averaged over  $p_T$ . The solid line corresponds to the trigger efficiency based on the parameterized efficiency curves.

## 4.2 Electron Reconstruction and Identification Scale Factors

Electromagnetic reconstruction and identification (recoID) efficiencies were determined for various jet multiplicities in data and MC. The efficiencies were measured using the electrons from  $Z$  boson decays in data and MC. Figures 10 through 14 show electron comparison distributions for data and MC PYTHIA  $Z \rightarrow e\bar{e} + X$  after the selection of a  $Z$  boson. The plots show that PYTHIA reasonably models the  $Z$  inclusive data sample.

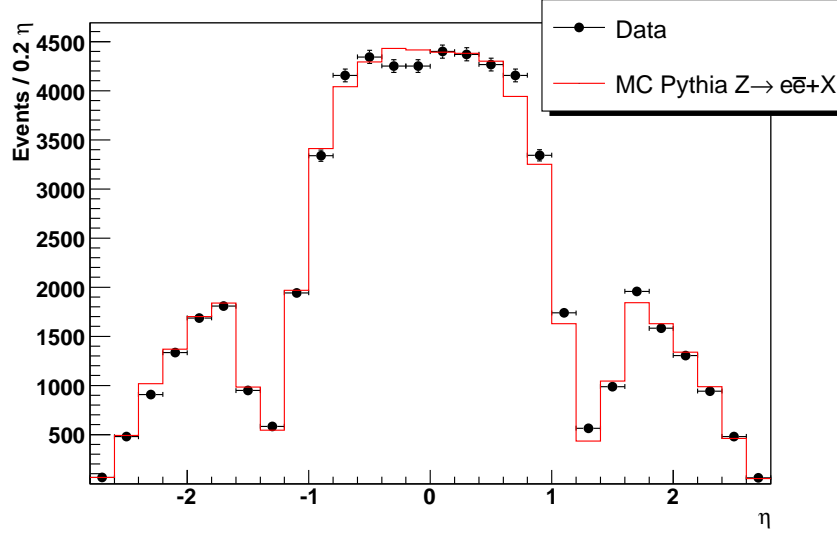


Figure 10: Electron  $\eta$  distribution for the  $Z$  inclusive sample after the diem invariant mass cut of  $75 \text{ GeV} < M_{ee} < 105 \text{ GeV}$ . The data points are background subtracted using the sidebands of the  $Z$  invariant mass distribution. PYTHIA is then normalized to the number of events in data.

In the central region of the calorimeter  $|\eta_{detector}| < 1.1$ , the efficiencies are studied versus the  $p_T$  and the modulus of  $\phi + 2\pi$  of  $2\pi/32$  of the probe track. There are 32 trigger towers around the circumference of the calorimeter ( $2\pi$ ). The width of each trigger tower is  $2\pi/32$  or 0.196 which is rounded to 0.2. There are cracks in  $\phi$  around each trigger tower in the central calorimeter and therefore each trigger tower edge has a large decrease in efficiency. The remainder, calculated from the modulus function (fmod), will range from 0 to 0.2, so that all 32 trigger towers can be overlaid into one trigger tower histogram. In the forward regions of the calorimeter  $1.5 < |\eta_{detector}| < 2.5$ , the efficiencies are determined versus the  $p_T$  and  $\eta_{detector}$  of the probe track. The EM1TRK data sample and PYTHIA  $Z \rightarrow e\bar{e} + X$  sample were used to compare efficiencies and to generate the scale factor. The efficiencies were calculated using a tag and probe method. The tag electron must satisfy the following conditions:

- $p_T > 20 \text{ GeV}$ ;
- EM Fraction  $> 0.95$ ;
- Isolation  $< 0.10$ ;
- $\chi^2 \text{ H-Matrix}(7) < 9$  if  $|\eta_{detector}| < 1.1$ ;

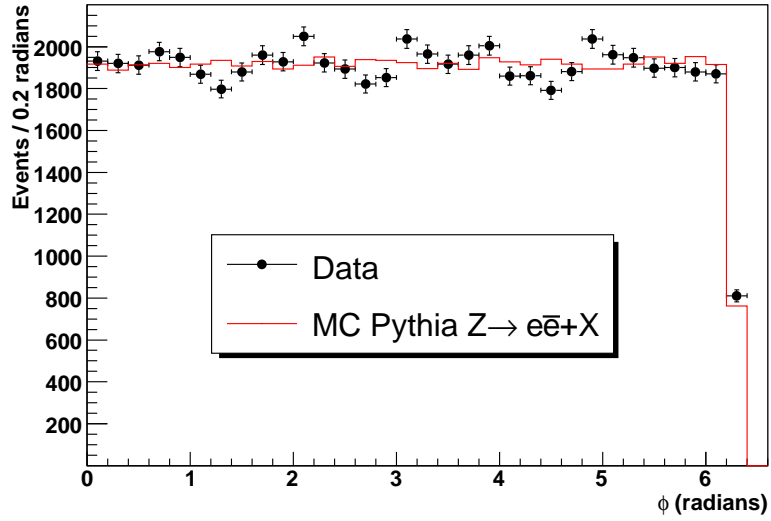


Figure 11: Electron  $\phi$  distribution for the  $Z$  inclusive sample after the diem invariant mass cut of  $75 \text{ GeV} < M_{ee} < 105 \text{ GeV}$ . The data points are background subtracted using the sidebands of the  $Z$  invariant mass distribution. PYTHIA is then normalized to the number of events in data.

- $\chi^2$  H-Matrix(7)  $< 17$  if  $1.5 < |\eta_{detector}| < 2.5$ ;
- passes the trigger (data only) with  $\Delta R < 0.4$  of L1, L2, and L3 trigger objects;
- spatial track match with  $\Delta R < 0.14$ ;
- track isolation ( $\Sigma p_T$  of tracks within  $\Delta R < 0.3$ )  $< 0.25$  probe track  $p_T$ .

The track requirements are:

- stereo track;
- $20 < p_T < 160 \text{ GeV}$ ;
- $\chi^2$  probability for the best track  $< 8.0$ ;
- distance of closest approach between the track and beam position in the  $R - \phi$  plane  $< 0.3 \text{ cm}$ ;
- distance of closest approach between the track and beam position along the  $Z$  axis  $< 4.0 \text{ cm}$ ;
- track isolation ( $\Sigma p_T$  of tracks with  $\Delta R < 0.3$ )  $< 0.25$  probe track  $p_T$ .

The matched electrons requirements are:

- ID = 10 or  $\pm 11$ ;
- EM Fraction  $> 0.9$ ;

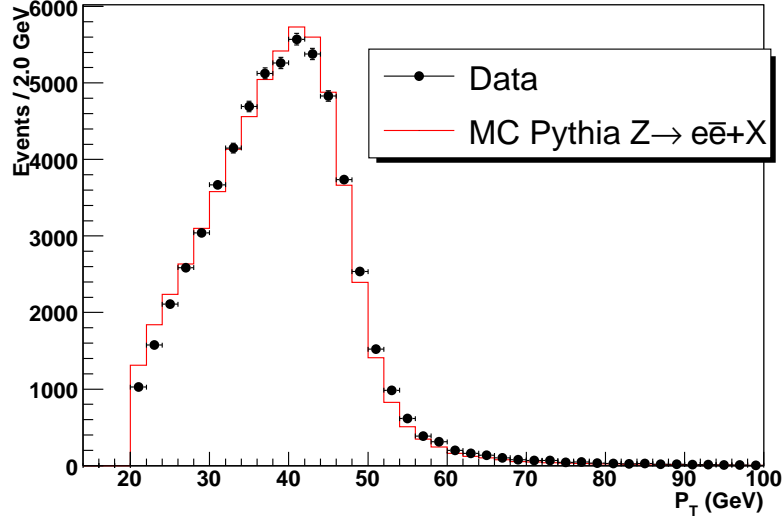


Figure 12: Electron  $p_T$  distribution in events for the  $Z$  inclusive sample after the diem invariant mass cut of  $75 \text{ GeV} < M_{ee} < 105 \text{ GeV}$ . The data points are background subtracted using the sidebands of the  $Z$  invariant mass distribution. PYTHIA is then normalized to the number of events in data.

- Isolation  $< 0.15$ ;
- $\chi^2$  of H-Matrix(7)  $< 12$  if  $|\eta_{detector}| < 1.1$ ;
- $\chi^2$  of H-Matrix(7)  $< 20$  if  $1.5 < |\eta_{detector}| < 2.5$ ;
- with  $\Delta R < 0.14$  of the probe track.

The probe is a track which has to fulfill the track requirements and have the opposite sign of the tag track. The tag electron and the probe track have to be within the invariant mass window  $80 \text{ GeV} < M_{tag_{electron}probe_{track}} < 100 \text{ GeV}$ . Figures 15 and 16 show the invariant mass distribution of the tag electron and probe track before and after finding a reconstructed electron which passed all the ID cuts, respectively. The sidebands of the invariant mass peak (starting 10 GeV away from the mass window) were used to estimate the background contribution to the average efficiency. The efficiencies were calculated using an inclusive jet multiplicity sample to improve statistics. The efficiencies versus inclusive jet multiplicity were measured, Table 6 and Figure 35.

Figures 17 through 20 show the efficiencies in 1D plots measured in data and MC.

sample	$\geq 0$ jets	$\geq 1$ jet	$\geq 2$ jets
data	$88.9 \pm 0.2$	$88.1 \pm 0.7$	$90.5 \pm 1.8$
Monte Carlo	$92.71 \pm 0.06$	$91.9 \pm 0.2$	$91.7 \pm 0.6$

Table 6: Electron reconstruction-identification efficiencies vs jet multiplicity for data and MC. Background has been removed by using the sidebands of the invariant mass peak.



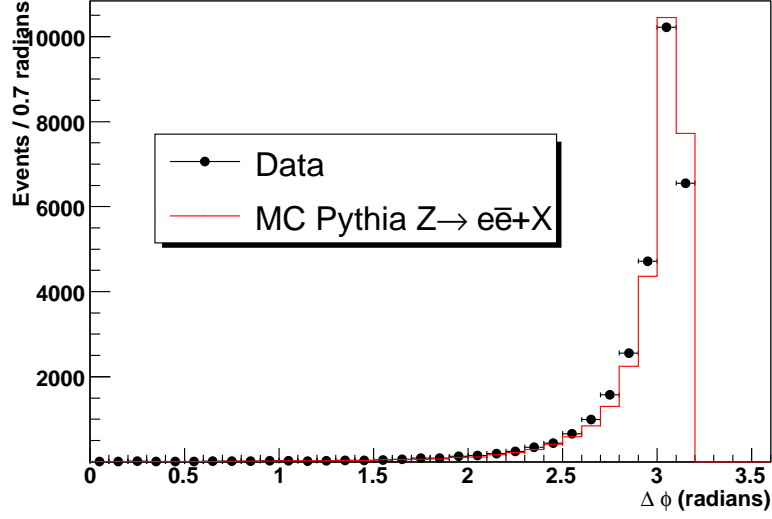


Figure 13: Electron  $\Delta\phi$  distribution in events for the  $Z$  inclusive sample after the diem invariant mass cut of  $75 \text{ GeV} < M_{ee} < 105 \text{ GeV}$ . The data points are background subtracted using the sidebands of the  $Z$  invariant mass distribution. PYTHIA is then normalized to the number of events in data.

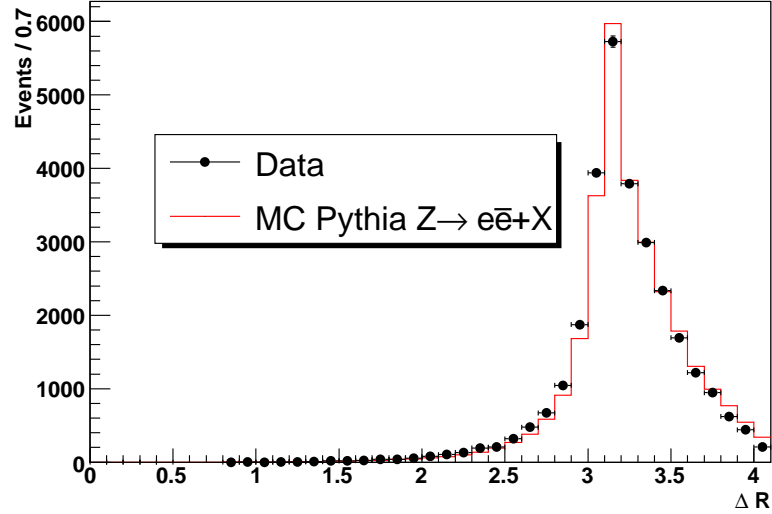


Figure 14: Electron  $\Delta R$  distribution in events for the  $Z$  inclusive sample after the diem invariant mass cut of  $75 \text{ GeV} < M_{ee} < 105 \text{ GeV}$ . The data points are background subtracted using the sidebands of the  $Z$  invariant mass distribution. PYTHIA is then normalized to the number of events in data.

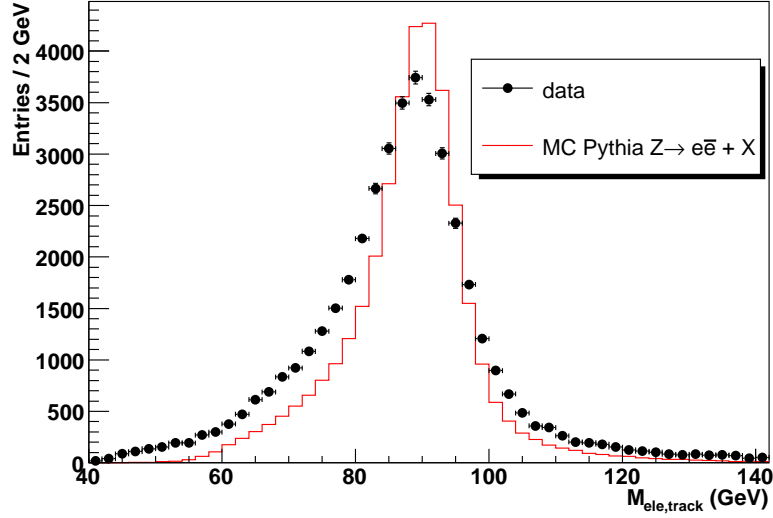


Figure 15: The invariant mass distribution for events for the  $Z$  inclusive sample for electron reco\*id efficiency using the tag electron and probe track. PYTHIA is normalized to have the same number of events in the window of  $75 \text{ GeV} < M_{ee} < 105 \text{ GeV}$  as data.

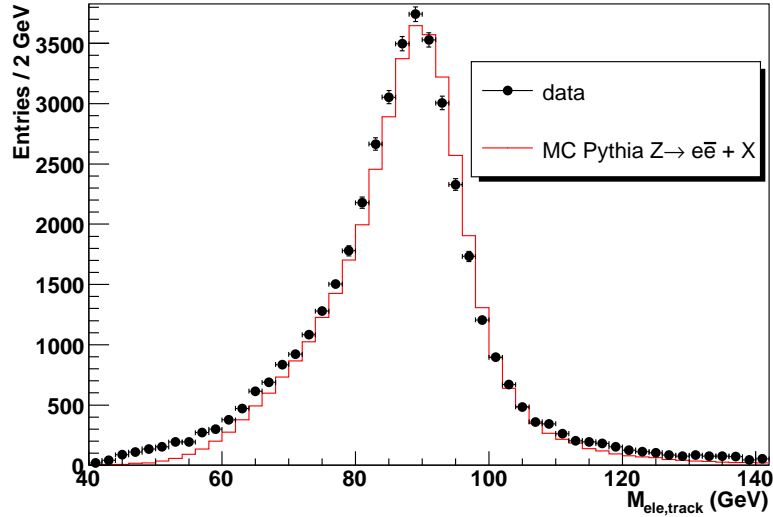


Figure 16: The invariant mass distribution for events for the  $Z$  inclusive sample for electron reco\*id efficiency using tag electron and probe track. The probe track in the MC is smeared to have the same resolution as the probe tracks in data. PYTHIA is normalized to have the same number of events in the window of  $75 \text{ GeV} < M_{ee} < 105 \text{ GeV}$  as data.

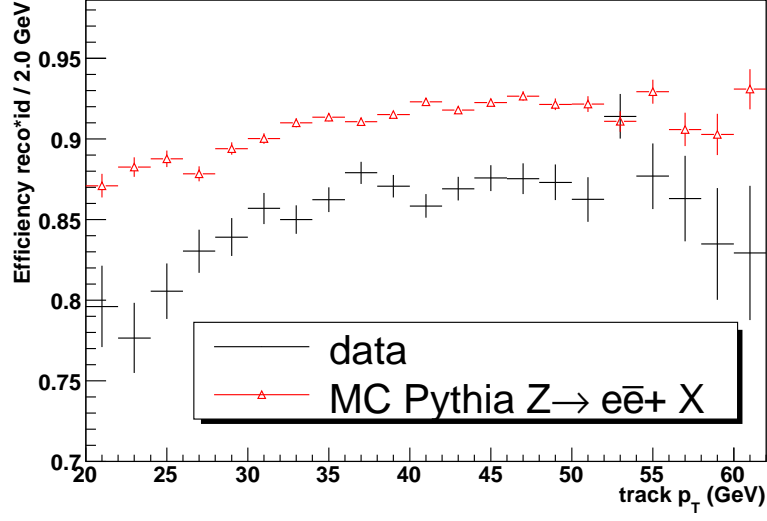


Figure 17: Electron reconstruction-identification efficiencies in data and MC for events for the  $Z$  inclusive sample vs probe track  $p_T$  without background subtraction. The MC sample is PYTHIA generated  $Z \rightarrow e\bar{e} + X$ . The probe track is in the central region  $|\eta_{detector}| < 1.1$  of the calorimeter.

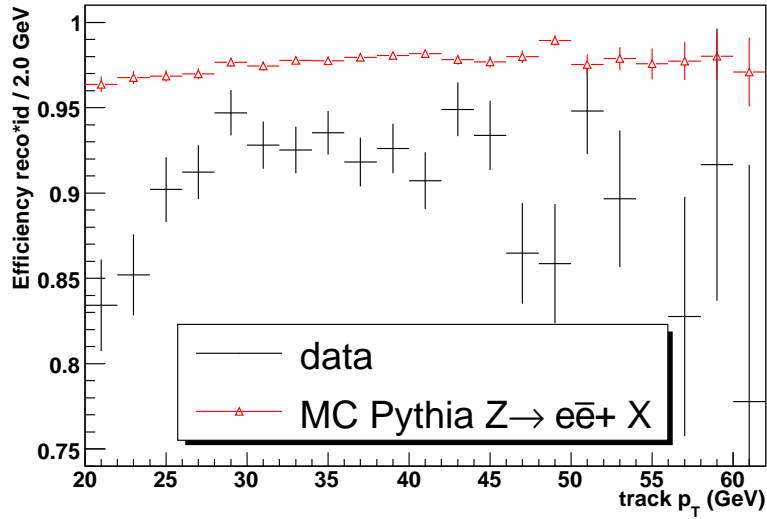


Figure 18: Electron reconstruction-identification efficiencies in data and MC for events for the  $Z$  inclusive sample vs probe track  $p_T$  without background subtraction. The MC sample is PYTHIA generated  $Z \rightarrow e\bar{e} + X$ . The probe track is in the forward region  $1.5 < |\eta_{detector}| < 2.5$  of the calorimeter.

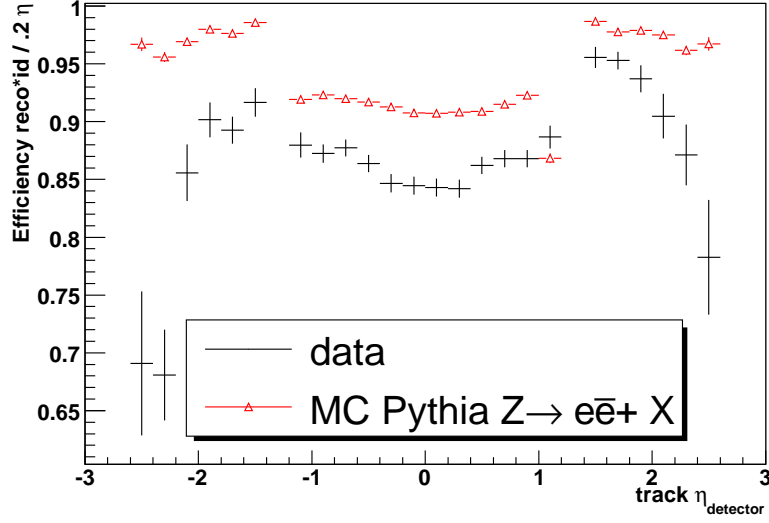


Figure 19: Electron reconstruction-identification efficiencies in data and MC for events for the  $Z$  inclusive sample vs probe track  $\eta_{\text{detector}}$  without background subtraction. The MC sample is PYTHIA generated  $Z \rightarrow e\bar{e} + X$ .

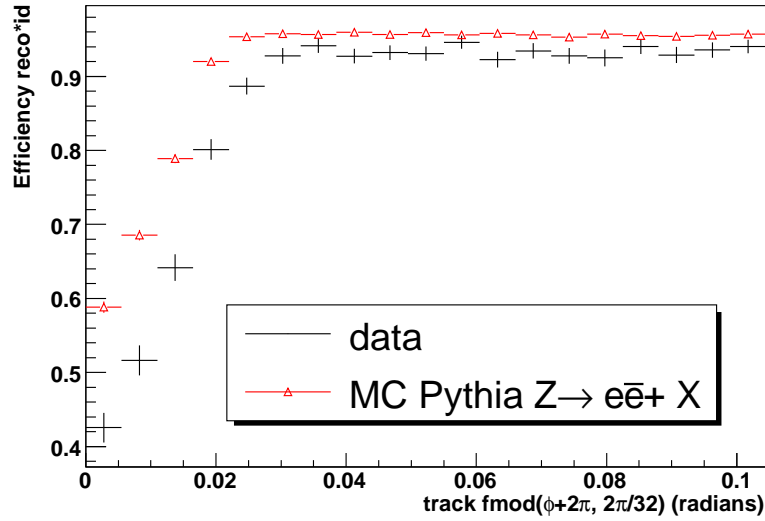


Figure 20: Electron reconstruction-identification efficiencies in data and MC for events for the  $Z$  inclusive sample vs probe track  $fmod(\phi + 2\pi, 2\pi/32)$  without background subtraction. The MC sample is PYTHIA generated  $Z \rightarrow e\bar{e} + X$ .

The probe track scans for a reconstructed electron, within  $\Delta R < 0.14$ , which passes the cuts of EM fraction, isolation, and  $\chi^2$  of H-matrix 7 cuts. A 2D ( $p_T$ , modulus ( $\phi+2\pi, 2\pi/32$ )) fit is made for tracks with  $|\eta_{detector}| < 1.1$  and another 2D ( $p_T, \eta_{detector}$ ) fit is made for the forward tracks. The 2D parameterizations are then tested on the probe tracks and overlaid with the calculated efficiencies, shown in 1D plots, in Figures 21 through 32. The scale factors applied to the Monte Carlo are 2D ratios of the 2D fits for data and MC. The scale factors are applied to the MC using electron  $p_T$ ,  $\eta$ , and the modulus of  $\phi$ . The scale factors are functions of track  $p_T$  not electron  $p_T$ . Figures 33 and 34 show the track  $p_T$  to be slightly lower than the electron  $p_T$  in both data and MC, therefore, a correction factor is made to the electron  $p_T$  before retrieving the scale factor value.

The uncertainty for the electron reconstruction \* identification scale factor was estimated from four sources. The first source is the difference between the  $Z+ \geq 0j$  average efficiency value and the  $Z+ \geq 2j$  average efficiency value in data, 1.8%. The second source is the statistical uncertainty of the average efficiency value for  $Z+ \geq 0j$ , 0.2%. The third source, 0.8%, is the difference between the the average efficiency value (after background subtraction) in data using a 20 GeV search window versus the average difference in the average efficiency value found by varying the Z boson search window in  $\pm 5$  GeV increments around the original search window. The forth source is the difference between the  $Z+ \geq 0$  average efficiency value in MC and the the  $Z+ \geq 2$  average efficiency value in MC. The drop in the average MC efficiency will bring data and MC into better agreement, therefore it is only added in as a plus contribution to the uncertainty, 1.1%. The first three sources of uncertainty are added in quadrature with the forth source added in linearly. The scale factor is modified by  $\pm 2.0^{+1.1}_0\%$  and ran through the analysis code. The overall uncertainty due to the electron recoID scale factor is 6%.

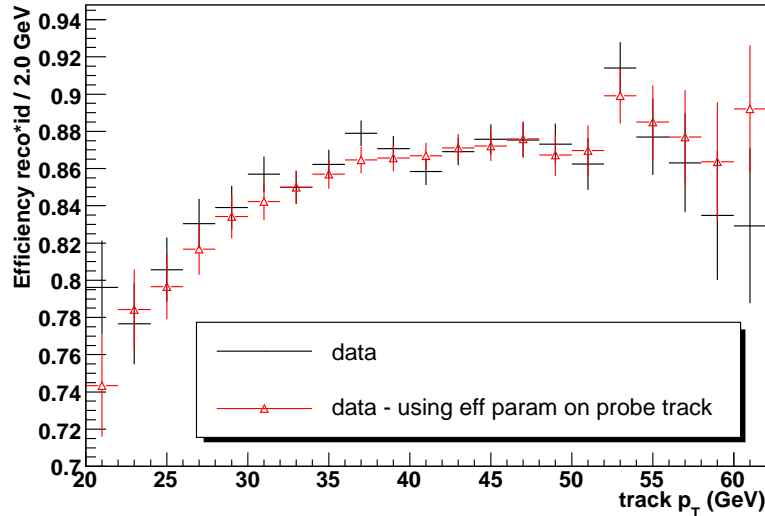


Figure 21: Electron reconstruction-identification efficiencies in data for events for the  $Z$  inclusive sample vs probe track  $p_T$  in the CC without background subtraction. The measured efficiency (data) is matched against the 2D fit ( $p_T, \phi$ ) of the probe track averaged over  $\phi$  and  $\eta$ .

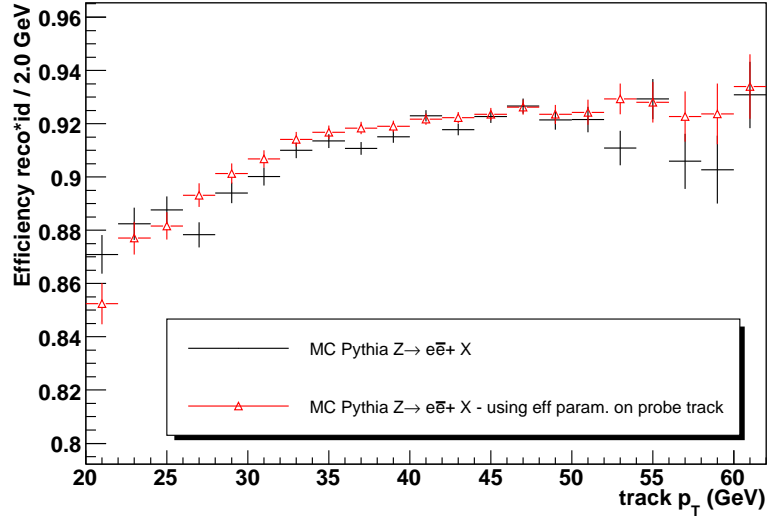


Figure 22: Electron reconstruction-identification efficiencies in MC for events for the  $Z$  inclusive sample vs probe track  $p_T$  in the CC. The measured efficiency (MC PYTHIA  $Z \rightarrow e\bar{e} + X$ ) is matched against the 2D fit  $(p_T, \phi)$  of the probe track averaged over  $\phi$  and  $\eta$ .

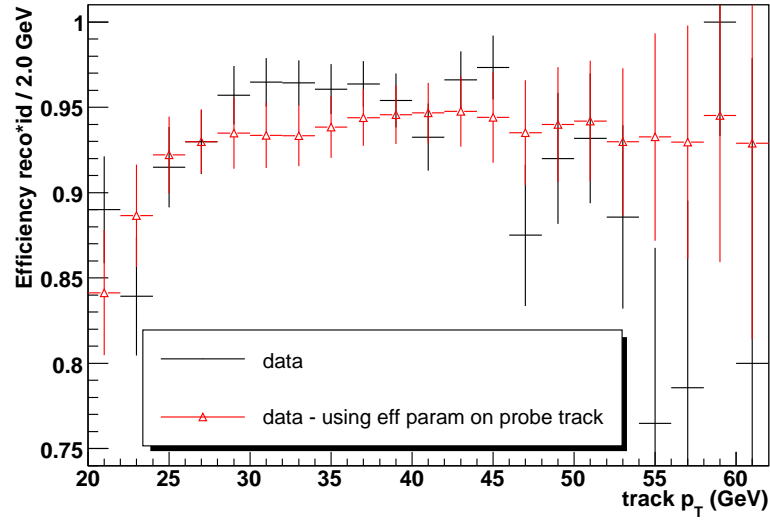


Figure 23: Electron reconstruction-identification efficiencies in data for events for the  $Z$  inclusive sample vs probe track  $p_T$  in the ECN without background subtraction. The measured efficiency (data) is matched against the 2D fit ( $p_T, \eta$ ) of the probe track averaged over  $\phi$  and  $\eta$ .

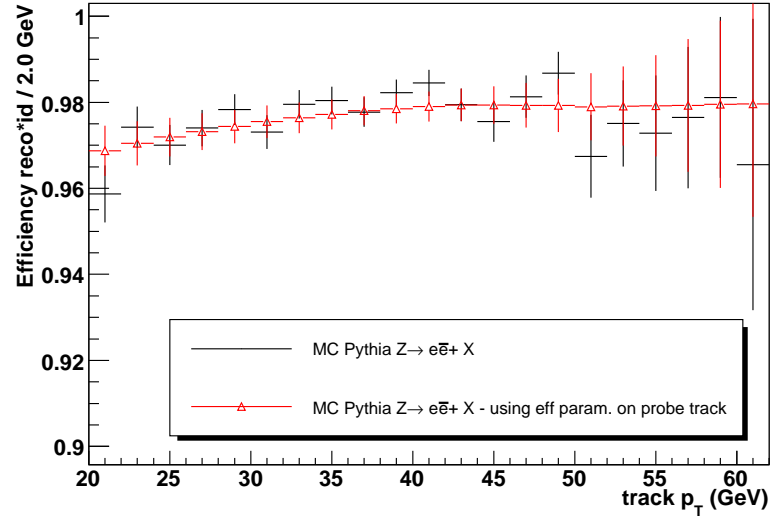


Figure 24: Electron reconstruction-identification efficiencies in MC for events for the  $Z$  inclusive sample vs probe track  $p_T$  in the ECN. The measured efficiency (MC PYTHIA  $Z \rightarrow e\bar{e} + X$ ) is matched against the 2D fit ( $p_T, \eta$ ) of the probe track averaged over  $\phi$  and  $\eta$ .

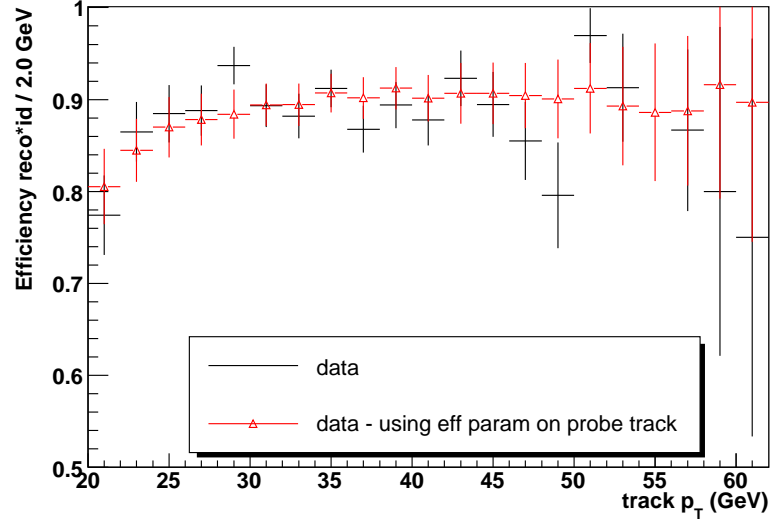


Figure 25: Electron reconstruction-identification efficiencies in data for events for the  $Z$  inclusive sample vs probe track  $p_T$  in the ECS without background subtraction. The measured efficiency (data) is matched against applying the 2D fit  $(p_T, \eta)$  of the probe track averaged over  $\phi$  and  $\eta$ .

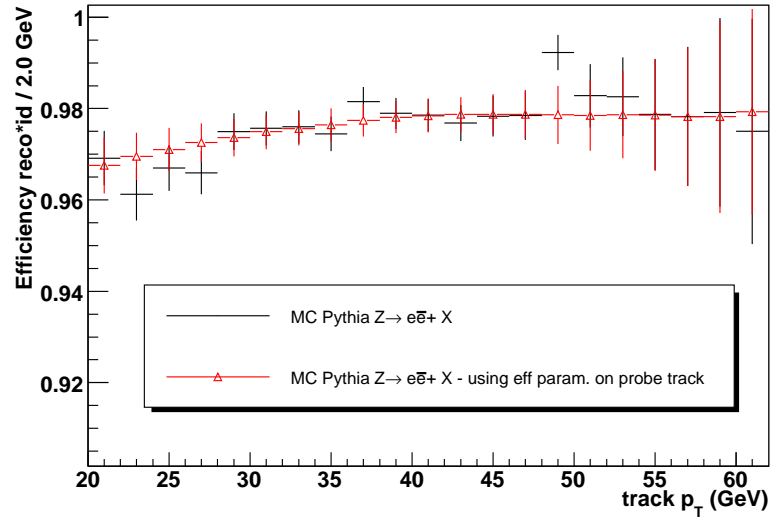


Figure 26: Electron reconstruction-identification efficiencies in MC for events for the  $Z$  inclusive sample vs probe track  $p_T$  in the ECS. The measured efficiency (MC PYTHIA  $Z \rightarrow e\bar{e} + X$ ) is matched against the 2D fit  $(p_T, \eta)$  of the probe track while averaged over  $\phi$  and  $\eta$ .



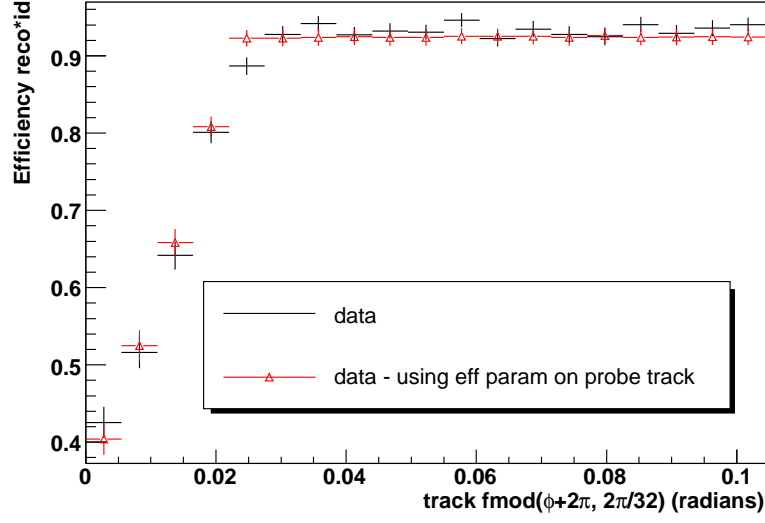


Figure 27: Electron reconstruction-identification efficiencies in data for events for the  $Z$  inclusive sample vs probe track  $fmod(\phi + 2\pi, 2\pi/32)$  in the CC without background subtraction. The measured efficiency (data) is matched against the 2D fit  $(p_T, \phi)$  to the probe track while averaged over  $p_T$  and  $\eta$ .

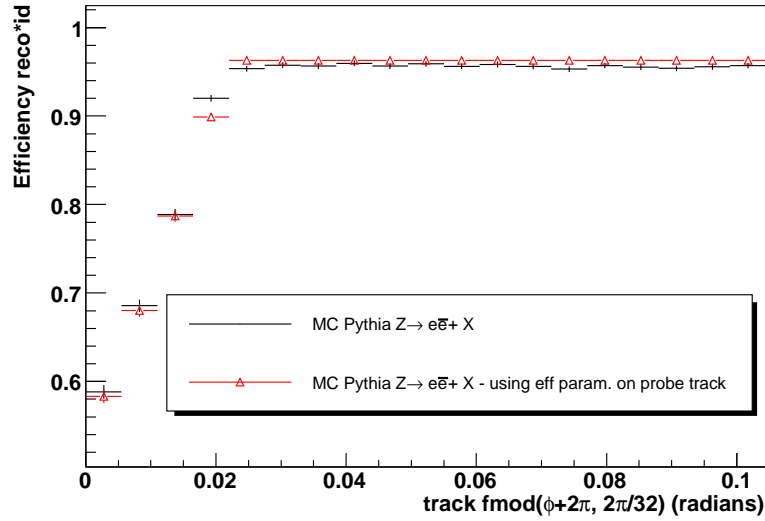


Figure 28: Electron reconstruction-identification efficiencies in MC for events for the  $Z$  inclusive sample vs probe track  $fmod(\phi + 2\pi, 2\pi/32)$  in the CC. The measured efficiency (MC PYTHIA  $Z \rightarrow e\bar{e} + X$ ) is matched against the 2D fit  $(p_T, \phi)$  of the probe track while averaged over  $p_T$  and  $\eta$ .

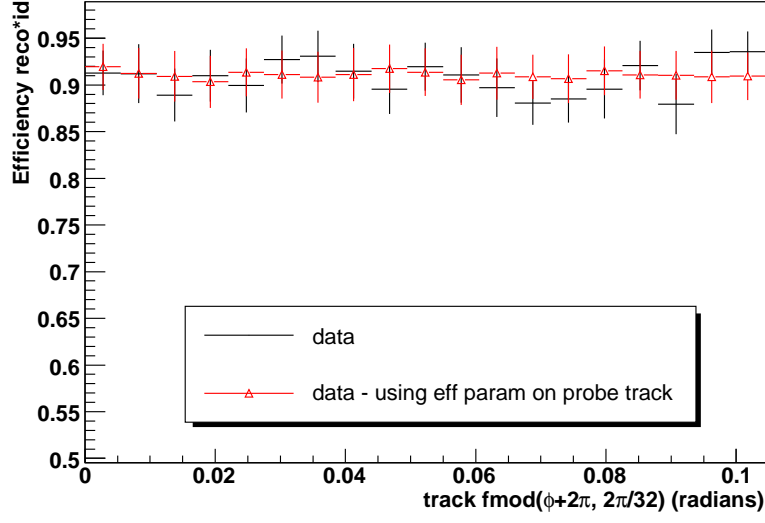


Figure 29: Electron reconstruction-identification efficiencies in data for events for the  $Z$  inclusive sample vs probe track  $fmod(\phi + 2\pi, 2\pi/32)$  in the EC without background subtraction. The measured efficiency (data) is matched against the 2D fit  $(p_T, \eta)$  of the probe track while averaged over  $p_T$  and  $\eta$ .

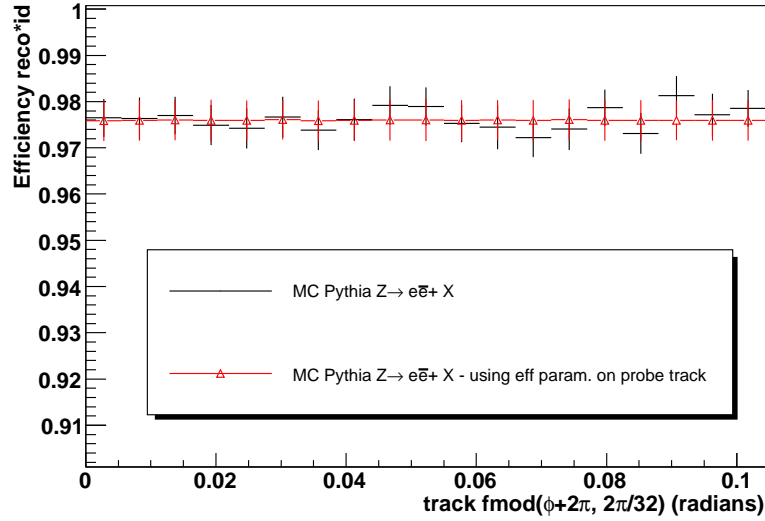


Figure 30: Electron reconstruction-identification efficiencies in MC for events for the  $Z$  inclusive sample vs probe track  $fmod(\phi + 2\pi, 2\pi/32)$  in the EC. The measured efficiency (MC PYTHIA  $Z \rightarrow e\bar{e} + X$ ) is matched against applying the 2D fit  $(p_T, \eta)$  of the probe track while averaged over  $p_T$  and  $\eta$ .

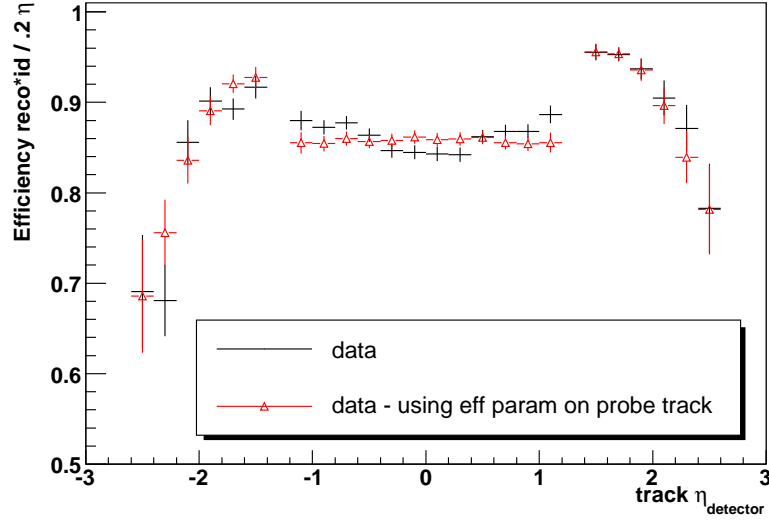


Figure 31: Electron reconstruction-identification efficiencies in data for events for the  $Z$  inclusive sample vs probe track  $\eta_{detector}$  without background subtraction. The measured efficiency (data) is matched against the 2D fits of the probe track while averaged over  $p_T$  and  $\phi$ .

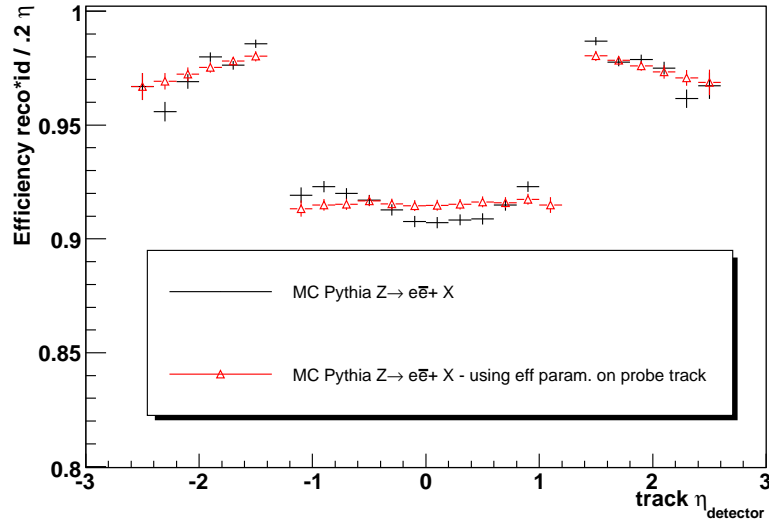


Figure 32: Electron reconstruction-identification efficiencies in MC for events for the  $Z$  inclusive sample vs probe track  $\eta_{detector}$ . The measured efficiency (MC PYTHIA  $Z \rightarrow e\bar{e} + X$ ) is matched against applying the 2D fits of the probe track while averaged over  $p_T$  and  $\phi$ .

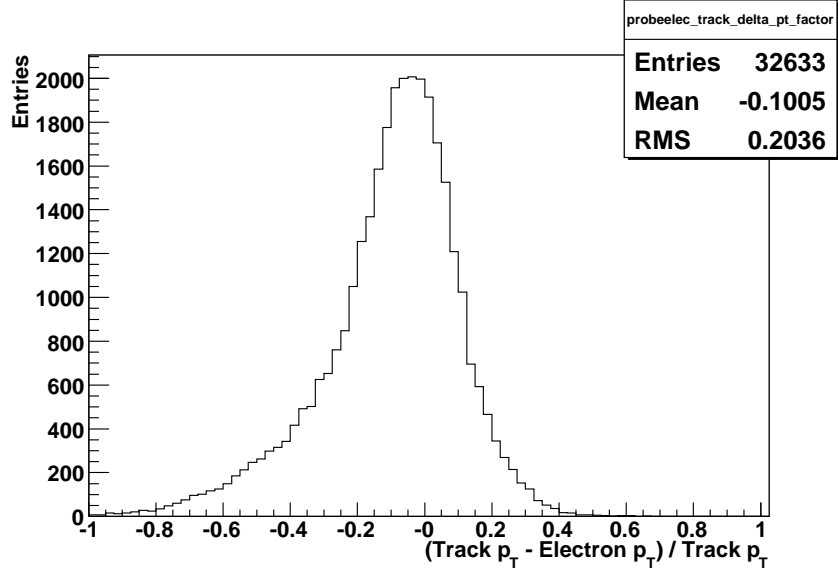


Figure 33: Probe track  $p_T$  minus matched electron  $p_T$  divided by the probe track  $p_T$  in data. The  $p_T$  of the probe track is approximately 5% lower than the  $p_T$  of the calorimeter reconstructed electron, due to resolution differences in the two separate detector systems. As the  $p_T$  of an electron increases, the resolution in the tracking detectors becomes worse and the resolution in the calorimeter detector becomes better. The EM efficiencies are calculated using the probe track  $p_T$ , but the scale factor applied in the MC uses the  $p_T$  of the reconstructed electron.

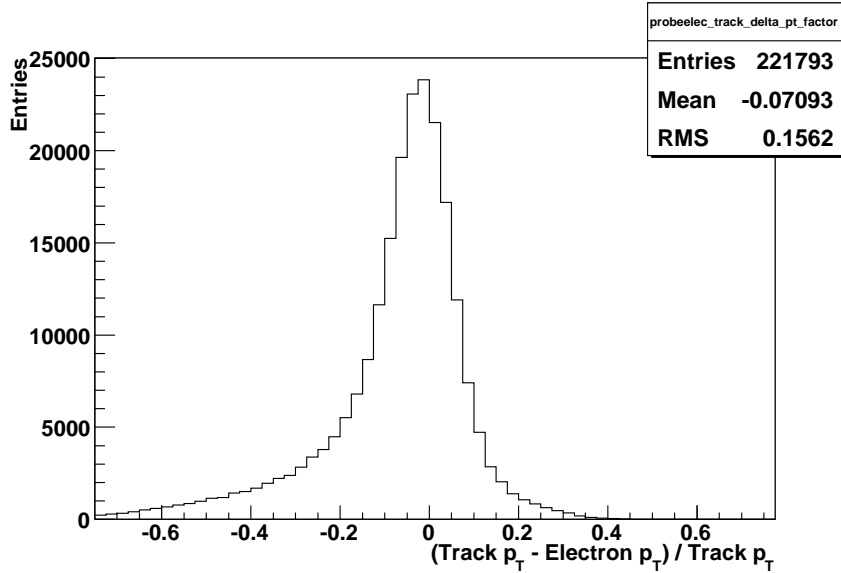


Figure 34: Probe track  $p_T$  minus matched electron  $p_T$  divided by probe track  $p_T$  in MC. The  $p_T$  of the probe track is approximately 2% lower than the  $p_T$  of the calorimeter reconstructed electron. This difference is due to resolution differences in the two separate detector systems. As the  $p_T$  of an electron increases, the resolution in the tracking detectors becomes worse, and the resolution in the calorimeter detector becomes better. The EM efficiencies are calculated using the probe track  $p_T$ , but the scale factor applied in the MC uses the  $p_T$  of the reconstructed electron. An additional study was performed by oversmearing the MC probe track  $p_T$  to the resolution of data [25]. The additional smearing did not effect the MC recoID efficiencies.

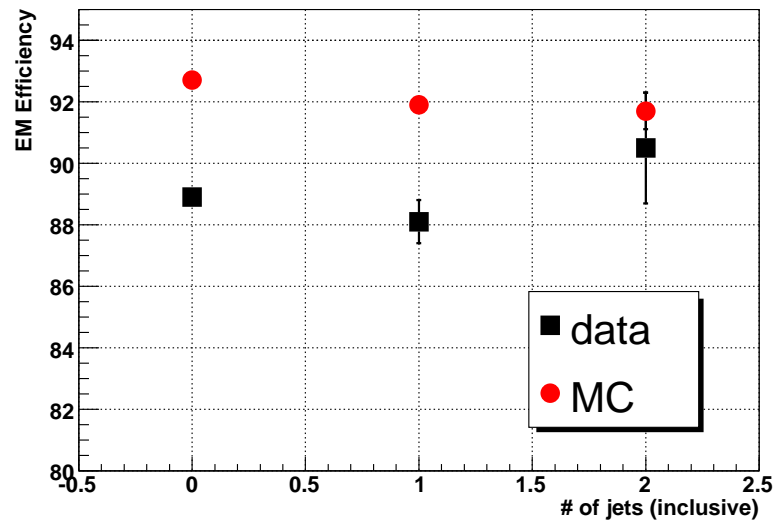


Figure 35: Electron reconstruction-identification efficiency vs jet multiplicity for data and MC after background subtraction. The sidebands of the invariant mass peak were used for the background estimation.

### 4.3 Electron Track Match Scale Factor

The efficiencies for an electron to have a track match have been measured in data and MC. The efficiencies were measured using  $Z$  bosons in data and MC. In the central region of the calorimeter  $|\eta_{detector}| < 1.1$ , the efficiencies are found to be dependent on  $p_T$ . In the forward region of the calorimeter  $1.5 < |\eta_{detector}| < 2.5$ , the efficiencies are found to be dependent on  $p_T$  and  $\eta_{detector}$ . The EM1TRK data sample and PYTHIA  $Z \rightarrow e\bar{e} + X$  sample were used to compare efficiencies and to generate a scale factor. The efficiencies were calculated using a tag and probe method.

The tag electron must satisfy the following conditions:

- $p_T > 20$  GeV;
- EM Fraction  $> 0.9$ ;
- Isolation  $< 0.15$ ;
- $\chi^2$  H-Matrix(7)  $< 12$  if  $|\eta_{detector}| < 12$ ;
- $\chi^2$  H-Matrix(7)  $< 20$  if  $1.5 < |\eta_{detector}| < 2.5$ ;
- passes the trigger (data only) with  $\Delta R < 0.4$  of L1, L2, and L3 trigger objects;
- Spatial track match with  $\Delta R < 0.14$ .

The probe electron must satisfy the following conditions:

- $p_T > 20$  GeV;
- EM Fraction  $> 0.9$ ;
- Isolation  $< 0.15$ ;
- $\chi^2$  H-Matrix(7)  $< 12$  if  $|\eta_{detector}| < 12$ ;
- $\chi^2$  H-Matrix(7)  $< 20$  if  $1.5 < |\eta_{detector}| < 2.5$ .

The tag and probe electrons have to be within the invariant mass window  $75 \text{ GeV} < M_{ee} < 105 \text{ GeV}$ . Figures 50 through 52 show the invariant mass histograms of the tag and probe electrons before requiring a track match for different jet multiplicities. The sidebands to the invariant mass peak were used in the background subtraction to derive the average efficiency and to properly normalize the scale factor. The invariant mass distributions were also fitted with a convoluted Breit-Wigner and Gaussian shape for the  $Z$  boson with an exponential shape for the background and the agreement between the two background subtracting techniques was found to be acceptable (within 1%). A probe electron has a track match if the track matching probability,  $P(\chi^2)$ , is greater than 0.01. Figures 36 through 38 show data and MC comparisons of the tracks which are matched to an electron. These track distributions are made after a  $75 < M_{ee} < 105 \text{ GeV}$  cut on the electrons for events with 0 or more jets. Figure 39 shows the track  $p_T$  being slightly lower than the matched electron

$p_T$ . The resolution is also shown to be worse in data. Figures 40 through 42 show the track matching efficiency for data and MC. The data distributions are not background subtracted and are used to parameterize the efficiencies vs probe track  $p_T$ . Figures 43 through 48 show comparisons of the parameterized efficiencies in 1D plots calculated in data and MC using the 1D ( $p_T$ ) fit made for electrons with  $|\eta_{detector}| < 1.1$  and the 2D ( $p_T, \eta$ ) fit is made for the forward electrons. Table 7 and Figure 49 show the electron track match efficiency versus jet multiplicity using the sideband method for subtracting background in data.

The uncertainty for the track match scale factor was estimated from four sources. The first source is the difference between the  $Z+ \geq 0j$  average efficiency value and the  $Z+ \geq 2j$  average efficiency value in data, 0.9%. The second source is the statistical uncertainty of the average efficiency value for  $Z+ \geq 0j$ , 0.3%. The third source, 0.4%, is from the difference of the average efficiency when using the errors of the exponential fit for the background subtraction of the  $Z$  peak. The forth source is the difference between the MC  $Z+ \geq 0$  average efficiency value and the the  $Z+ \geq 2$  average efficiency value, +0.8%. The first three sources of uncertainty are added in quadrature with the forth source added in linearly. The scale factor is modified by  $\pm 1.0^{+0.8}_{-0}\%$  and ran through the analysis code. The overall uncertainty due to the track match scale factor is 1%.

sample	$\geq 0$ jets	$\geq 1$ jet	$\geq 2$ jets
data	$76.51 \pm 0.20$	$76.31 \pm 0.62$	$75.85 \pm 1.75$
Monte Carlo	$86.70 \pm 0.07$	$86.63 \pm 0.21$	$86.00 \pm 0.69$

Table 7: Track match efficiencies vs jet multiplicity for data and MC. The background has been removed by using the sidebands of the invariant mass distribution.

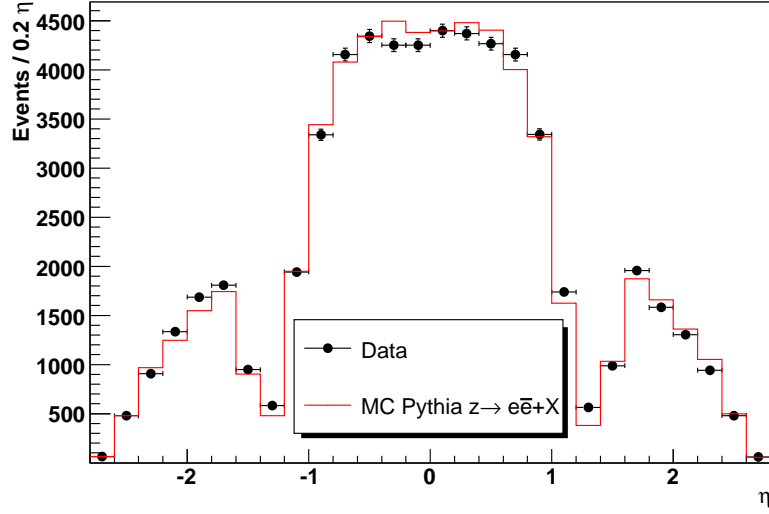


Figure 36: The  $\eta$  distribution of tracks which are matched to an electron in events for the  $Z$  inclusive sample in the events after the diem invariant mass cut of  $75 \text{ GeV} < M_{ee} < 105 \text{ GeV}$ . The data points are background subtracted using the sidebands of the invariant mass peak. PYTHIA is then normalized to the number of events in data.

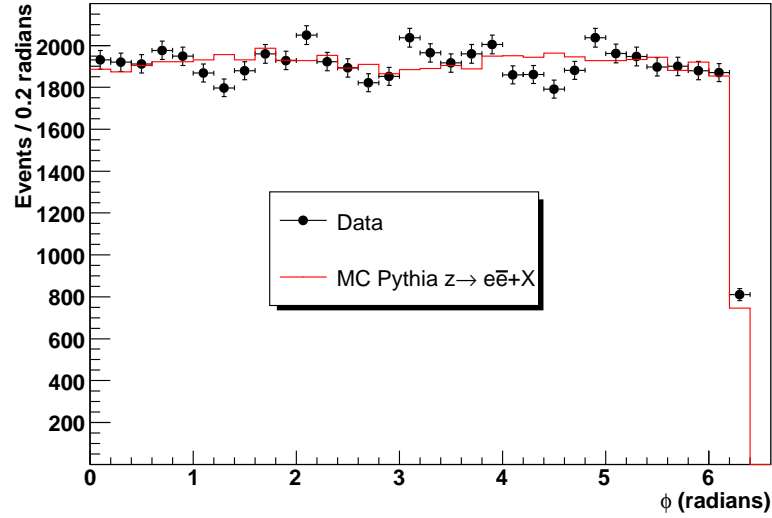


Figure 37: The  $\phi$  distribution of tracks which are matched to an electron in events for the  $Z$  inclusive sample after the diem invariant mass cut of  $75 \text{ GeV} < M_{ee} < 105 \text{ GeV}$ . The data points are background subtracted using the sidebands of the invariant mass peak. PYTHIA is then normalized to the number of events in data.



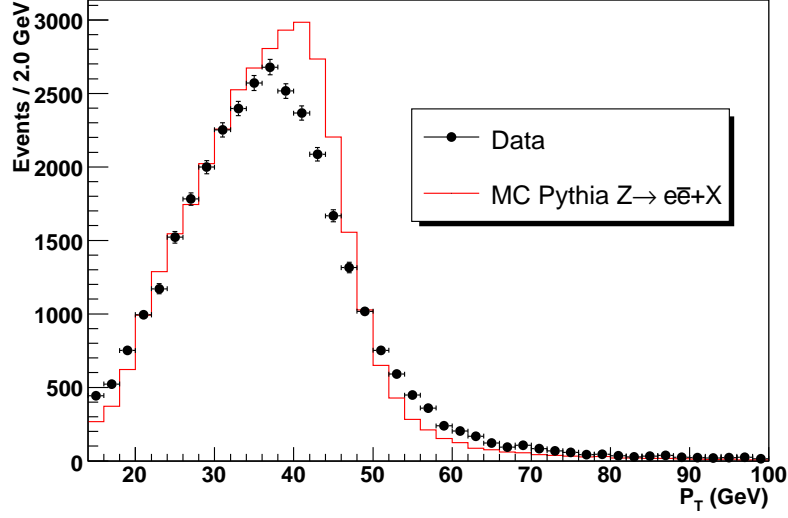


Figure 38:  $P_T$  distribution of tracks which are matched to an electron in events for the  $Z$  inclusive sample after the diem invariant mass cut of  $75 \text{ GeV} < M_{ee} < 105 \text{ GeV}$ . The data points are background subtracted using the sidebands of the invariant mass peak. PYTHIA is then normalized to the number of events in data.

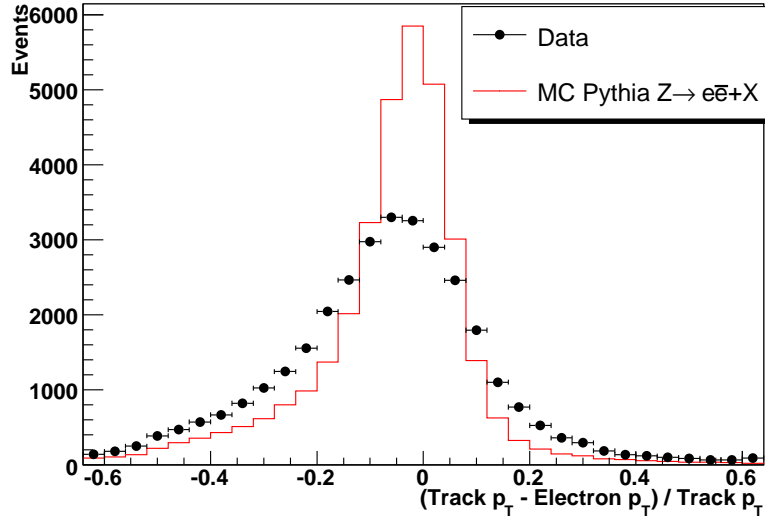


Figure 39: Track  $p_T$  - Electron  $p_T$  divided by Track  $p_T$  distribution in events for the  $Z$  inclusive sample after the diem invariant mass cut of  $75 \text{ GeV} < M_{ee} < 105 \text{ GeV}$ . PYTHIA is then normalized to the number of events in data. An additional study was performed by oversmearing the MC track  $p_T$  to the resolution of data [25]. The additional smearing did not effect the MC track match efficiencies.

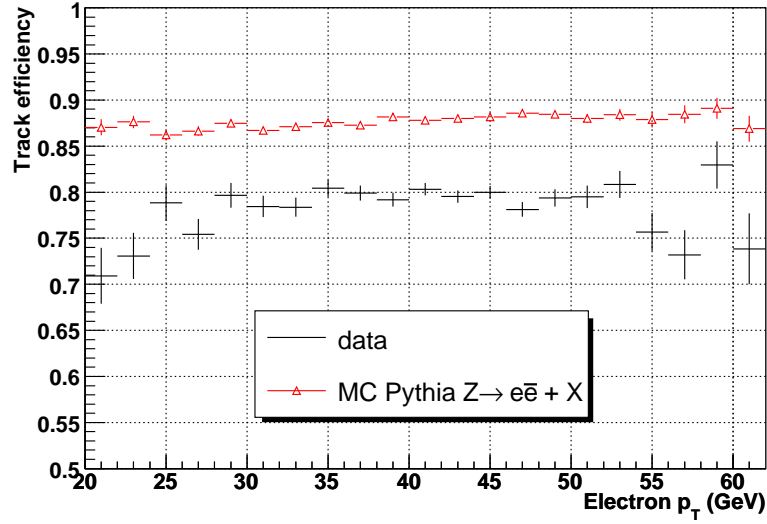


Figure 40: Track match efficiencies in data and MC for events for the  $Z$  inclusive sample vs probe electron  $p_T$  without background subtraction. The MC sample is PYTHIA generated  $Z \rightarrow e\bar{e} + X$ . The probe electron is in the central region  $|\eta_{detector}| < 1.1$  of the calorimeter.

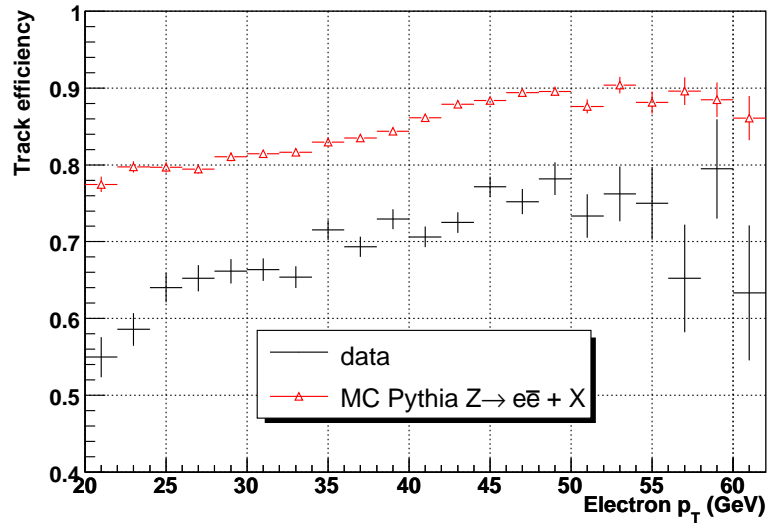


Figure 41: Track match efficiencies in data and MC for events for the  $Z$  inclusive sample vs probe electron  $p_T$  without background subtraction. The MC sample is PYTHIA generated  $Z \rightarrow e\bar{e} + X$ . The probe electron is in the forward region  $1.5 < |\eta_{detector}| < 2.5$  of the calorimeter.

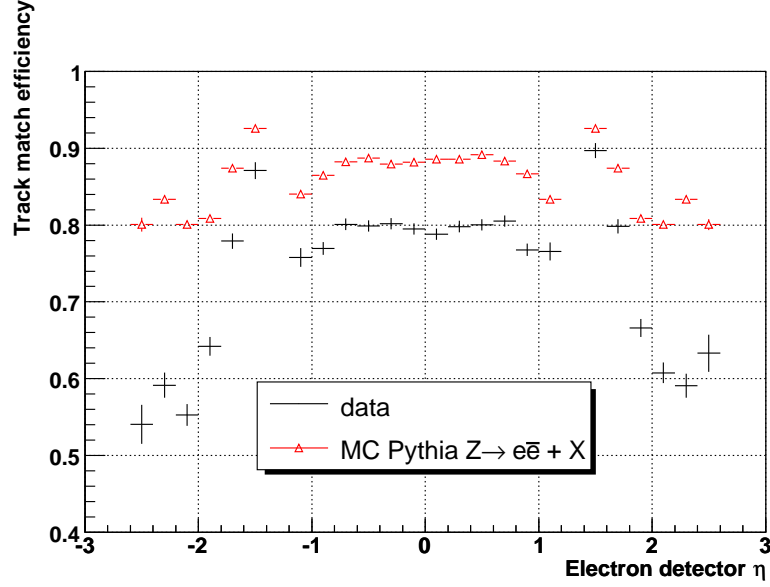


Figure 42: Track match efficiencies in data and MC for events for the  $Z$  inclusive sample vs probe electron  $\eta_{detector}$  without background subtraction. The MC sample is PYTHIA generated  $Z \rightarrow e\bar{e} + X$ .

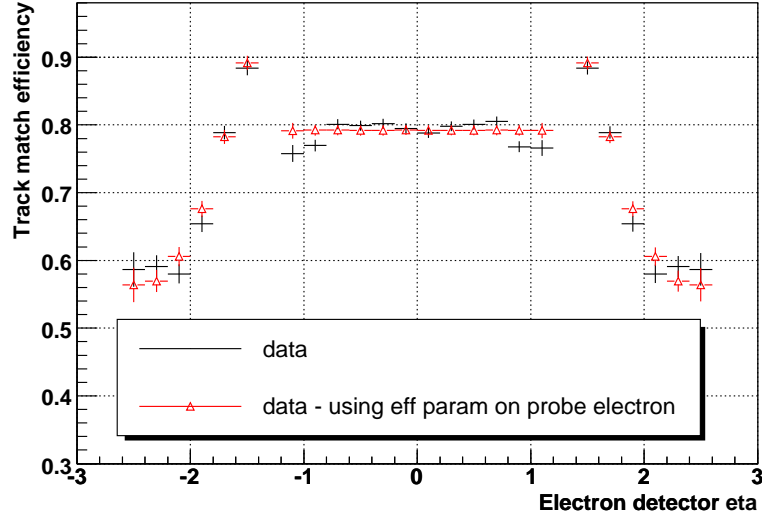


Figure 43: Track match efficiency in data for events for the  $Z$  inclusive sample vs probe electron  $\eta_{detector}$  without background subtraction. The measured efficiency (data) is matched against a 1D fit ( $p_T$ ) in the central region and a 2D fit ( $p_T, \eta_{detector}$ ) of the forward region to the probe electron. The efficiency is averaged over  $p_T$  and  $\phi$ .

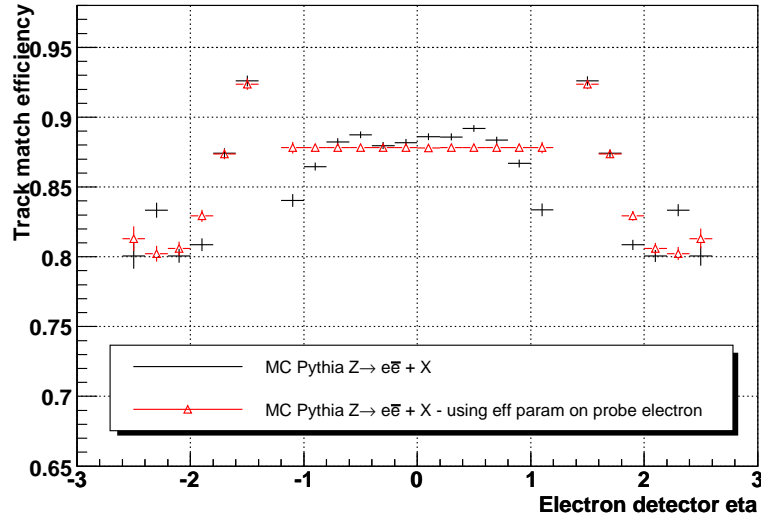


Figure 44: Track match efficiency in MC for events for the  $Z$  inclusive sample vs probe electron  $\eta_{detector}$ . The measured efficiency (MC) is matched against a 1D fit ( $p_T$ ) in the central region and a 2D fit ( $p_T, \eta_{detector}$ ) of the forward region to the probe electron. The efficiency is averaged over  $p_T$  and  $\phi$ .

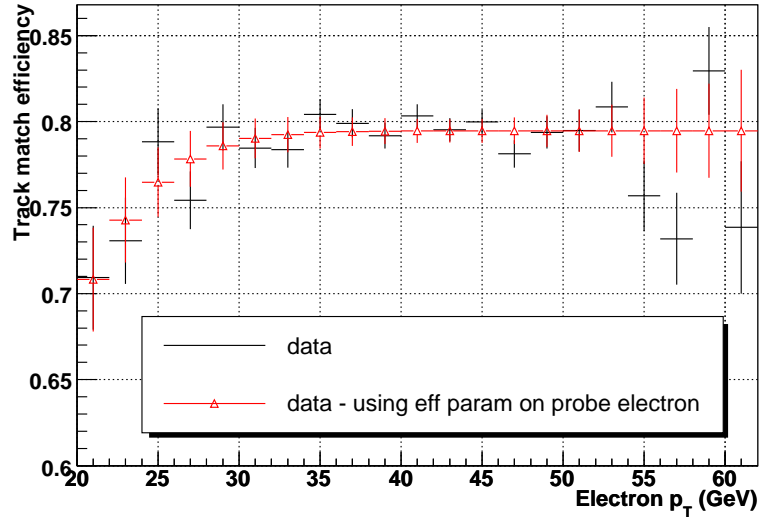


Figure 45: Track match efficiency in data for events for the  $Z$  inclusive sample vs probe electron  $p_T$  in the central region of the calorimeter without background subtraction. The measured efficiency (data) is matched against a 1D fit ( $p_T$ ) in the central region and a 2D fit ( $p_T, \eta_{detector}$ ) of the forward region to the probe electron. The efficiency is averaged over  $\eta$  and  $\phi$ .

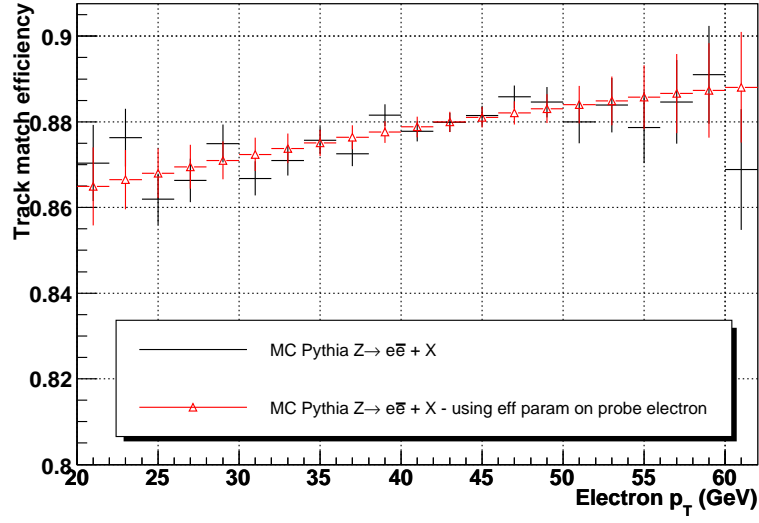


Figure 46: Track match efficiency in MC for events for the  $Z$  inclusive sample vs probe electron  $p_T$  in the central region of the calorimeter. The measured efficiency (MC) is matched against a 1D fit ( $p_T$ ) in the central region and a 2D fit ( $p_T, \eta_{detector}$ ) of the forward region to the probe electron. The efficiency is averaged over  $\eta$  and  $\phi$ .

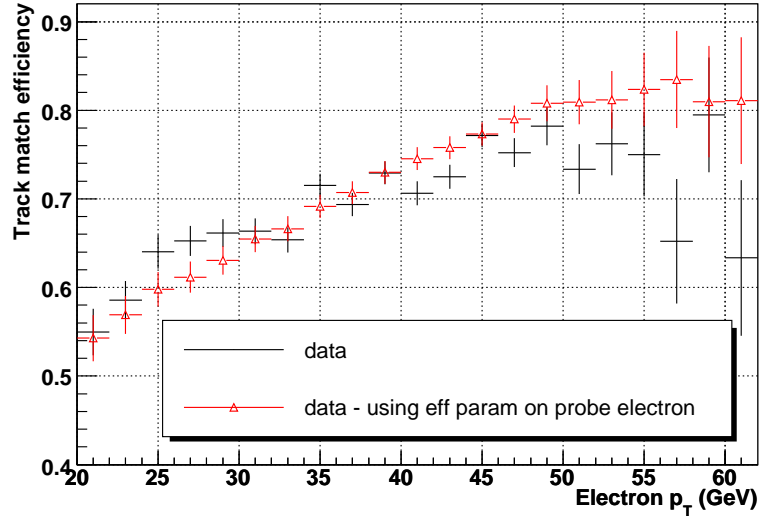


Figure 47: Track match efficiency in data for events for the  $Z$  inclusive sample vs probe electron  $p_T$  in the forward regions of the calorimeter without background subtraction. The measured efficiency (data) is matched against a 1D fit ( $p_T$ ) in the central region and a 2D fit ( $p_T, \eta_{detector}$ ) of the forward region to the probe electron. The efficiency is averaged over  $\eta$  and  $\phi$ .

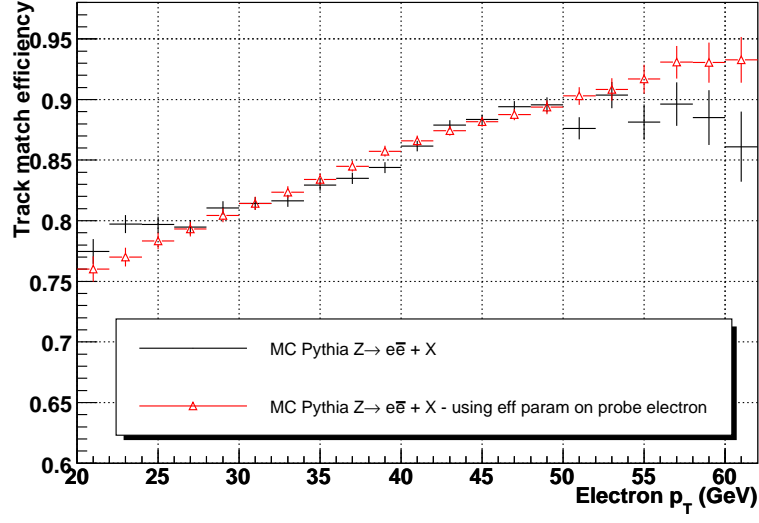


Figure 48: Track match efficiency in data for events for the  $Z$  inclusive sample vs probe electron  $p_T$  in the forward regions of the calorimeter without background subtraction. The measured efficiency (MC) is matched against a 1D fit ( $p_T$ ) in the central region and a 2D fit ( $p_T, \eta_{detector}$ ) of the forward region to the probe electron. The efficiency is averaged over  $\eta$  and  $\phi$ .

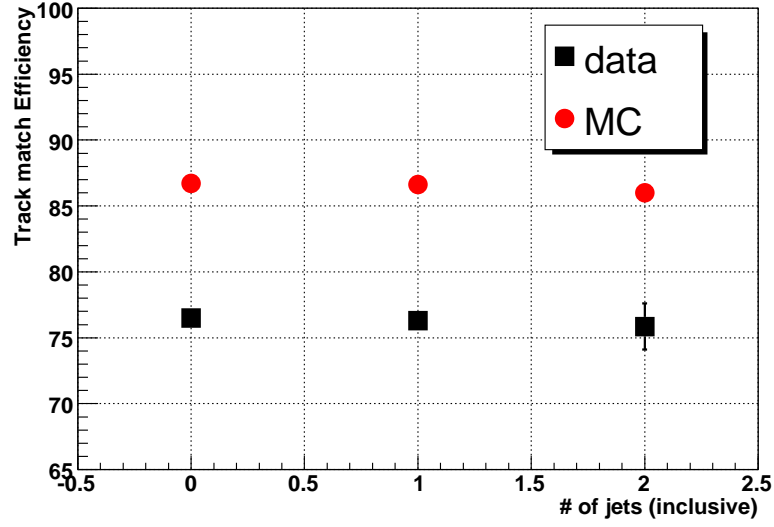


Figure 49: Track match efficiencies vs jet multiplicity for data and MC. The background in data has been removed by using the sidebands of the invariant mass peak.

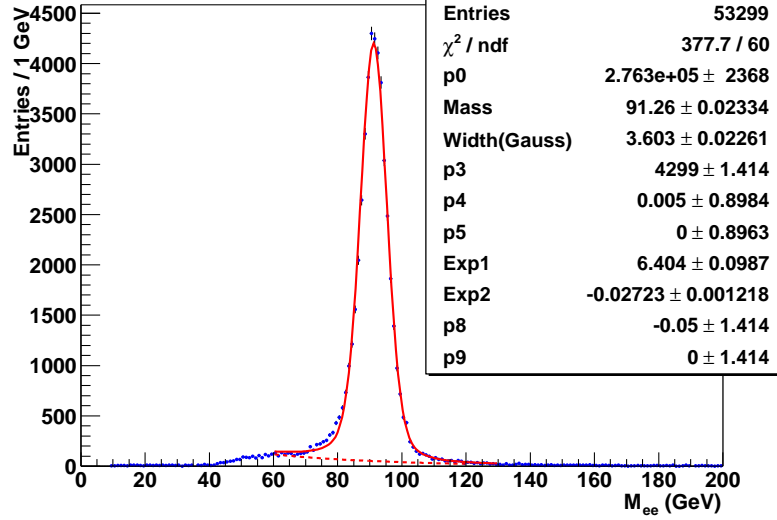


Figure 50: The invariant mass distribution for the two leading electrons for events for the  $Z$  inclusive sample for track matching efficiency in data. This invariant mass distribution is fitted with a convoluted Breit-Wigner and Gaussian shape for the  $Z$  boson with an exponential fit for the background.

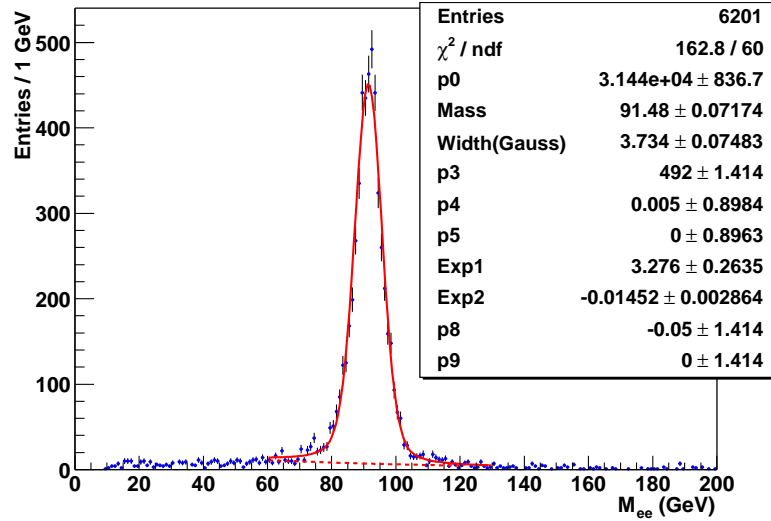


Figure 51: The invariant mass distribution for the two leading electrons for events with 1 or more jets for track matching efficiency in data. This invariant mass distribution is fitted with a convoluted Breit-Wigner and Gaussian shape for the  $Z$  boson with an exponential fit for the background.

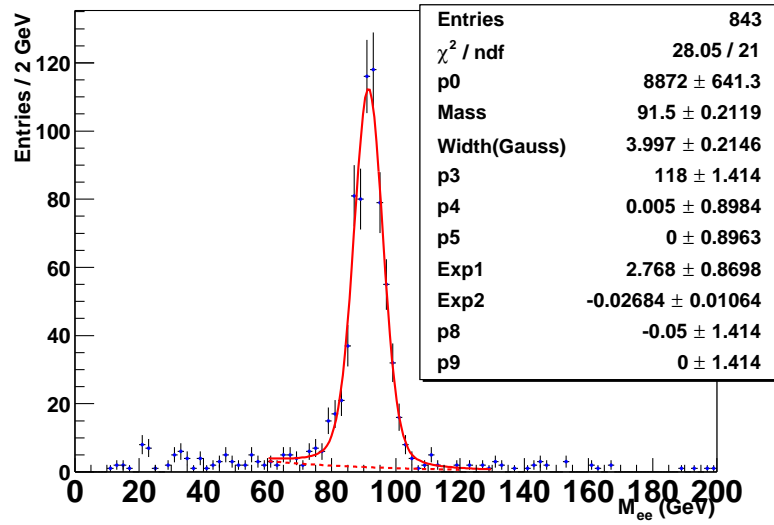


Figure 52: The invariant mass distribution for the two leading electrons for events with 2 or more jets for track matching efficiency in data. This invariant mass distribution is fitted with a convoluted Breit-Wigner and Gaussian shape for the  $Z$  boson with an exponential fit for the background.



## 4.4 Jet Reconstruction and Identification Scale Factor

The jet reconstruction and identification (jetID) efficiency was estimated using a tuned MC sample according to the following procedure [26].

- A scaling factor is derived based on the “ $Z$   $p_T$  balance” method. This method selects events with  $Z$  candidates and probes for a recoiling jet opposite in  $\phi$ . The probability of finding a recoiling jet can be measured as a function of  $Z$   $p_T$  in data and MC.
- The ratio of the  $Z$   $p_T$  probability in data and MC yields a scaling factor.
- The scaling factor is applied to the MC sample to tune it to match the data distributions.
- The tuned MC is used to measure the jetID efficiency by matching particle level jets with calorimeter jets within a search cone of  $\Delta R = 0.4$ .
- The jetID efficiency is parameterized versus particle jet  $p_T$ . The  $p_T$  values of the particles jets are smeared with the data energy resolutions.

Figures 53 through 58 show the measured efficiencies in data and MC in three regions:  $|\eta| < 0.70$ ,  $0.70 < |\eta| < 1.5$ , and  $1.5 < |\eta| < 2.5$ . The efficiencies in the MC plateau at 98% due to small inefficiencies in the jetID selection. The ratio of these curves,  $\text{eff}_{MC} / \text{eff}_{data}$ , in the three regions of pseudo-rapidity, are the scale factors applied to the MC samples. The systematic uncertainty from the jet reconstruction \* identification scale factor was determined separately for the MC  $ZH_{115}$  signal sample and all other background samples. Varying the scale factor in the analysis by  $\pm 1\sigma$  (at the level of requiring 2 b-tags and within the Higgs mass search window) gives a  $\pm 10\%$  change in the amount of  $Z$  boson plus 2 b-tagged jets for the largest background,  $Zbb$ , and a  $\pm 9\%$  change for the  $ZH_{115}$  signal.

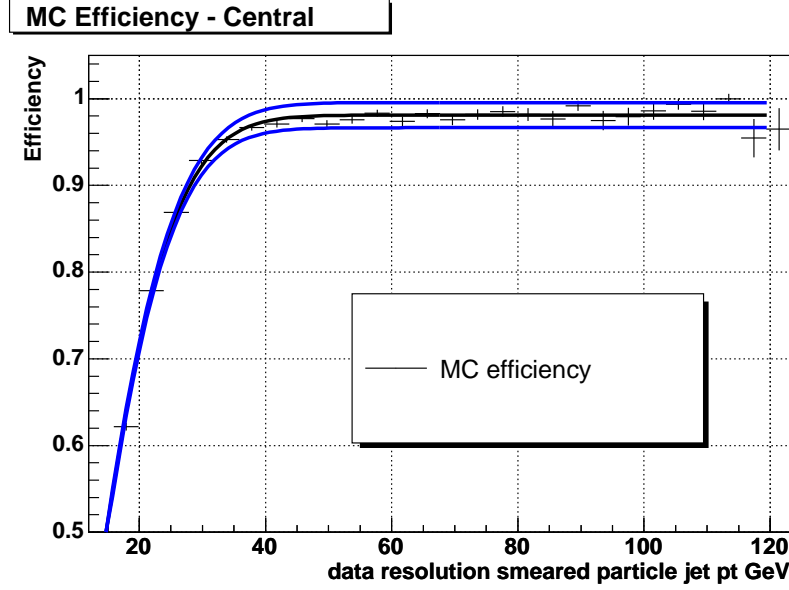


Figure 53: Jet reconstruction\*identification efficiency for MC within  $|\eta| < 0.70$  vs smeared particle jet  $p_T$ . The jet reconstruction efficiency is the probability of a particle jet to have a calorimeter jet, passing all id requirements, within  $\Delta R < 0.4$  of the particle jet. The particle jets are smeared to the full resolution of calorimeter jets in data.

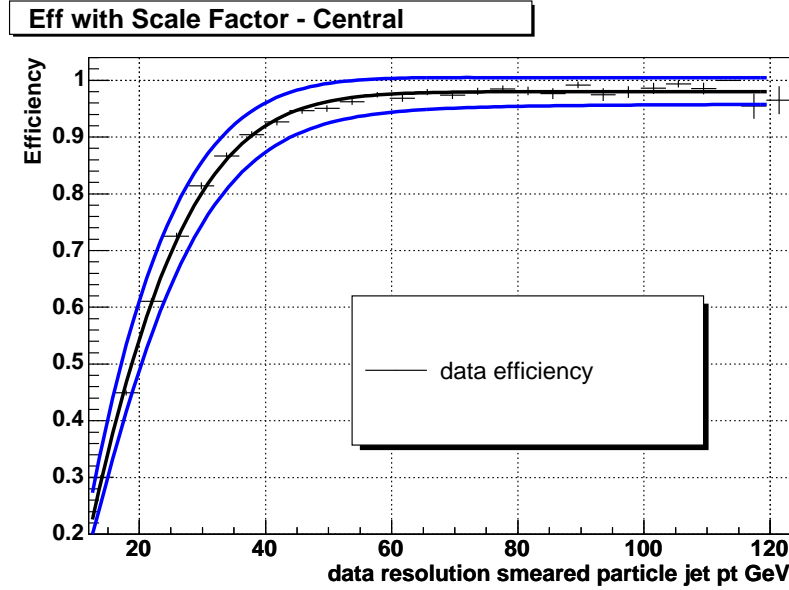


Figure 54: Jet reconstruction\*identification efficiency for data within  $|\eta| < 0.7$  vs smeared particle jet  $p_T$ . The jet reconstruction efficiency is the probability of a particle jet to have a calorimeter jet, passing all id requirements, within  $\Delta R < 0.4$  of the particle jet. The particle jets are smeared to the full resolution of calorimeter jets in data.

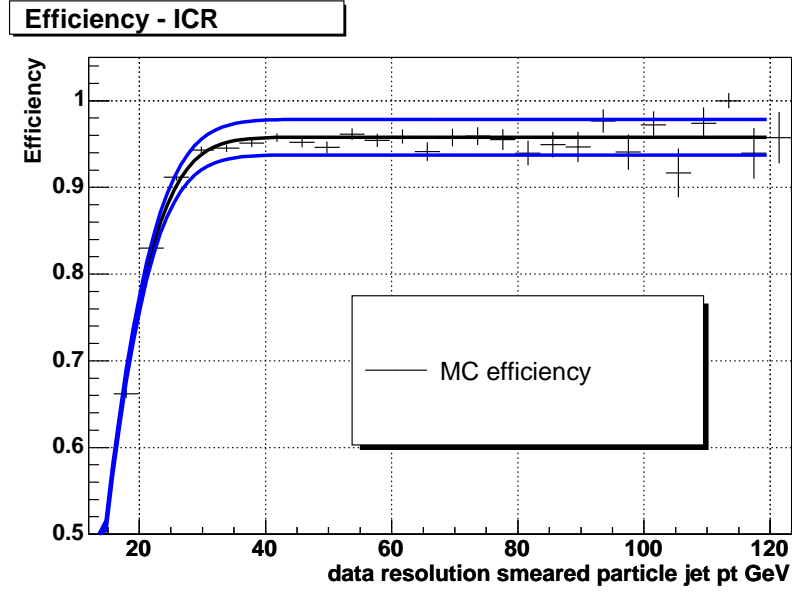


Figure 55: Jet reconstruction\*identification efficiency for MC within  $0.70 < |\eta| < 1.5$  vs smeared particle jet  $p_T$ . The jet reconstruction efficiency is the probability of a particle jet to have a calorimeter jet, passing all id requirements, within  $\Delta R < 0.4$  of the particle jet. The particle jets are smeared to the full resolution of calorimeter jets in data.

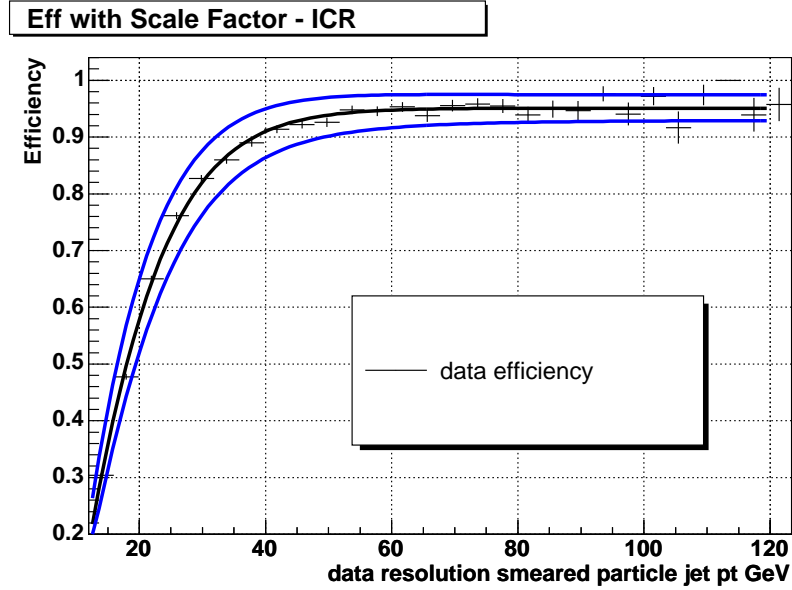


Figure 56: Jet reconstruction\*identification efficiency for data within  $0.7 < |\eta| < 1.5$  vs smeared particle jet  $p_T$ . The jet reconstruction efficiency is the probability of a particle jet to have a calorimeter jet, passing all id requirements, within  $\Delta R < 0.4$  of the particle jet. The particle jets are smeared to the full resolution of calorimeter jets in data.

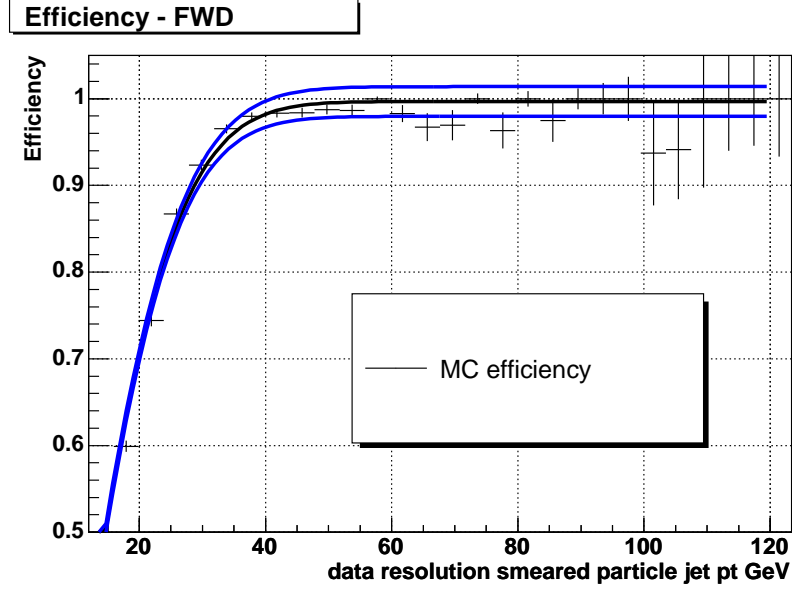


Figure 57: Jet reconstruction\*identification efficiency for MC within  $1.5 < |\eta| < 2.5$  vs smeared particle jet  $p_T$ . The jet reconstruction efficiency is the probability of a particle jet to have a calorimeter jet, passing all id requirements, within  $\Delta R < 0.4$  of the particle jet. The particle jets are smeared to the full resolution of calorimeter jets in data.

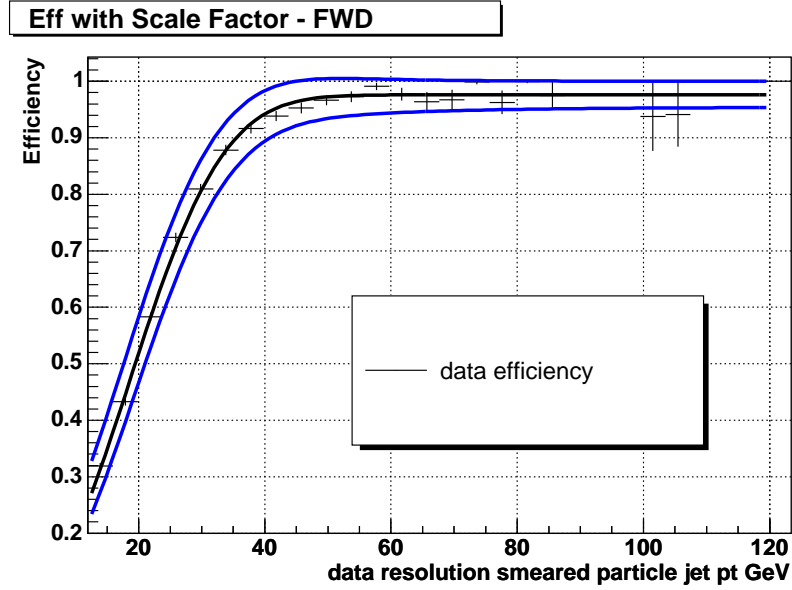


Figure 58: Jet reconstruction\*identification efficiency for data within  $1.5 < |\eta| < 2.5$  vs smeared particle jet  $p_T$ . The jet reconstruction efficiency is the probability of a particle jet to have a calorimeter jet, passing all id requirements, within  $\Delta R < 0.4$  of the particle jet. The particle jets are smeared to the full resolution of calorimeter jets in data.

## 4.5 Jet Taggability Scale Factor

The jet taggability efficiencies are parameterized by 2D functions of  $p_T$  and  $\eta$ . Figures 59 and 60 show the Zjj MC and data efficiencies. Figures 61 and 62 show the jet taggability efficiency overlaid with the 2D parameterization of each jet in data. In Zjj MC sample, Figures 63 and 64 show the jet taggability efficiency overlaid with the 2D parameterization. Figure 65 shows the average jet taggability efficiency for data and a variety of MC processes. The MC simulations with b-jets have an enhanced taggability probability. The average efficiency in data is  $78.3 \pm 0.7\%$  while Zjj MC simulation is  $89.0 \pm 0.1\%$ . The taggability efficiencies in Zjj (after applying the taggability scale factor) were compared to using the taggability efficiencies measured in a W+jets data sample [27]. The two techniques were found to be in very good agreement [28].

The uncertainty on the jet taggability scale factor was estimated by fitting the statistical uncertainty distributions from the data measurement. The statistical uncertainties are parameterized versus  $p_T$  and  $\eta$ . The  $\eta$  distribution starts at 4% in the central region and goes up to 10% in the forward regions. The  $p_T$  distribution starts at 1.5% at 20 GeV and goes up to 9% at 100 GeV. For a given  $p_T$  and  $\eta$  of a jet, an average uncertainty is added and subtracted to the jet multiplicity scale factor and propagated through the analysis. The change in the number of  $Z$  boson plus 2 b-tagged jets for all of the MC processes, including signal, was  $\pm 4\%$ .

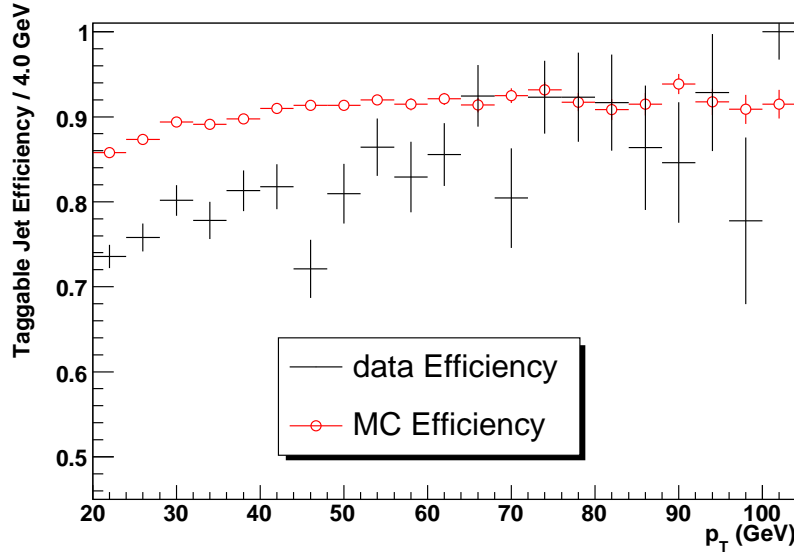


Figure 59: Taggable jet efficiency for data and MC within  $|\eta| < 2.5$  vs calorimeter jet  $p_T$ .

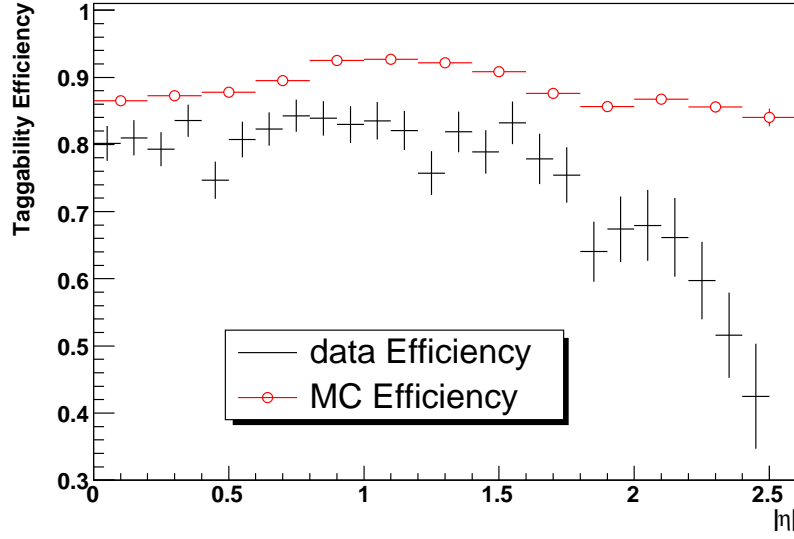


Figure 60: Taggability jet efficiency for data and MC within  $|\eta| < 2.5$  vs calorimeter jet  $|\eta|$ .

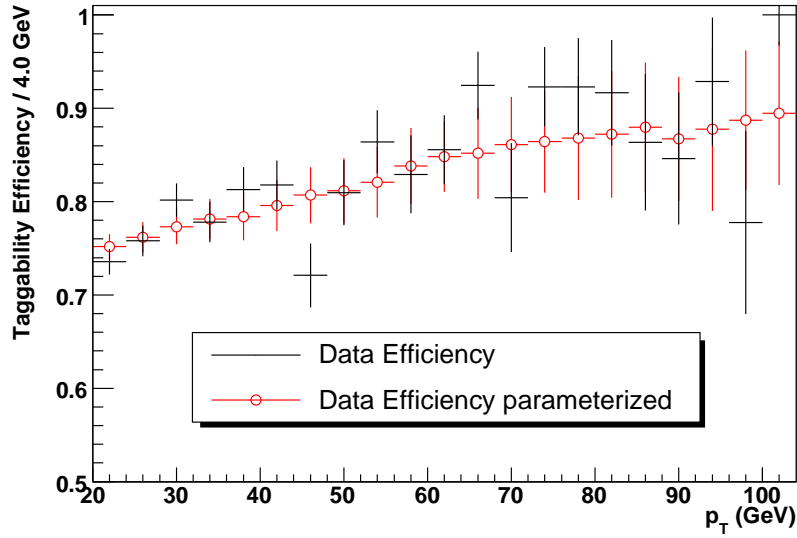


Figure 61: Taggability jet efficiency for data within  $|\eta| < 2.5$  vs calorimeter jet  $p_T$ . The open circles show the application of the 2D  $(p_T, \eta)$  parameterization curves to each jet.

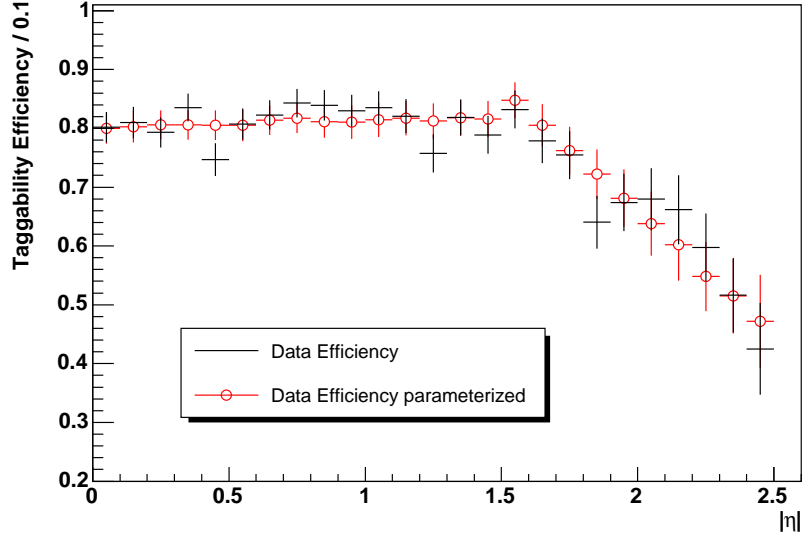


Figure 62: Taggability jet efficiency for data within  $|\eta| < 2.5$  vs calorimeter jet  $|\eta|$ . The open circles show the application of the 2D  $(p_T, \eta)$  parameterization curves to each jet.

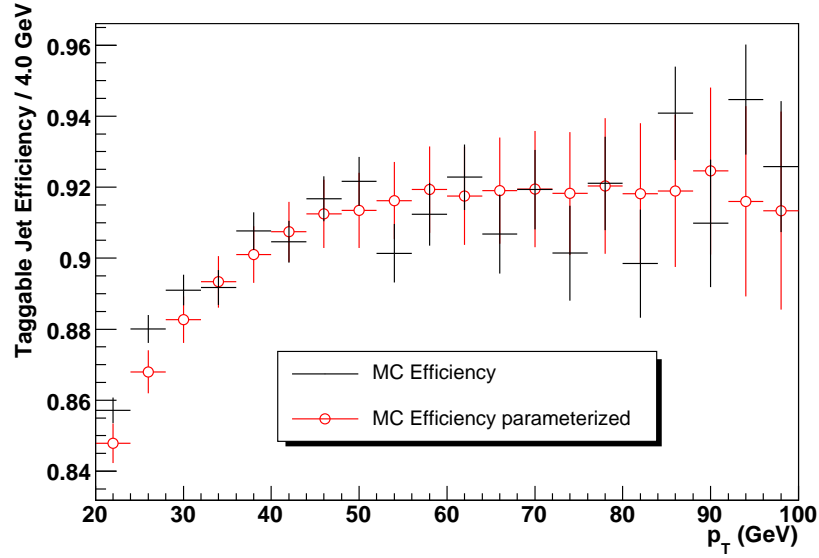


Figure 63: Taggability jet efficiency for the MC simulated  $Zjj \rightarrow e\bar{e} + jj$  within  $|\eta| < 2.5$  vs calorimeter jet  $p_T$ . The open circles show the application of the 2D  $(p_T, \eta)$  parameterization to each jet.

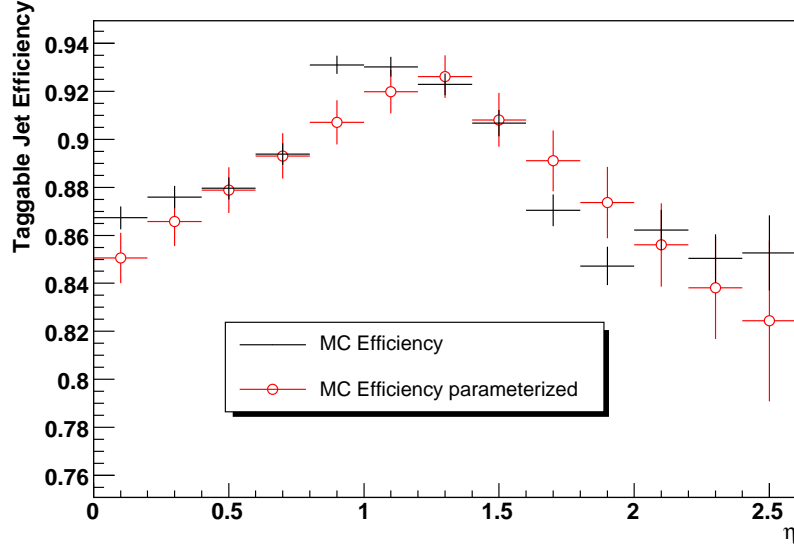


Figure 64: Taggable jet efficiency for the MC simulated  $Zjj \rightarrow e\bar{e} + jj$  within  $|\eta| < 2.5$  vs calorimeter jet  $\eta$ . The open circles show the 2D  $(p_T, \eta)$  parameterization to each jet.

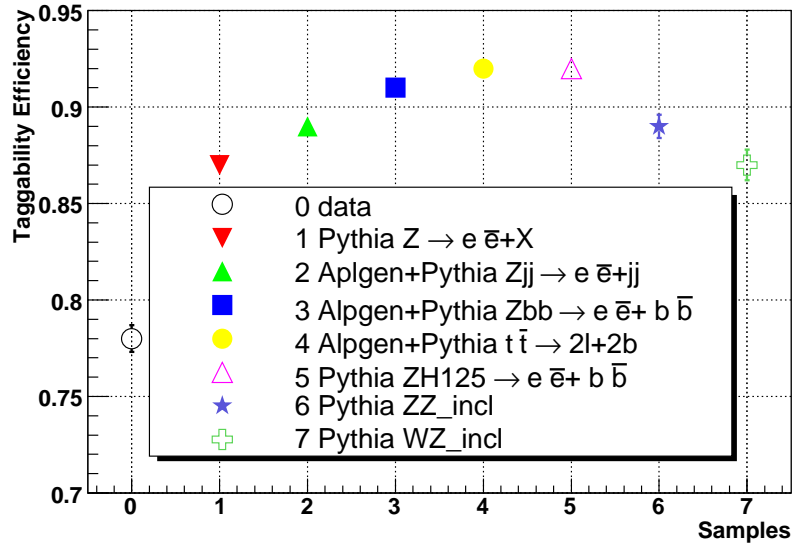


Figure 65: Average taggable jet efficiency of data and various MC samples.



## 4.6 B Tagging Scale Factor

There are six certified JLIP cuts which are compared in the following figures. Figure 66 shows the tagging rate functions or b-tagging efficiencies for b jets in data. Figure 67 shows the tagging rate functions for c-jets in data and the efficiency is roughly half of the b-tagging efficiencies. Figure 68 shows the mistag efficiencies of light quark jets, which are roughly the JLIP cut value. Figure 69 shows the certified scale factor applied to the MC simulation. Figure 70 shows the statistical and systematic b tagging uncertainties. In the analysis, the MC jets were considered b tagged if their JLIP probability value was less than the JLIP cut used, 0.001 to 0.04, and then the b tagging scale factor was applied. The validity of using the JLIP cut value versus Tagging Rate Functions (TRFs) on the MC simulated jets is shown in Figures 71 and 72. These two plots were generated using an ALPGEN+PYTHIA  $Zb\bar{b} \rightarrow e\bar{e} + b\bar{b}$  sample. All jets were required to have a B hadron or meson within  $\Delta R < 0.4$  of the jet. For the solid lines, the JLIP probability was used, and if the jet was b tagged, the JLIP scale factor was applied. For the square dots, the JLIP TRF<sub>b</sub> were applied to the jets without checking the JLIP probability value. The two techniques agree very well in the jet  $\eta$  distribution, but disagree at higher jet  $p_{Ts}$ . In a significance study in which the results are shown in Table 9, the tightest certified JLIP cut 0.001, has the largest significance for 2 or more jets with 1 b tag jets, and the loosest certified JLIP cut 0.04 has the largest significance for 2 or more jets with 2 b tag jets. Therefore, the JLIP cut of 0.04 is used when requiring two b-jets and JLIP cut of 0.001 is used when requiring 1 exclusive b-jet..

The certified JLIP b-tagging code has  $\pm 1\sigma$  uncertainties for the scale factor. The scale factor uncertainties are a function of jet  $p_T$  and  $\eta$ , as shown in Figure 70. These uncertainties were applied to the scale factor and propagated through the analysis. The change in the number of Z boson plus 2 b-tagged jets for all the MC processes, including signal, was  $\pm 7\%$ .

JLIP cut	1-b tag # events in ZH signal	1-b tag # events in background	Significance 1-b tag*100	2-b tags # events in ZH signal	2-b tags # events in background	Significance 2-b tags*100
0.001	0.070	8.34	2.39	0.012	0.88	1.31
0.003	0.080	12.24	2.31	0.019	1.44	1.62
0.005	0.084	14.70	2.19	0.023	1.81	1.72
0.01	0.093	21.28	2.02	0.028	2.44	1.81
0.02	0.100	31.27	1.78	0.036	3.19	2.03
0.04	0.103	46.36	1.51	0.044	4.22	2.16

Table 9: Significance study, number of ZH events divided by the square root of all the background processes for 1 b-tag and 2-btags using the six certified JLIP cuts.

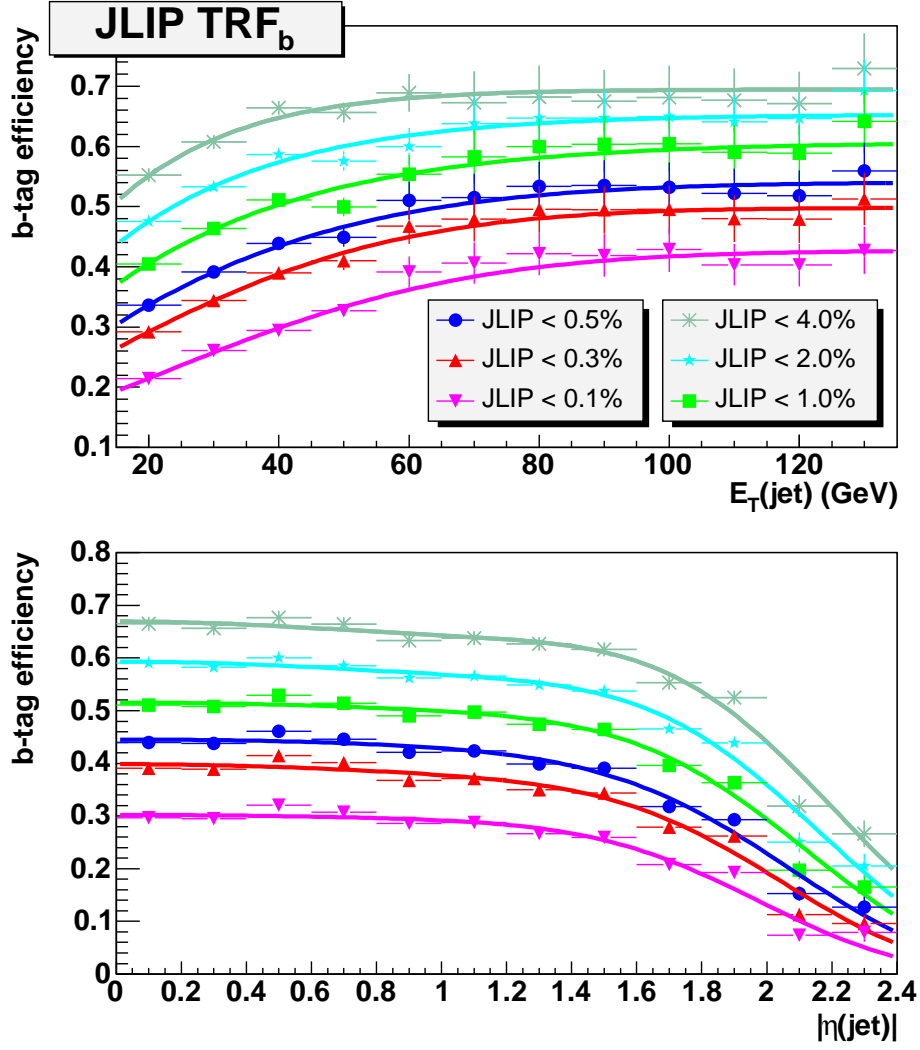


Figure 66: Tag Rate Function  $TRF_b$  for simulated inclusive b-tag jets, versus  $E_T$  and  $|\eta|$  for all six working points.

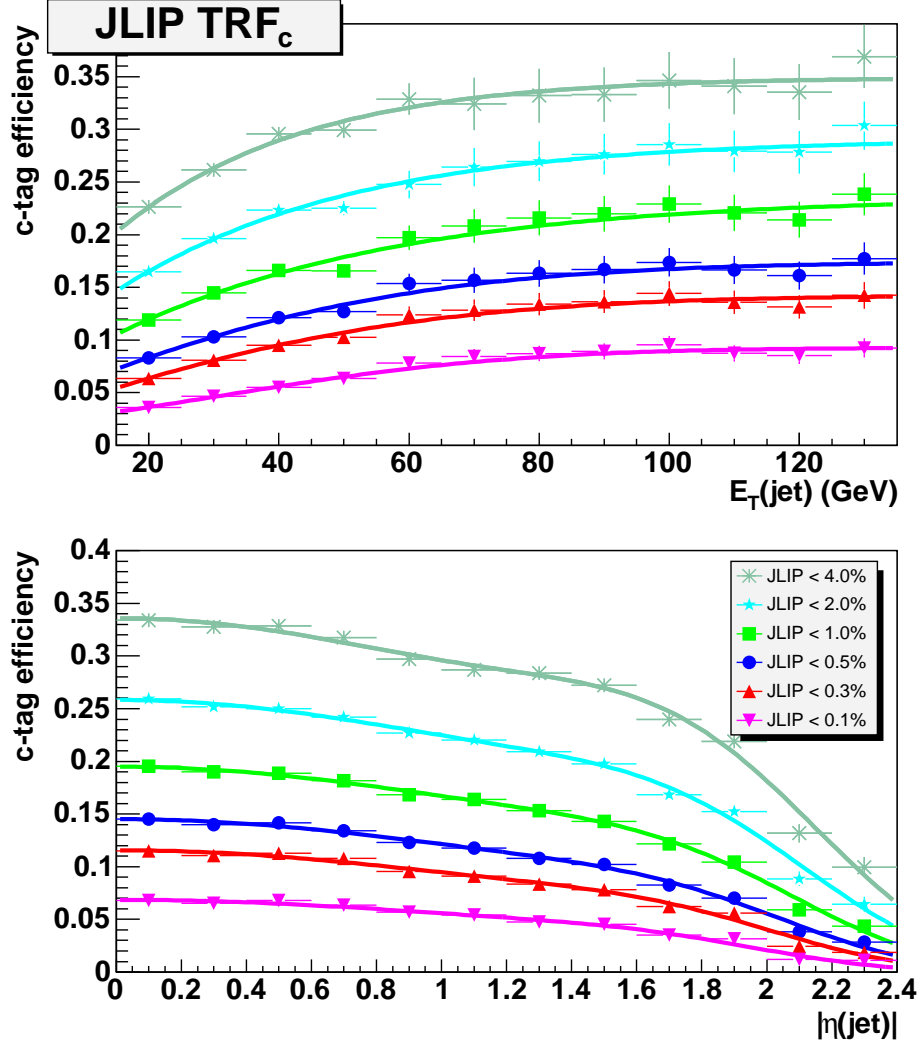


Figure 67: Tag Rate Function  $TRF_c$  for simulated inclusive c-tag jets versus  $E_T$  and  $|\eta|$  for all six working points.

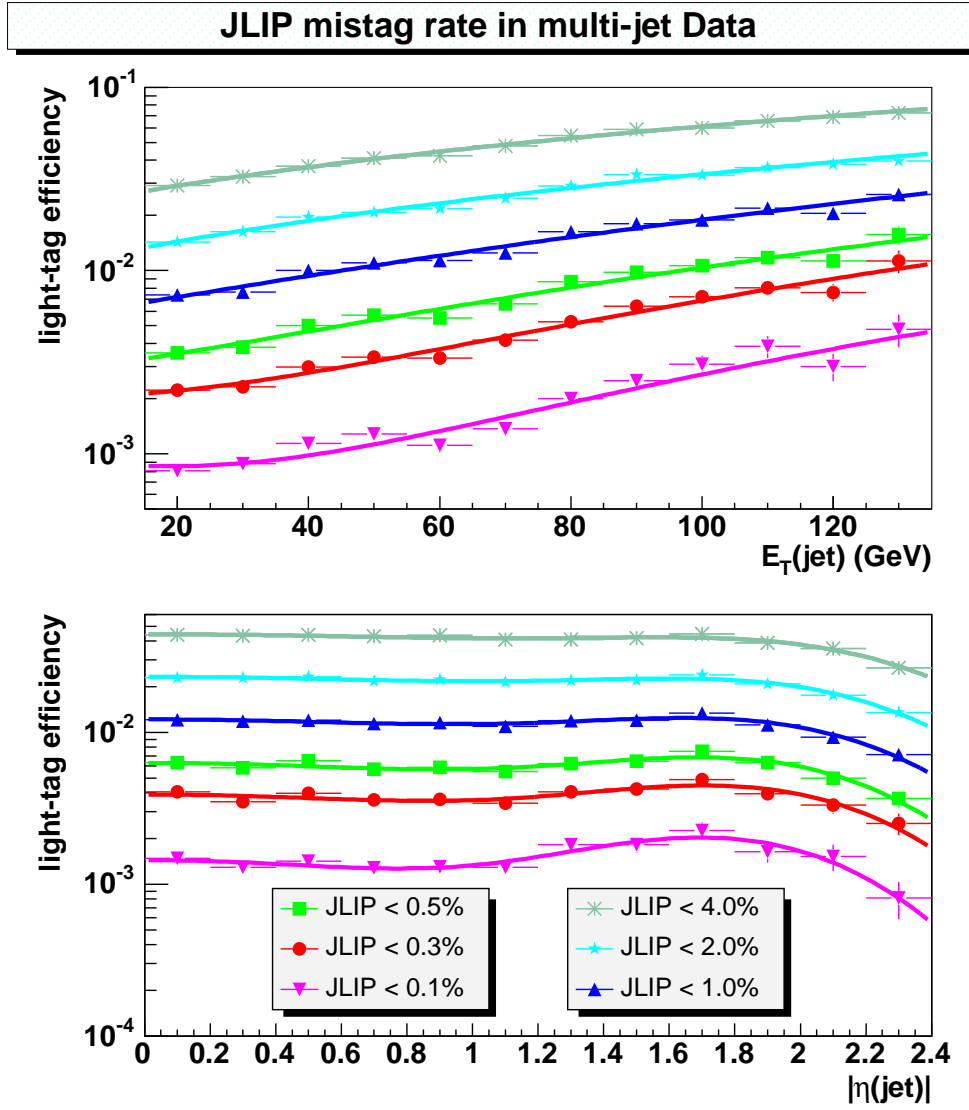


Figure 68: Light quark tagging efficiency for all six working points versus jet  $E_T$  and  $|\eta|$ .

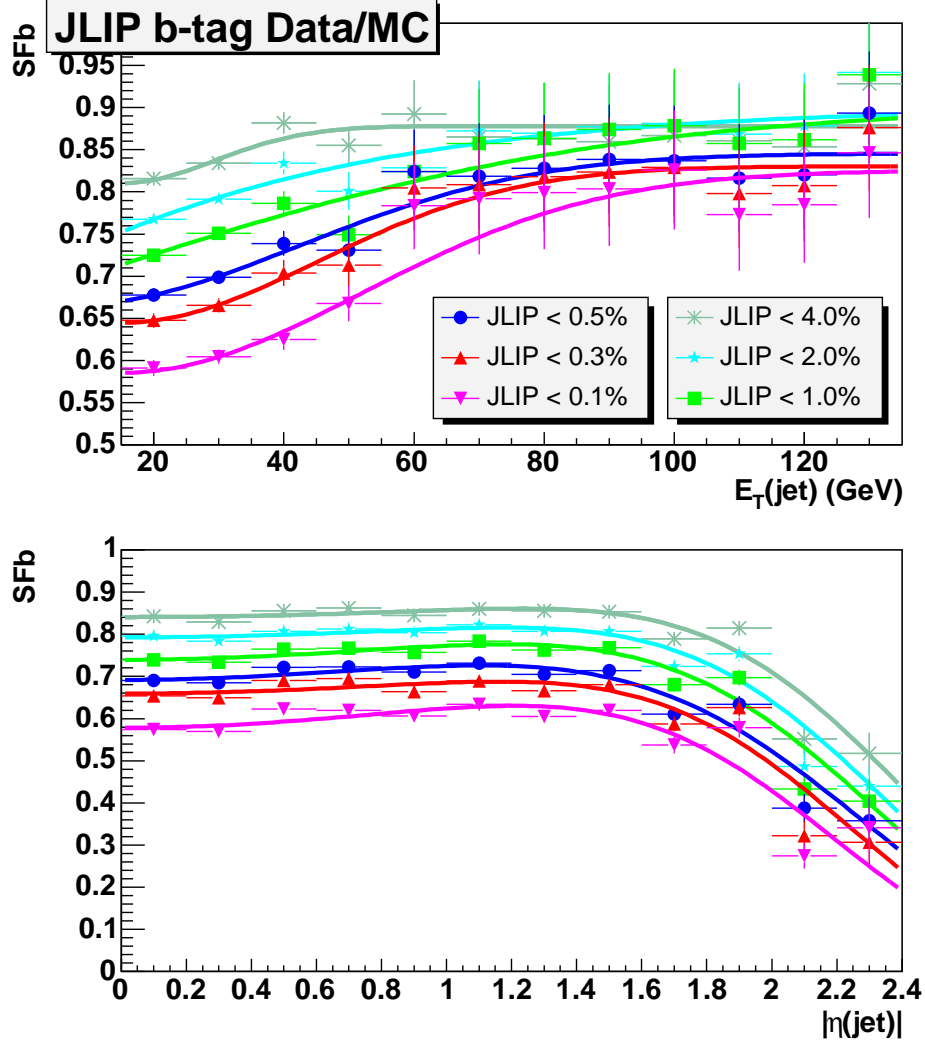


Figure 69:  $SF_b$  scale factor, ratio of the b-tagging efficiencies measured in muon-in-jet data and simulation versus the jet  $E_T$  and  $|\eta|$  for all six working points.

**JLIP TRFs : stat.  $\oplus$  syst. relative errors**

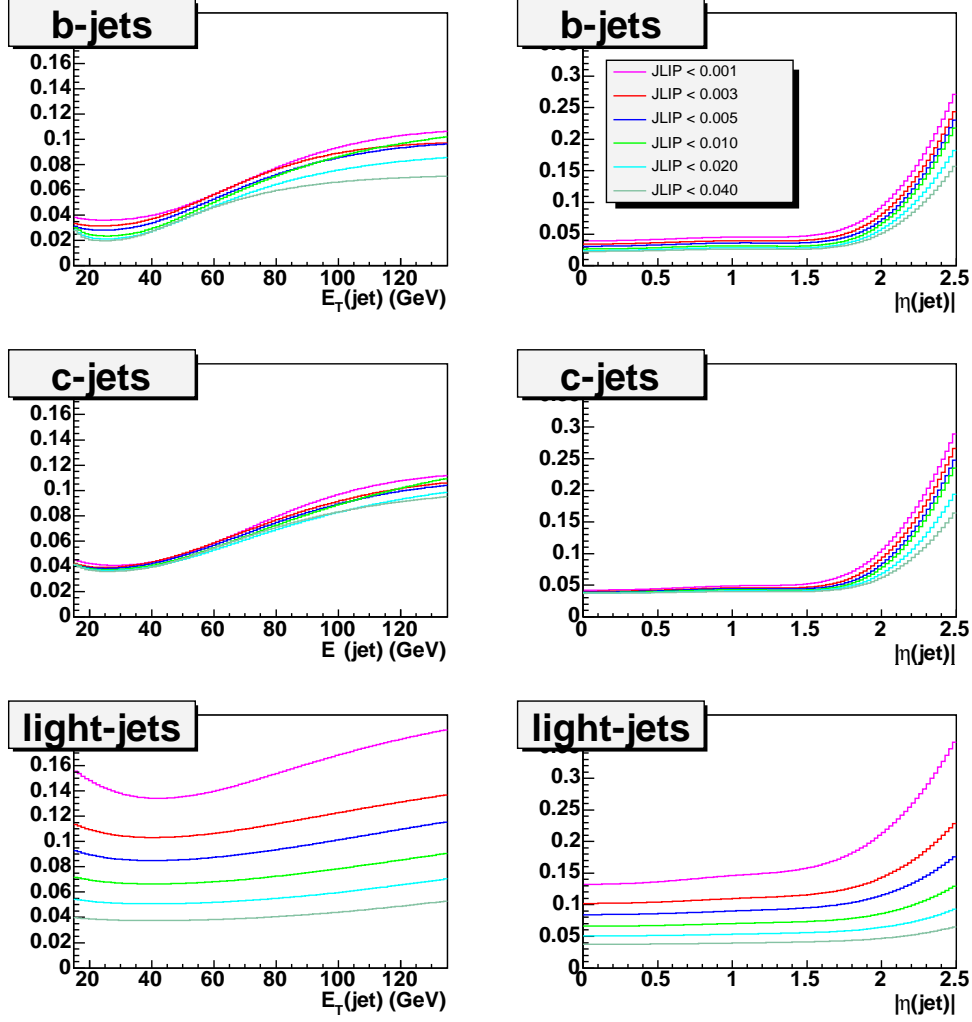


Figure 70: Overall relative uncertainties on  $TRF_b$ ,  $TRF_c$ , and  $TRF_{light}$  versus jet  $E_T$  and  $|\eta|$  for all working points. The statistical uncertainties and systematics are summed in quadrature.

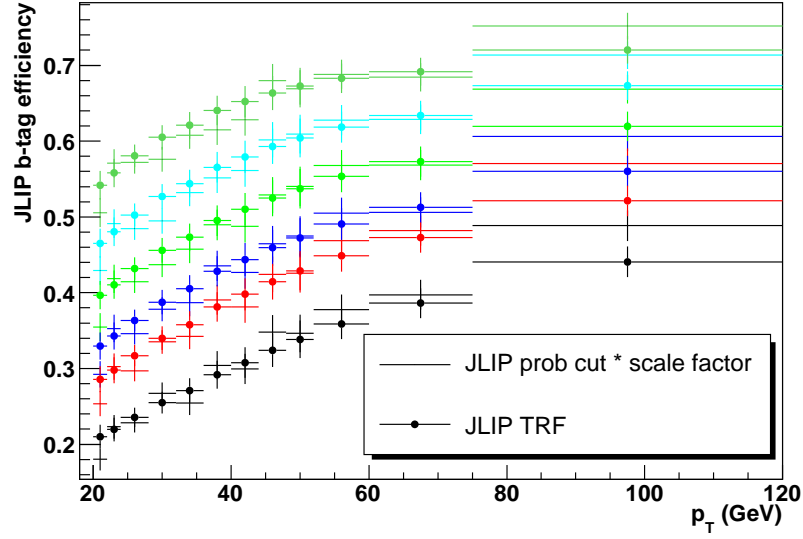


Figure 71: JLIP efficiencies for the six working points as a function of jet  $p_T$ . The solid lines use the MC JLIP probability and then the JLIP scale factor. The square points use the JLIP TRFs for b jets. The MC simulation is ALPGEN+PYTHIA  $Zb\bar{b} \rightarrow e\bar{e} + b\bar{b}$ .

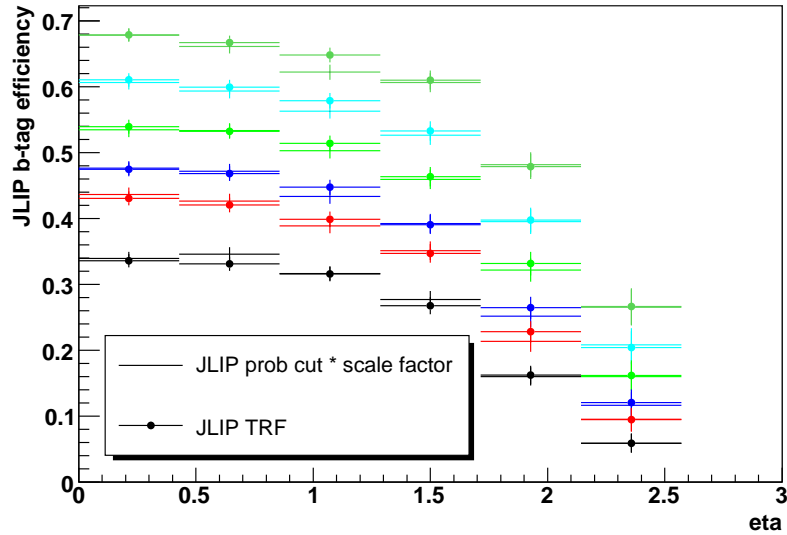


Figure 72: JLIP efficiencies for a six working points as a function of  $\eta$ . The solid lines use the MC JLIP probability and then the JLIP scale factor. The square points use the JLIP TRFs for b jets. The MC simulation is ALPGEN+PYTHIA  $Zb\bar{b} \rightarrow e\bar{e} + b\bar{b}$ .

## 4.7 QCD estimation

The QCD contribution is estimated by fitting the electron invariant mass peak with a Breit-Wigner convoluted with a Gaussian distribution, and an exponential curve for the background. The sidebands of the invariant mass peak include QCD, Drell-Yan, and a small  $Z$  boson contribution. MC simulation is used to estimate the number of Drell-Yan / (  $Z$ +Drell-Yan ) bosons expected, based on the number of events within the  $Z$  boson search window. Figure 73 shows the di-em objects invariant mass distribution in data for  $Z$  with two or more jets. The Drell-Yan plus QCD contribution is found to be  $7.78 \pm 1.29\%$  of events in the  $Z$  boson candidate search window,  $75 < M_{ee} < 105$  GeV, equation 4. Figure 74 is the di-em invariant mass distribution in MC, ALPGEN+PYTHIA  $Zjj \rightarrow e\bar{e} + jj$  for  $Z$  with two or more jets and the Drell-Yan contribution is found to be  $1.79 \pm 0.14\%$  of the events in the  $Z$  boson search window,  $75 < M_{ee} < 105$  GeV, equation 5. The Drell-Yan contribution in the data is expressed in equation 6. Plugging equation 6 into equation 4 and solving for  $N_{QCD}$  yields equation 7, the number of QCD events in data.

$$N_{(DY+QCD)} = N_{DY} + N_{QCD} \quad (4)$$

$$R_{(MC \frac{DY}{Z+DY})} = \frac{N_{MC_{DY}}}{N_{MC_{(Z+DY)}}} \quad (5)$$

$$N_{DY} = R_{MC \frac{DY}{Z+DY}} (N_{(Z+DY+QCD)} - N_{QCD}) \quad (6)$$

$$N_{QCD} = \frac{N_{(DY+QCD)} - R_{(MC \frac{DY}{Z+DY})} N_{(Z+DY+QCD)}}{1 - R_{(MC \frac{DY}{Z+DY})}} \quad (7)$$

The QCD contribution in data is found to make up  $6.10 \pm 1.46\%$  of the  $Z$  bosons in the search window. There are 463  $Z$  plus two or more jets in data, which include 28 QCD events. In order to fill electron and jet histograms a QCD enhanced sample is needed and normalized to the 28 QCD events found in data. The QCD enhanced sample is generated in data using the EM1TRK skim. The event selection is basically the same as the electron selection, except the  $\chi^2$  of H-Matrix cut is inverted. For completeness, the selection cuts are:

- ID = 10 or  $\pm 11$ ;
- EM Fraction  $> 0.9$ ;
- Isolation  $< 0.15$ ;
- $\chi^2$  of H-Matrix(7)  $> 12$  if  $|\eta_{detector}| < 1.1$ ;
- $\chi^2$  of H-Matrix(7)  $> 20$  if  $1.5 < |\eta_{detector}| < 2.5$ ;
- $p_T > 20$ ;
- No fiducial restrictions in  $\phi$ ;
- At least one electron object has  $|\eta_{detector}| < 1.1$ ;



- No track match requirements.

A QCD enhanced sample should not have a  $Z$  boson peak in the invariant mass distribution. Figures 75 and 76 show the di-em objects invariant mass distribution for the QCD enhanced sample which uses the same convoluted Drell-Yan and Breit-Wigner fit with an exponential curve for the background for events with  $Z+ \geq 0j$  and  $Z+ \geq 2j$  respectively. There is no  $Z$  boson peak, therefore this qcd enhanced sample is valid and normalized to 28 events at  $Z+ \geq 2j$  selection.

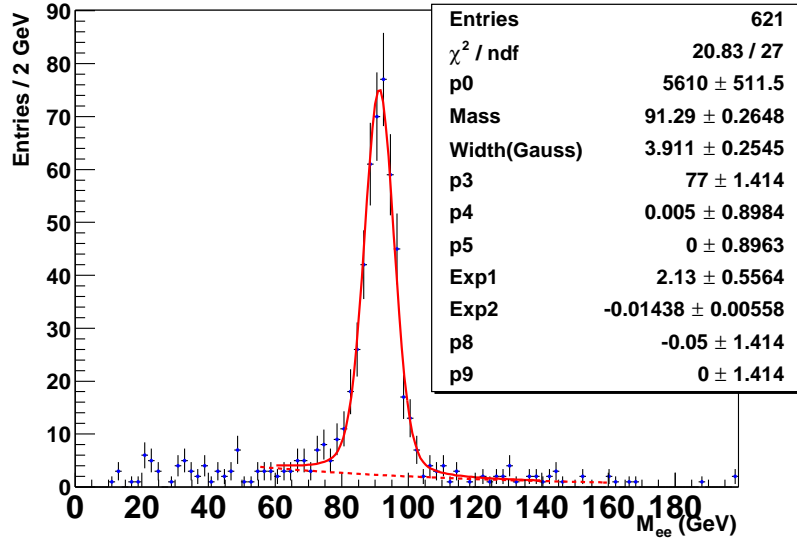


Figure 73: Di-electron invariant mass distribution for events with 2 or more jets in data. The fit is a convoluted Gaussian and Breit-Wigner with an exponential curve for the background.

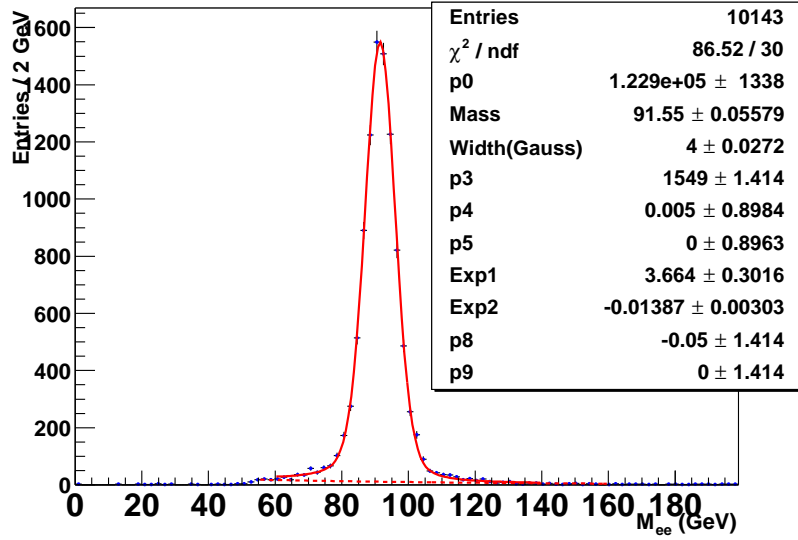


Figure 74: Di-electron invariant mass distribution for events with 2 or more jets in ALPGEN+PYTHIA MC simulated  $Zjj \rightarrow e\bar{e} + jj$ . The fit is a convoluted Gaussian and Breit-Wigner with an exponential curve for the background.

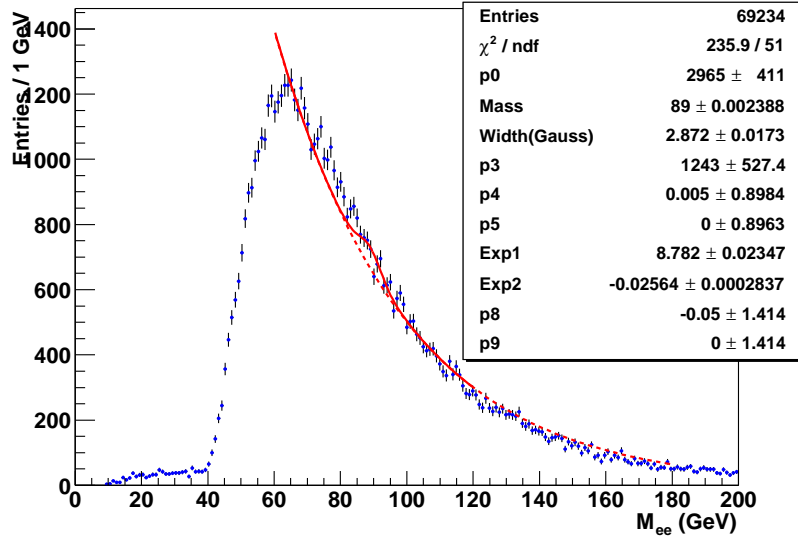


Figure 75: Di-electron object (inverted H-matrix 7 cuts) invariant mass distribution for events for the  $Z$  inclusive sample in the QCD enhanced sample. The fit is dominated by the exponential background with a convoluted Gaussian and Breit-Wigner fit in the absence of a  $Z$  boson signature.

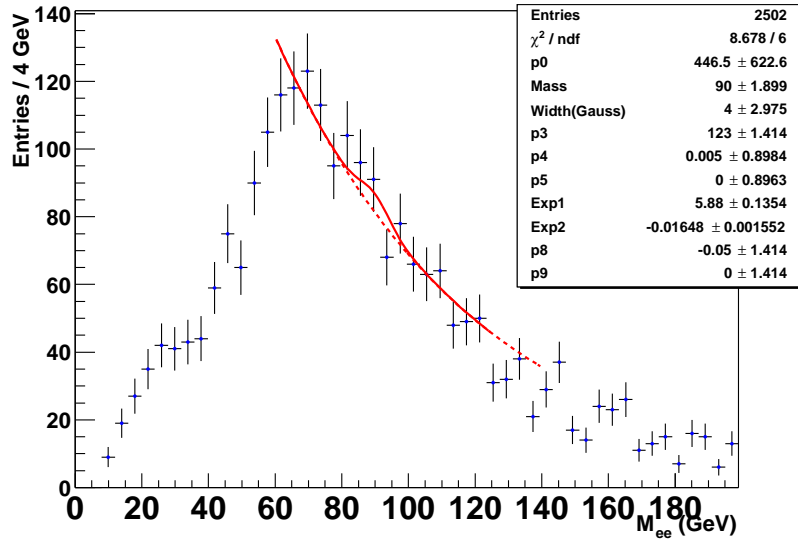


Figure 76: Di-electron object (inverted H-matrix 7 cuts) invariant mass distribution for 2 or more jets in the QCD enhanced sample. The fit is dominated by the exponential background with a convoluted Gaussian and Breit-Wigner trying to fit in the absence of a  $Z$  boson signature.

## 5 Uncertainties

The overall experimental uncertainty is 16% for  $ZH_{115}$  and 18% for  $Zb\bar{b}$  which is estimated from the following sources:

- Jet energy scale 7% (Zbb 10%);
- Jet reconstruction\*identification scale factor 9% (Zbb 10%);
- JLIP efficiency 7%;
- Trigger efficiency 1%;
- Electron reconstruction\*identification scale factor 6%;
- Track match scale factor uncertainty 1%;
- Electron energy smearing 1%;
- Jet energy smearing 2% (Zbb 3%);
- Jet taggability scale factor 4%.

**Jet Energy Scale** The uncertainty from the jet energy scale was determined using  $ZH_{115}$  signal and all of the other background processes. The jet energy scale correction factor was modified by adding in quadrature one sigma statistical and systematic uncertainties from data. The uncertainty is a function of uncorrected jet  $p_T$  and  $\eta$ . Equation 8 shows the formula to add or subtract one sigma uncertainties to the correction factor.

$$\left(1 + \frac{\pm 1\sigma}{\text{correction factor}}\right) \text{corrected jet pt} \quad (8)$$

The new  $p_T$  of the jet was propagated through jet smearing and all of the selection cuts. The percent difference in the amount of  $Z$  boson plus 2 b-tagged jets for  $Zbb$  is  $\pm 10\%$ . The signal  $ZH_{115}$  GeV has a  $\pm 7\%$  change.

**Jet reconstruction\*identification scale factor** The uncertainty from the jet reconstruction \* identification scale factor was determined using  $ZH_{115}$  signal and all of the other background processes. The data efficiency uncertainty was used to move the scale factor up or down one sigma. The uncertainty is a function of jet  $p_T$ . Applying the new scale factor in the analysis gives a  $\pm 10\%$  change in the amount of  $Z$  boson plus 2 b-tagged jets for  $Zbb$  and a  $\pm 9\%$  change for the  $ZH_{115}$  signal.

**JLIP** The certified JLIP b-tagging code has  $\pm 1\sigma$  uncertainties for the scale factor. The scale factor uncertainties are a function of jet  $p_T$  and  $\eta$ . These uncertainties were applied to the scale factor and propagated through the code. The change in the number of  $Z$  boson plus 2 b-tagged jets for all of the MC processes, including signal, was  $\pm 7\%$ .

**Trigger Efficiency** The trigger efficiency uncertainty was calculated by adding together the statistical and systematic uncertainty. The statistical event uncertainty was found to be 0.1%. A systematic uncertainty was measured by turning off the track match requirement for the probe electron. The average efficiency was lower by 0.2%. Another systematic uncertainty was estimated to be 1% from the uncertainty in the measurement of the efficiency of the  $Z+ \geq 2j$  sample. The three uncertainties are added in quadrature, propagated through the analysis code by raising and lowering the combined trigger efficiency, and give an uncertainty on the measurement of 1% for the amount of signal and background events passing all the selection cuts.

**Electron reconstruction\*identification scale factor** The uncertainty for the electron reconstruction \* identification scale factor was estimated from four sources. The first source is the difference between the  $Z+ \geq 0j$  average efficiency value and the  $Z+ \geq 2j$  average efficiency value in data, 1.8%. The second source is the statistical uncertainty of the average efficiency value for  $Z+ \geq 0j$ , 0.2%. The third source, 0.8%, is the difference between the the average efficiency value (after background subtraction) in data using a 20 GeV search window versus the average difference in the average efficiency value found by varying the  $Z$  boson search window in  $\pm 5$  GeV increments around the original search window. The fourth source is the difference between the  $Z+ \geq 0$  average efficiency value in MC and the the  $Z+ \geq 2$  average efficiency value in MC. The drop in the average MC efficiency will bring data and MC into better agreement, therefore it is only added in as a plus contribution to the uncertainty, 1.1%. The first three sources of uncertainty are added in quadrature with the fourth source added in linearly. The uncertainty to modify the scale factor is  $2.0^{+1.1}_{-0}\%$ . After using this modified scale factor and passing through all the analysis cuts, the uncertainty is found to be 6%.

**Track match scale factor** The uncertainty for the track match scale factor was estimated from four sources. The first source is the difference between the  $Z+ \geq 0j$  average efficiency value and the  $Z+ \geq 2j$  average efficiency value in data, 0.9%. The second source is the statistical uncertainty of the average efficiency value for  $Z+ \geq 0j$ , 0.3%. The third source, 0.4%, is from the difference of the average efficiency when using the errors of the exponential fit for the background subtraction of the  $Z$  peak. The fourth source is the difference between the MC  $Z+ \geq 0$  average efficiency value and the the  $Z+ \geq 2$  average efficiency value, +0.8%. The first three sources of uncertainty are added in quadrature with the fourth source added in linearly. The uncertainty to modify the scale factor is  $1.0^{+0.8}_{-0}\%$ . After using the modified scale factor and passing through all the analysis cuts, the uncertainty is found to be 1%.

**Electron energy smear** The electron energy smearing coefficients have been applied to the MC [17]. The uncertainties in their measurement were propagated through the analysis and gave a 1% uncertainty.

**Jet energy smearing** The monte carlo jets are smeared to the resolution of the jets in data [18]. The jet energy resolution fit uncertainties were propagated through the analysis and gave a 2% uncertainty for  $ZH_{115}$  and 3% for  $Zbb$ .

**Jet taggability** The jet taggability uncertainty was estimated by fitting the statistical uncertainty distributions from the data measurement. The statistical error are parameterized versus  $p_T$  and  $\eta$ . The  $\eta$  dependant uncertainty starts at 4% in the central region and goes up to 10% in the forward regions. The  $p_T$  dependant uncertainty starts at 1.5% at 20 GeV and goes up to 9% at 100 GeV. For a given  $p_T$  and  $\eta$  of the jet, an average uncertainty is added and subtracted to the scale jet multiplicity scale factor and propagated through the analysis code. The change in the number of  $Z$  boson plus 2 b-tagged jets for all of the MC processes, including signal, was 4%.

**MC cross section uncertainty** The uncertainty of the predicted MC simulated events is summarized in Table 10.

Monte Carlo	Uncertainty
$t\bar{t}$	8%
WZ	6%
ZZ	6%
$Zb\bar{b}$	19%
$Zjj$	7%
$ZH_{115}$	7%

Table 10: Monte Carlo cross section uncertainties.

**$t\bar{t}$**  The  $t\bar{t}$  cross section is calculated to be  $6.2 \pm 0.53$  pb for  $M_t = 175$  GeV [30]. Also taking into account the mass dependence (0.11 pb per GeV), for the current uncertainty of  $M_t$  measurement  $\pm 2.9$  GeV, the uncertainty is  $\pm 0.42 \pm 0.32$  pb. By adding the two uncertainties in quadrature, the total uncertainty is  $\pm 0.53$  pb, which is equivalent to an 8% uncertainty.

**ZZ or WZ** The WW cross section is quoted as  $12.4 \pm 0.8$  pb in [31], which is a 6% uncertainty. The WZ and ZZ is assumed to have a similar uncertainty.

**$Zjj$**  The amount of  $Zjj$  events is determined to be the number of events in data subtracted by the other background contributions, therefore, no uncertainties on the  $Zjj$  cross section has been used. Instead a normalization uncertainty is calculated based on the determination of the number of  $Zjj$  events in data and the uncertainty in the flavor composition of the  $Zjj$  sample.

The number of  $Zjj$  is estimated to be  $416.4 = N_{obs}(463) - QCD(28) - \Sigma BG(18.6)$ , where  $N_{obs}$  is the number of events in data and BG represents each background source besides  $Zjj$  and  $QCD$ . The statistical uncertainty on the total number of observed events is 21.5 events. The uncertainty in the amount of QCD events is 7 events. The uncertainty in the background contributions comes from summing the cross section uncertainties for each BG sample and is 2.2 events. Adding these three uncertainties in quadrature gives an error of 5.5% with respect to the 416.4  $Zjj$  events.

The second uncertainty is in terms of the flavor composition of the  $Zjj$  sample,  $Zbb/Zjj$ ,  $Zcc/Zjj$ ,  $Zbj/Zjj$ , and  $Zcj/Zjj$ . The *alpgen* generator performs leading order calculations, therefore, the uncertainty is evaluated using MCFM LO calculations. The scale uncertainties are obtained by averaging the difference between the two scales,  $M_Z/2$  and  $2 \times M_Z$ . The uncertainty associated with the PDF is assigned by taking the differences between CTEQ5L and CTEQ6L. There is no  $Zbj$  nor  $Zcj$  process available in MCFM, therefore the same error for  $Zbb$  and  $Zcc$  processes are used. The relative uncertainties are 1.9% for  $Zbb/Zjj$  and 4.7% for  $Zcc/Zjj$ . The weighted average is calculated based on the flavor composition from the MCFM LO calculations, and b-tagging efficiencies for b-, c-, and light-jets used in the analysis. The uncertainty for the exclusive single b-tagged sample is 3.7% and 4.9% for the double b-tagged sample. These errors are multiplied by the K-factor of 1.7 for a NLO approximation and result in 6.6% and 7.4% for exclusive single b-tagged and double b-tagged samples.

Adding the error due to normalization, 5.5% and the flavor composition in quadrature, gives a total normalization error of 7%.

**Zbb** The theoretical Zbb cross section is quoted as  $3.74 \pm 0.45 \pm 0.12 \pm 0.15$  pb with variations from the renormalization scale, the factorization scale, and the parton distribution functions, respectively [32]. The variations are added linearly and give a 19% uncertainty.

**QCD** The QCD background was estimated by using a Gaussian convoluted with Breit-Wigner with an exponential for QCD and Drell Yan. The uncertainty of the exponential fit of the Drell Yan contribution in the MC is 7.9%. The uncertainty of the exponential fit of the Drell-Yan and QCD (in data) is 16.6%. Adding the two uncertainties linearly gives an overall uncertainty of 25%.

**Statistical Uncertainty** Statistical uncertainties of the MC samples at the final selection cuts of exclusive 1 b-tagged jet and 2 b-tagged jets are shown in Table 11. The binomial statistical errors are dominated by how efficient the MC processes are in passing all the selection cuts.

The uncertainties of the cross sections, experimental, and statistical are added in quadrature to give the final uncertainty per sample, Table 12. The errors shown are for  $ZH_{115}$  but they are all recalculated for the 4 other Higgs search windows. The JES and Jet Reco\*id have smaller error for the MC Signal samples as the Higgs mass window increases.

Monte Carlo	1b(%)	2b(%)
ZH <sub>115</sub>	8.4	6.5
Zb $\bar{b}$	6.3	6.2
Zjj	16	33
t $\bar{t}$	11	9
ZZ	23	18
WZ	41	58
QCD	32	50

Table 11: Statistical uncertainty using binomial statistics. The mean is  $\mu$  = number MC generated events \* acceptance and variance  $\pm\sigma^2$  = number of MC generated events \* acceptance \* (1 - acceptance). The acceptance is the percent of events left after the final selection cuts of 1 exclusive b-tag or 2 b-tags. The statistical error is  $\sigma/\mu$ .

Monte Carlo	1b(%)	2b(%)
t $\bar{t}$	23	21
WZ	45	61
ZZ	30	26
Zb $\bar{b}$	27	27
QCD	44	59
Zjj	18	34
ZH <sub>115</sub>	19	19

Table 12: Overall signal and background uncertainties.



## 6 ZH Cross Section Limit

In order to calculate the ZH cross section limit, a Higgs signal search window must be established. As the expected Higgs mass increases, the search window scans along the di-jet invariant mass distribution. Using a Gaussian fit to the double b-tagged dijet invariant mass distribution of  $ZH_{115}$ , Figure 77, yields a mean of 98 GeV and a width of 17 GeV, which gives a resolution of 18%. Table 13 lists the mean, width, resolution values, and the search windows ( $\pm 1.5\sigma$ ) for the 5 ZH simulated samples. The average resolution of the 5 samples is 18% and the same search window can be used for exclusive single b-tagged events. The di-jet invariant mass is approximately 85% lower than the parton generated Higgs mass due to the jet energy scale. The jet energy scale corrects back to the particle level. The jet particle level is after final state radiation and hadronization. A parton level jet energy scale correction would be needed to be able to reconstruct the original generated Higgs mass.

The following selection cuts are applied to the data and MC simulation:

- Primary vertex  $< \pm 60$  cm along the Z axis from the center of the detector;
- The event passes the trigger (the trigger effects were applied to the MC);
- At least two electrons with  $p_T > 20$  GeV within  $|\eta_{detector}| < 1.1$  or  $1.1 < |\eta_{detector}| < 2.5$ ;
- At least one of the electrons is within  $|\eta_{detector}| < 1.1$ ;
- At least one of the electrons has a track match;
- $75 \text{ GeV} < M_{ee} < 105 \text{ GeV}$ ;
- At least two jets with  $p_T > 20$  GeV with  $|\eta| < 2.5$ ;
- At least two taggable jets;
- At least two b-tagged jets;
- Or an exclusive single b-tagged jet.

A series of data to MC comparison plots are made at the  $Z + \geq 2$  jets selection cut level. A Higgs mass of 115 GeV was chosen for the signal sample to make the comparisons. Electron distributions are shown in Figure 78. Z boson distributions are shown in Figure 79. Jet distributions are shown in Figures 80 through 82.

The  $p_T$  of all jets,  $H_T$  (sum of the two leading jets),  $\Delta R$  between the two leading jets, and the invariant mass of the two leading jets are shown in Figure 83. The same four distributions, with the additional requirement of exclusive single b-tagging are shown in Figure 84. The same four distributions, with the additional requirement of at least 2 b-tagged jets are shown in Figure 85. The log scale is shown for these four distributions for exclusive single b-tag and double b-tag in Figures 86 and 87.

Table 14 contains a summary of the acceptance of the MC signal and various background contributions for the selection cuts. The acceptance of the  $ZH_{115}$  signal sample is 4.7% to pass all the selection cuts (Higgs mass search window with 2 b-tags). Table 15

contains a summary of the individual and total MC contributions for  $Z + \geq 2$  jets,  $Z + \geq 2$  taggable jets,  $Z + 1$  b-tag exclusive, and  $Z + \geq 2$  b-tags. There are 463  $Z + \geq 2$  jets in data, 10 exclusive single b-tag in data while  $6.1 \pm 1.3$  in the simulation, and 5 double b-tag events while  $4 \pm 1$  in the simulation. For the cleanest sample, double b-tag,  $Zbb$  is roughly 40% of the total background followed by  $Zjj$  at 30% and  $t\bar{t}$  production at 17%.

Table 16 contains a summary of the amount of events found in each of the 5 Higgs mass windows after the exclusive single b tag cut. A 95% confidence level upper cross section limit is obtained using a Bayesian approach [34] that takes statistical and systematic uncertainties into account. There are 3 events in data and  $2.3 \pm 0.5$  background events, while  $0.03 \pm 0.01$  MC signal events for a 115 GeV Higgs. The efficiency shown in the table is defined as the signal acceptance 2.5% times the branching ratio of a  $Z$  boson into electrons 3.363% [35]. Table 17 is a summary of the amount of events found in each of the 5 Higgs mass windows after the double b-tag cut. For a Higgs mass of 115 GeV, there are  $1.7 \pm 0.4$  background events, 1 data events, and  $0.06 \pm 0.01$  signal events. The signal efficiency is  $0.16 \pm 0.03\%$  which translates into a cross section limit for  $\sigma(p\bar{p} \rightarrow ZH) \times B(H \rightarrow b\bar{b})$  of 6.2 pb (17.4 pb) at the 95% C.L. upper limit for double tag (single tag) at a Higgs boson mass of 115 GeV. Figure 88 summarizes the cross section limit for exclusive single b-tag and double b-tag. These cross section limits are compared to the standard model predictions and a CDF Run I cross section limit [36]. Figure 89 compares the expected 95% C.L. upper limit and the observed C.L. event displays for the five double b-tagged data events are shown in Figures 90 through 94.

Higgs mass (GeV)	mean (GeV)	width (GeV)	width/mean (%)	search window
105	89	16	18	65 – 113
115	98	17	18	72 – 125
125	106	20	19	75 – 136
135	112	21	18	82 – 143
145	122	23	19	87 – 156

Table 13: Invariant mass resolutions obtained by a Gaussian fit. An average relative resolution is found to be 18%. The higgs search windows are centered on the mean and span  $\pm 1.5\sigma$ .

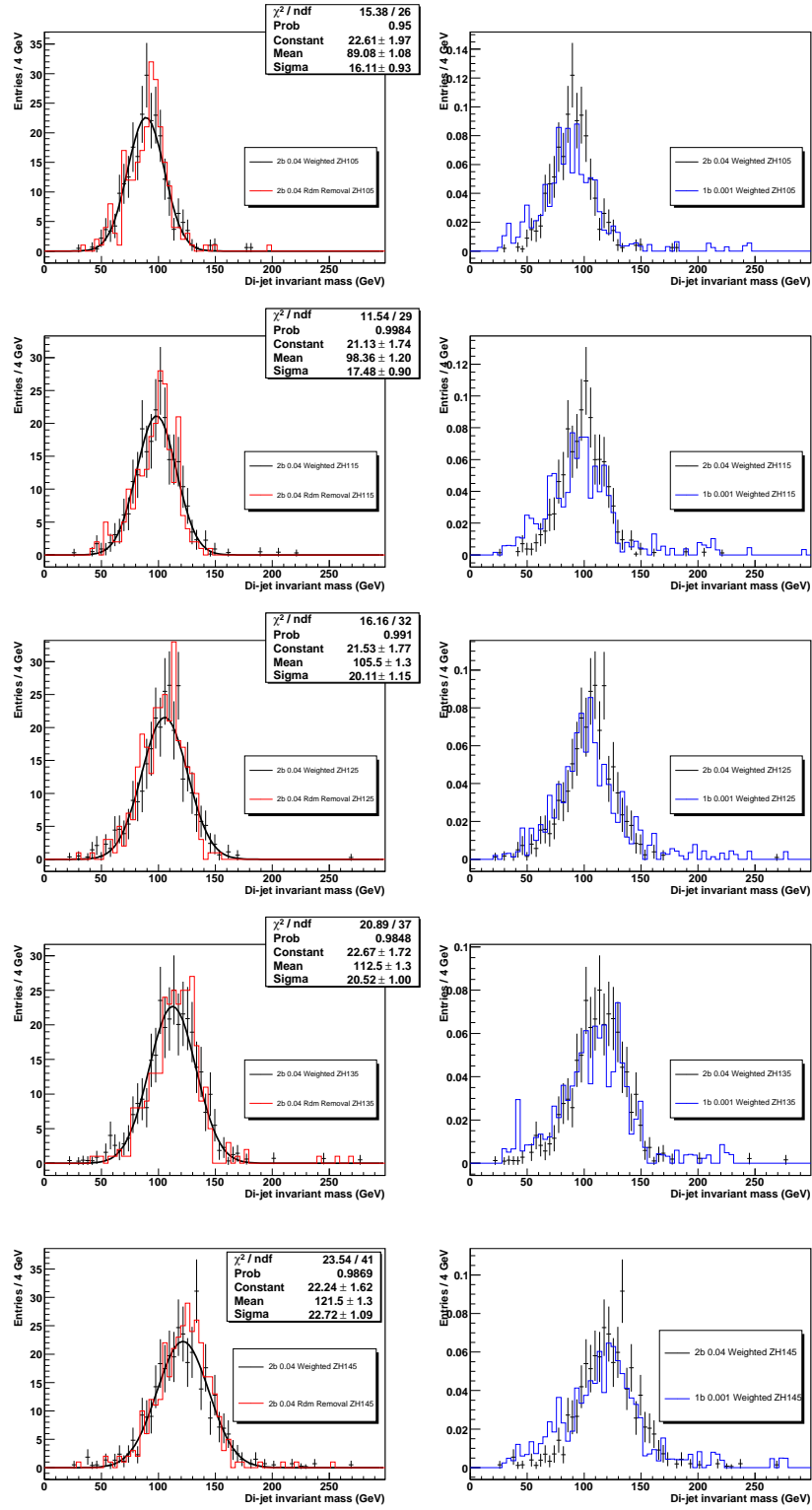


Figure 77: The resolutions of the higgs mass given two b-tagged jets. The distributions on the left have a gaussian fit for each ZH sample. The invariant mass distributions on the right compare double b-tagged jet events overlaid with exclusive single b-tag jet events.

selection cut	ZH (%)	Zbb (%)	Zjj (%)	tt <sub>2b2l</sub> (%)	ZZ (%)	WZ (%)	tt <sub>2b2j1l</sub> (%)
2 electrons $p_T > 20$ GeV	33.7	30.8	28.2	4.1	2.1	1.1	0.23
75 < $M_{ee}$ < 105 GeV	31.7	28.5	26.2	1.1	1.9	0.93	0.068
2 jets $p_T > 20$ GeV	18.9	4.0	3.7	0.67	0.60	0.30	0.058
2 taggable jets	14.3	2.9	2.5	0.51	0.43	0.20	0.050
1 b tag	3.5	0.74	0.028	0.15	0.036	0.0064	0.015
1b 75 < $M_{jj}$ < 125 GeV	2.5	0.27	0.0009	0.055	0.024	0.0034	0.0061
2 b tags	5.1	0.85	0.010	0.22	0.040	0.0025	0.014
2b 75 < $M_{jj}$ < 125 GeV	4.7	0.28	0.0004	0.077	0.022	0.0010	0.0048
selection cut	ZH 105 (%)	ZH 115 (%)	ZH 125 (%)	ZH 135 (%)	ZH 145 (%)		
2 electrons $p_T > 20$ GeV	33.3	33.7	33.8	32.6	34.4		
75 < $M_{ee}$ < 105 GeV	31.6	31.7	31.6	30.4	32.2		
2 jets $p_T > 20$ GeV	17.8	18.9	21.0	21.5	23.1		
2 taggable jets	14.2	14.3	16.2	16.9	18.5		
1 b tag	3.6	3.5	4.4	4.7	4.8		
1b $M_{jj}$ window	2.7	2.5	3.3	3.5	3.5		
2 b tags	5.4	5.1	6.3	6.6	7.6		
2b $M_{jj}$ window	4.6	4.7	5.5	5.7	6.7		

Table 14: The acceptance of the five MC signal samples and the MC backgrounds (in %).

	Z+ $\geq 2$ jets	Z+ $\geq 2$ jets taggable	Z+ 1 B tag exclusive	Z+ 2 B tags
tt	$2.7 \pm 0.5$	$2.2 \pm 0.4$	$0.47 \pm 0.09$	$0.83 \pm 0.16$
WZ	$5.0 \pm 0.9$	$3.4 \pm 0.6$	$0.11 \pm 0.04$	$0.04 \pm 0.02$
ZZ	$4.2 \pm 0.8$	$3.0 \pm 0.6$	$0.26 \pm 0.07$	$0.28 \pm 0.07$
Zbb	$9.4 \pm 2.4$	$6.7 \pm 1.7$	$1.71 \pm 0.44$	$1.97 \pm 0.51$
qcd	$28.0 \pm 8.5$	$18.5 \pm 5.7$	$0.44 \pm 0.19$	$0.18 \pm 0.10$
Zjj	$413.7 \pm 86.3$	$277.4 \pm 57.9$	$3.09 \pm 0.73$	$1.15 \pm 0.31$
Total Exp.	$463.0 \pm 94.5$	$311.5 \pm 63.5$	$6.07 \pm 1.31$	$4.45 \pm 0.95$
Data	463	317	10	5
ZH	$0.24 \pm 0.04$	$0.18 \pm 0.03$	$0.08 \pm 0.006$	$0.065 \pm 0.0011$

Table 15: Summary of the ZH analysis with single b-tagging exclusive and double b-tagging before requiring the di-jet invariant mass to be within the Higgs mass search window.

ST	105 GeV	115 GeV	125 GeV	135 GeV	145 GeV
ZH	$0.048 \pm 0.009$	$0.032 \pm 0.006$	$0.027 \pm 0.005$	$0.017 \pm 0.003$	$0.008 \pm 0.0013$
Zbb	$0.63 \pm 0.17$	$0.64 \pm 0.17$	$0.69 \pm 0.18$	$0.62 \pm 0.16$	$0.60 \pm 0.16$
Zjj	$1.19 \pm 0.31$	$0.99 \pm 0.26$	$1.03 \pm 0.27$	$1.11 \pm 0.29$	$1.03 \pm 0.27$
tt	$0.21 \pm 0.05$	$0.24 \pm 0.05$	$0.27 \pm 0.06$	$0.26 \pm 0.06$	$0.28 \pm 0.06$
ZZ	$0.17 \pm 0.05$	$0.17 \pm 0.05$	$0.18 \pm 0.05$	$0.14 \pm 0.04$	$0.13 \pm 0.04$
qcd	$0.18 \pm 0.08$	$0.18 \pm 0.08$	$0.27 \pm 0.12$	$0.22 \pm 0.10$	$0.26 \pm 0.12$
WZ	$0.07 \pm 0.03$	$0.06 \pm 0.03$	$0.07 \pm 0.03$	$0.07 \pm 0.03$	$0.04 \pm 0.02$
Total Exp.	$2.45 \pm 0.54$	$2.27 \pm 0.50$	$2.50 \pm 0.54$	$2.42 \pm 0.53$	$2.34 \pm 0.51$
Data	3	3	4	3	3
Efficiency(%)	$0.090 \pm 0.017$	$0.085 \pm 0.015$	$0.110 \pm 0.019$	$0.118 \pm 0.020$	$0.118 \pm 0.020$
Obs limit(pb)	16.5	17.4	15.7	12.2	12.2
Exp limit(pb)	13.3	14.0	10.5	9.86	9.86

Table 16: Summary of the ZH analysis with exclusive single b-tagging. Expected number of ZH events and background contributions for  $M_H = 105, 115, 125, 135$ , and  $145$  GeV, along with 95% C.L. cross-section upper limits.

DT	105 GeV	115 GeV	125 GeV	135 GeV	145 GeV
ZH	$0.083 \pm 0.015$	$0.059 \pm 0.010$	$0.046 \pm 0.008$	$0.027 \pm 0.004$	$0.015 \pm 0.002$
Zbb	$0.68 \pm 0.18$	$0.66 \pm 0.17$	$0.69 \pm 0.18$	$0.63 \pm 0.17$	$0.64 \pm 0.17$
Zjj	$0.45 \pm 0.18$	$0.49 \pm 0.19$	$0.49 \pm 0.19$	$0.41 \pm 0.16$	$0.37 \pm 0.14$
tt	$0.27 \pm 0.06$	$0.29 \pm 0.06$	$0.31 \pm 0.07$	$0.33 \pm 0.07$	$0.34 \pm 0.07$
ZZ	$0.15 \pm 0.04$	$0.16 \pm 0.04$	$0.15 \pm 0.04$	$0.14 \pm 0.04$	$0.13 \pm 0.03$
qcd	$0.058 \pm 0.026$	$0.044 \pm 0.026$	$0.088 \pm 0.052$	$0.044 \pm 0.026$	$0.088 \pm 0.052$
WZ	$0.025 \pm 0.015$	$0.016 \pm 0.010$	$0.016 \pm 0.010$	$0.008 \pm 0.005$	$0.008 \pm 0.005$
Total Exp.	$1.63 \pm 0.37$	$1.66 \pm 0.38$	$1.75 \pm 0.40$	$1.57 \pm 0.35$	$1.58 \pm 0.35$
Data	2	1	1	1	0
Efficiency(%)	$0.155 \pm 0.028$	$0.157 \pm 0.027$	$0.186 \pm 0.031$	$0.191 \pm 0.031$	$0.227 \pm 0.035$
Obs Limit(pb)	8.2	6.2	5.1	5.0	3.2
Exp Limit(pb)	6.3	6.2	5.1	5.0	4.2

Table 17: Summary of the ZH analysis with double b-tagging. Expected number of ZH events and background contributions for  $M_H = 105, 115, 125, 135$ , and  $145$  GeV, along with 95% C.L. cross-section upper limits.



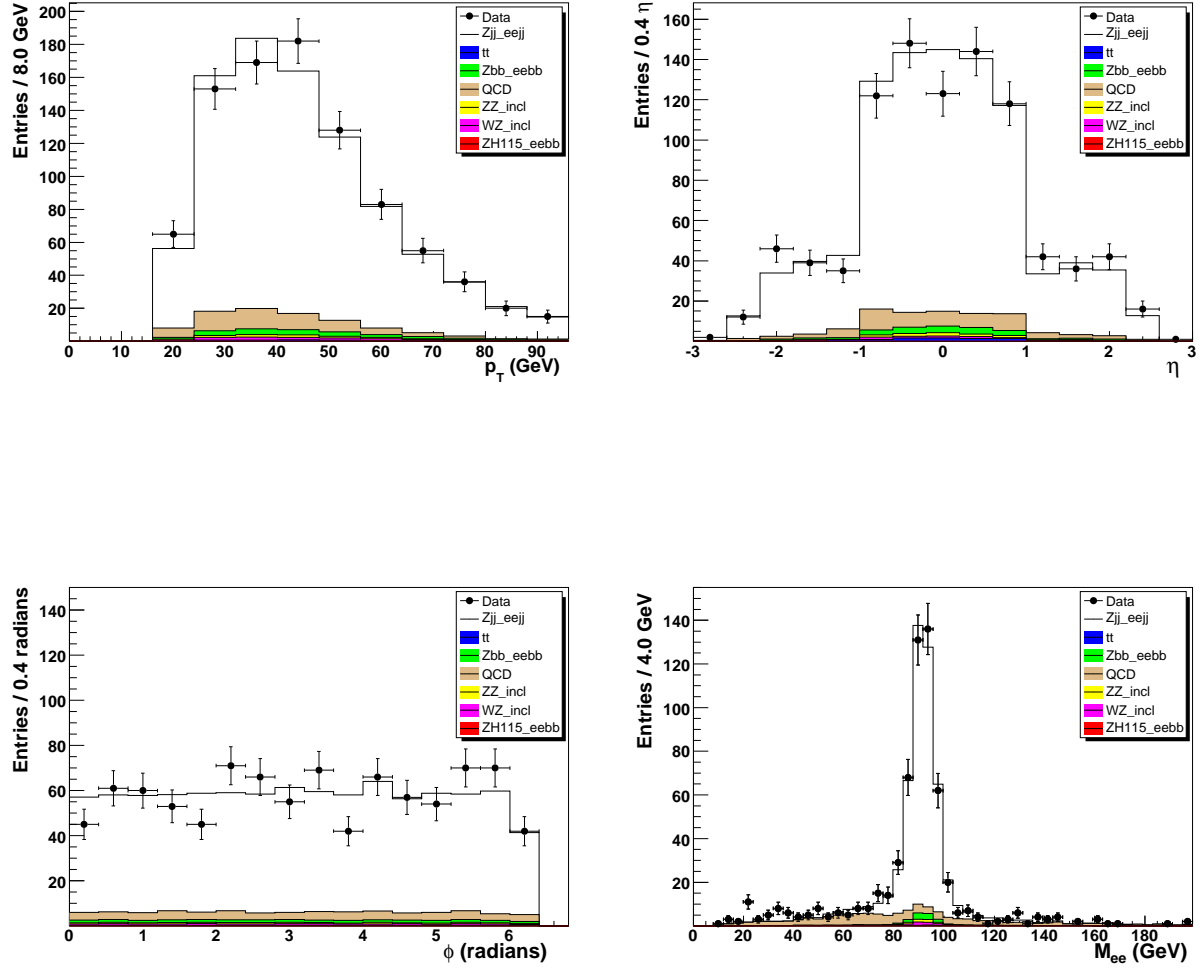


Figure 78: Kinematic distributions of the two electrons in the  $Z + \geq 2$  jet sample: a)  $p_T$  b)  $\eta$  c)  $\phi$  d) invariant mass. The simulation is normalized to the integrated luminosity of the data sample using the expected cross sections (absolute normalization). The  $Zjj$  simulation is normalized so the total number of simulated events equals the number of events in data at the  $Z + \geq 2$  jet selection cut.

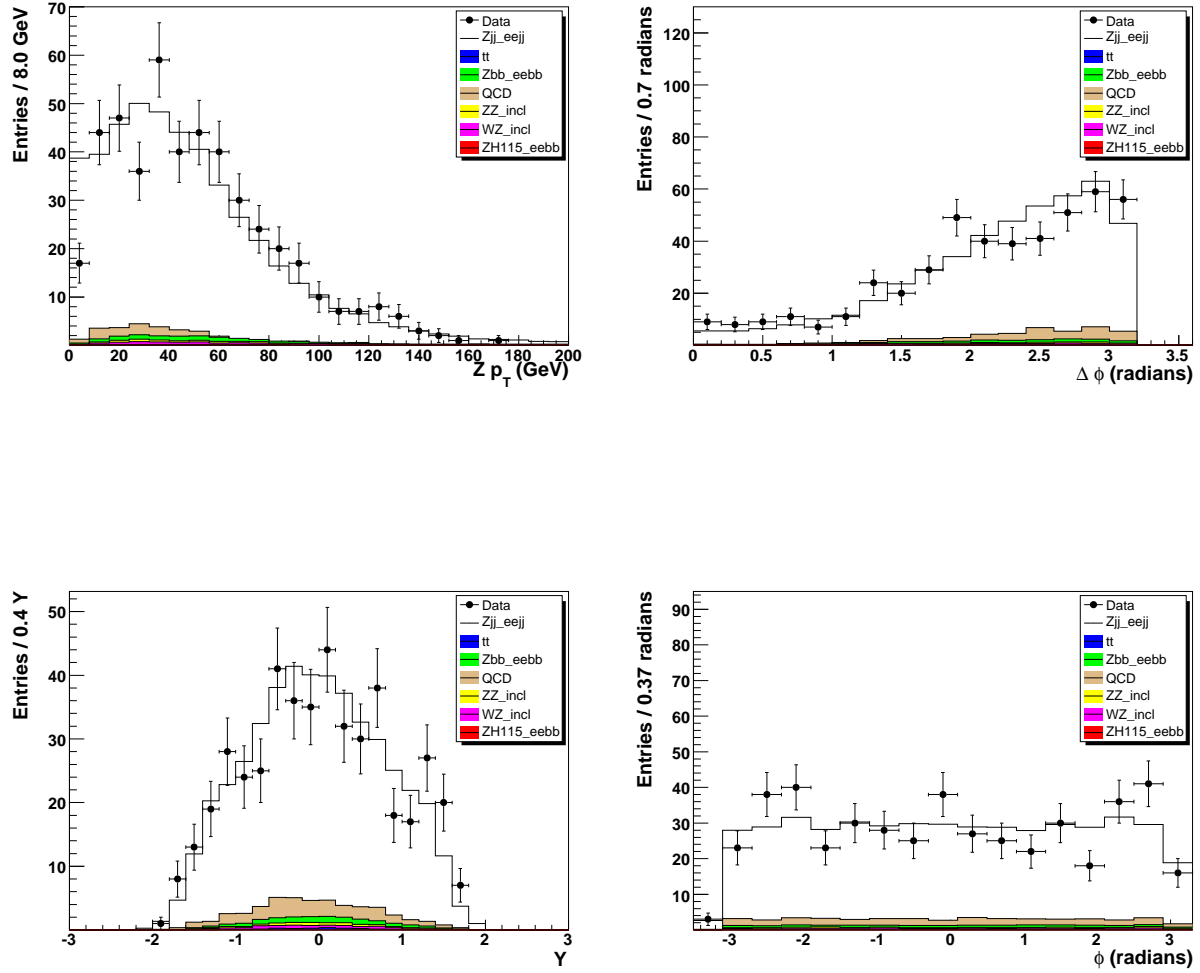


Figure 79: Kinematic distributions of the  $Z$  boson in the  $Z + \geq 2$  jet sample: a)  $p_T$  b)  $\Delta\phi$  of the 2 electrons c) Rapidity d)  $\phi$ . The simulation is normalized to the integrated luminosity of the data sample using the expected cross sections (absolute normalization). The  $Zjj$  simulation is normalized so the total number of simulated events equals the number of events in data at the  $Z + \geq 2$  jet selection cut.



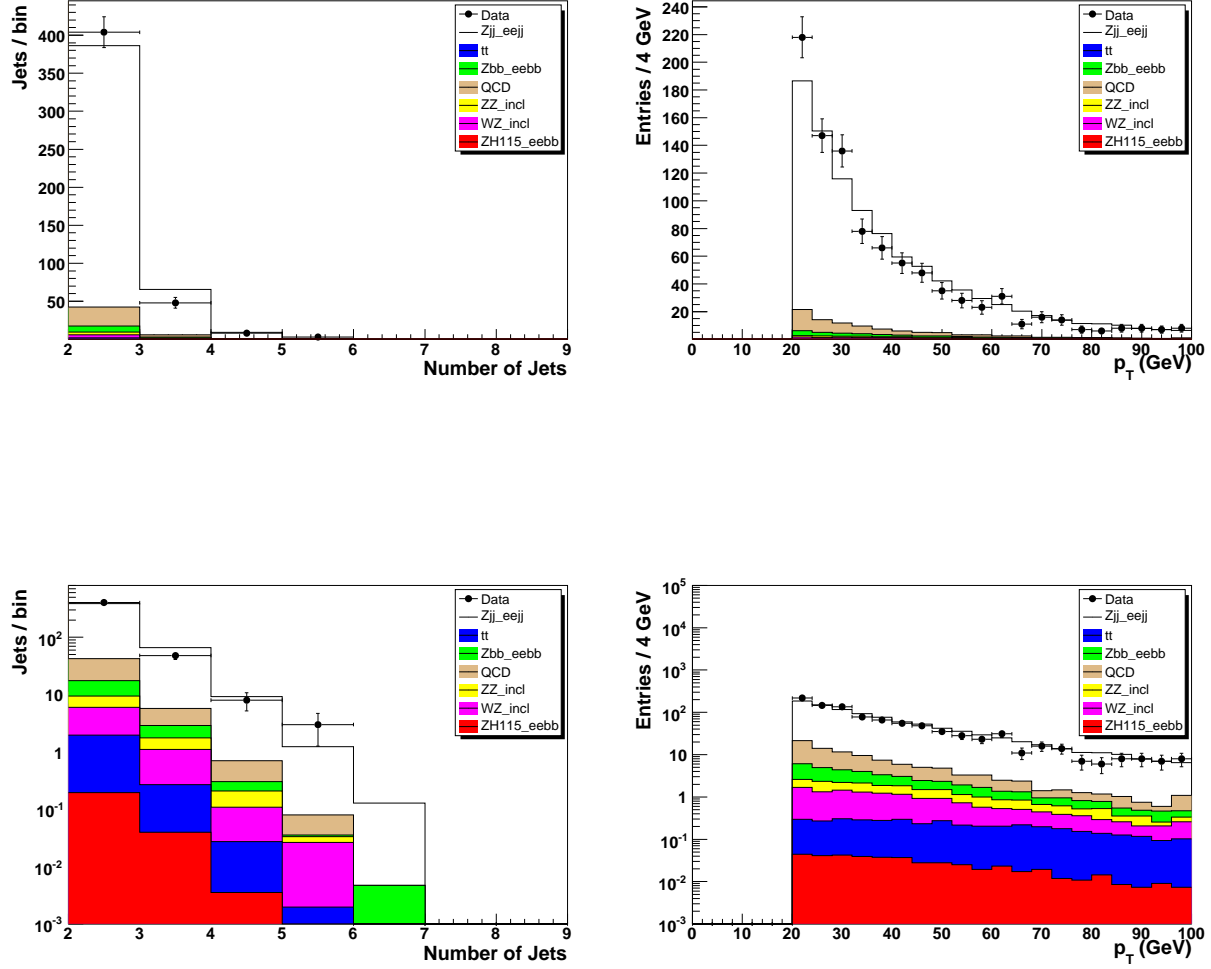


Figure 80: Distributions of the jets in the  $Z + \geq 2$  jet sample: a) number of jets b)  $p_T$  c) number of jets in the log scale d)  $p_T$  of the jets in the log scale. The simulation is normalized to the integrated luminosity of the data sample using the expected cross sections (absolute normalization). The  $Zjj$  simulation is normalized so the total number of simulated events equals the number of events in data at the  $Z + \geq 2$  jet selection cut.

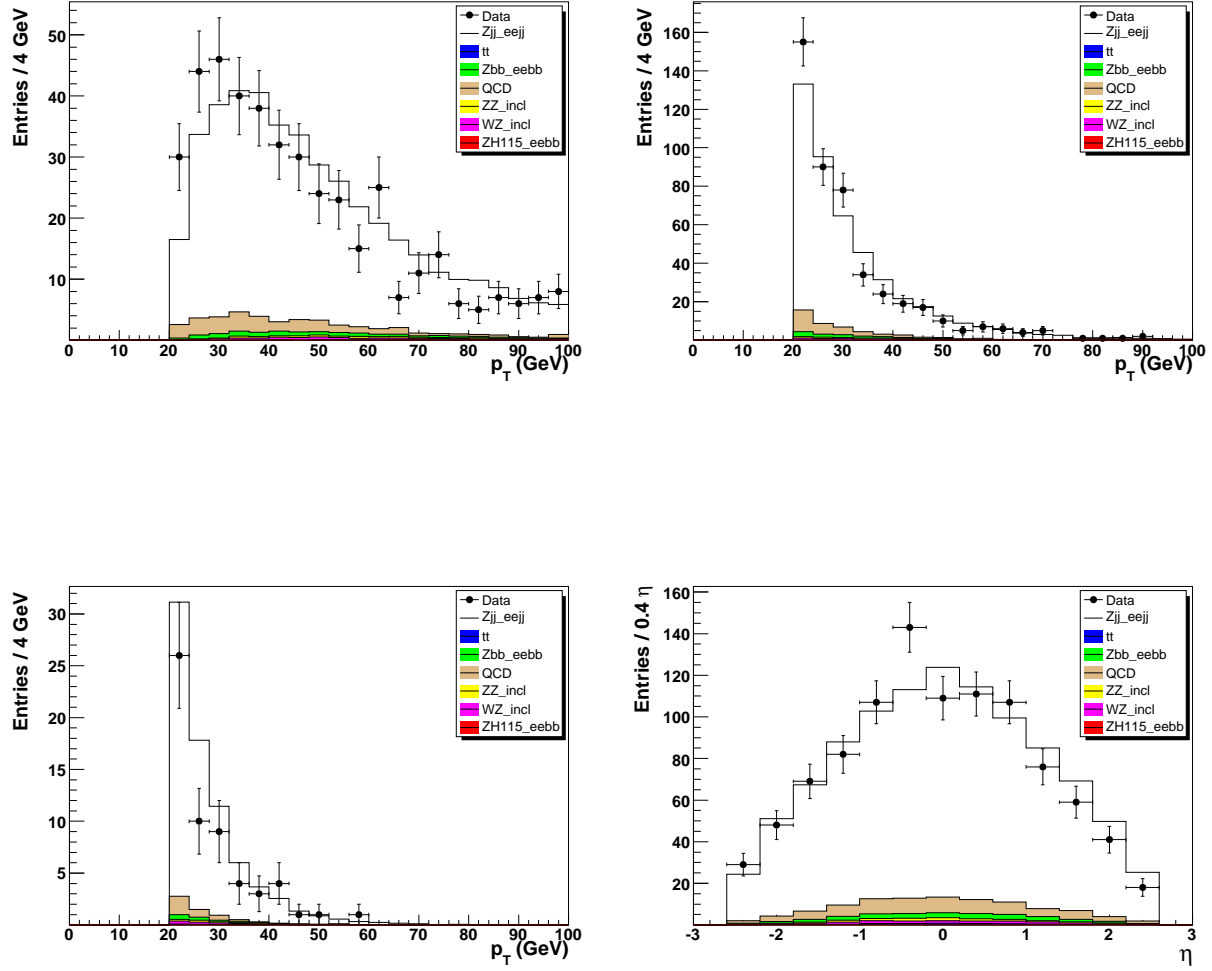


Figure 81: Distributions of the jets in the  $Z + \geq 2$  jet sample: a)  $p_T$  of leading jet b)  $p_T$  of the second jet c)  $p_T$  of the third jet (if applicable) d)  $\eta$  of all the jets. The simulation is normalized to the integrated luminosity of the data sample using the expected cross sections (absolute normalization). The  $Zjj$  simulation is normalized so the total number of simulated events equals the number of events in data at the  $Z + \geq 2$  jet selection cut.

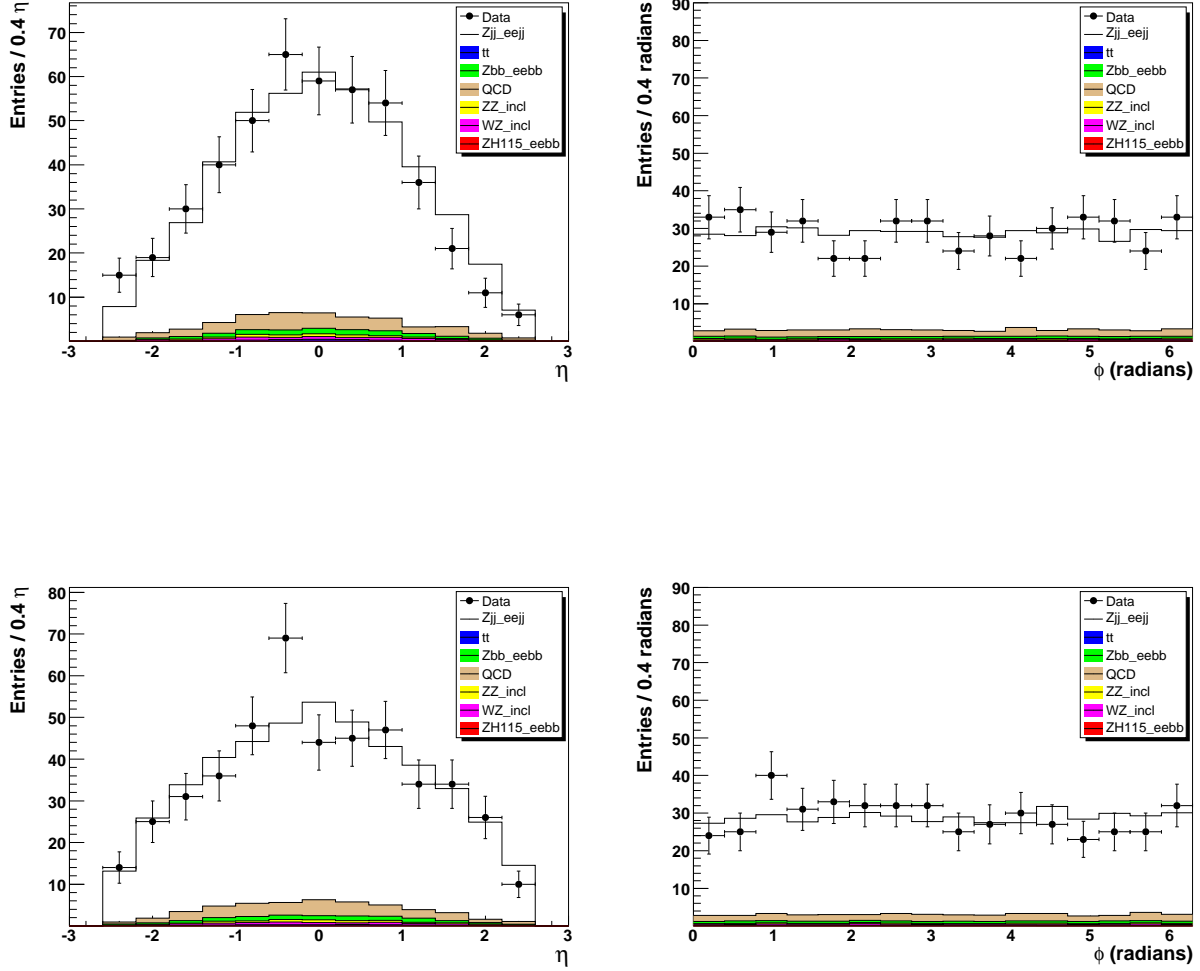


Figure 82: Distributions of the two leading jets (in  $p_T$ ) in the  $Z + \geq 2$  jet sample: a) leading jet  $\eta$  b) leading jet  $\phi$  c) second jet  $\eta$  d) second jet  $\phi$ . The simulation is normalized to the integrated luminosity of the data sample using the expected cross sections (absolute normalization). The  $Zjj$  simulation is normalized so the total number of simulated events equals the number of events in data at the  $Z + \geq 2$  jet selection cut.

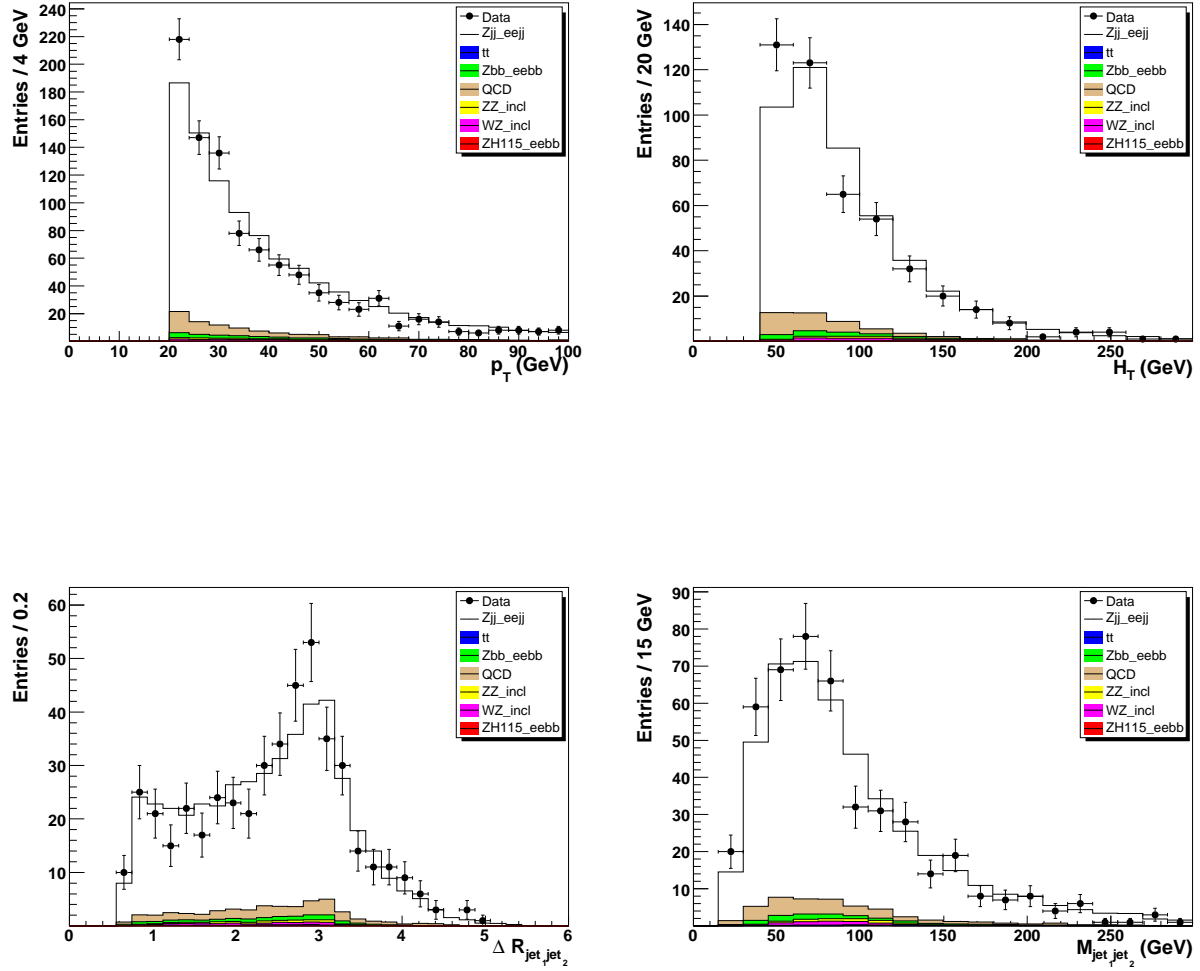


Figure 83: Distributions for the jets in the  $Z + \geq 2$  jet sample: a)  $p_T$  b)  $H_T$  c)  $\Delta R$  between the two leading jets d) invariant mass of the two leading jets. The simulation is normalized to the integrated luminosity of the data sample using the expected cross sections (absolute normalization). The  $Zjj$  simulation is normalized so the total number of simulated events equals the number of events in data at the  $Z + \geq 2$  jet selection cut.

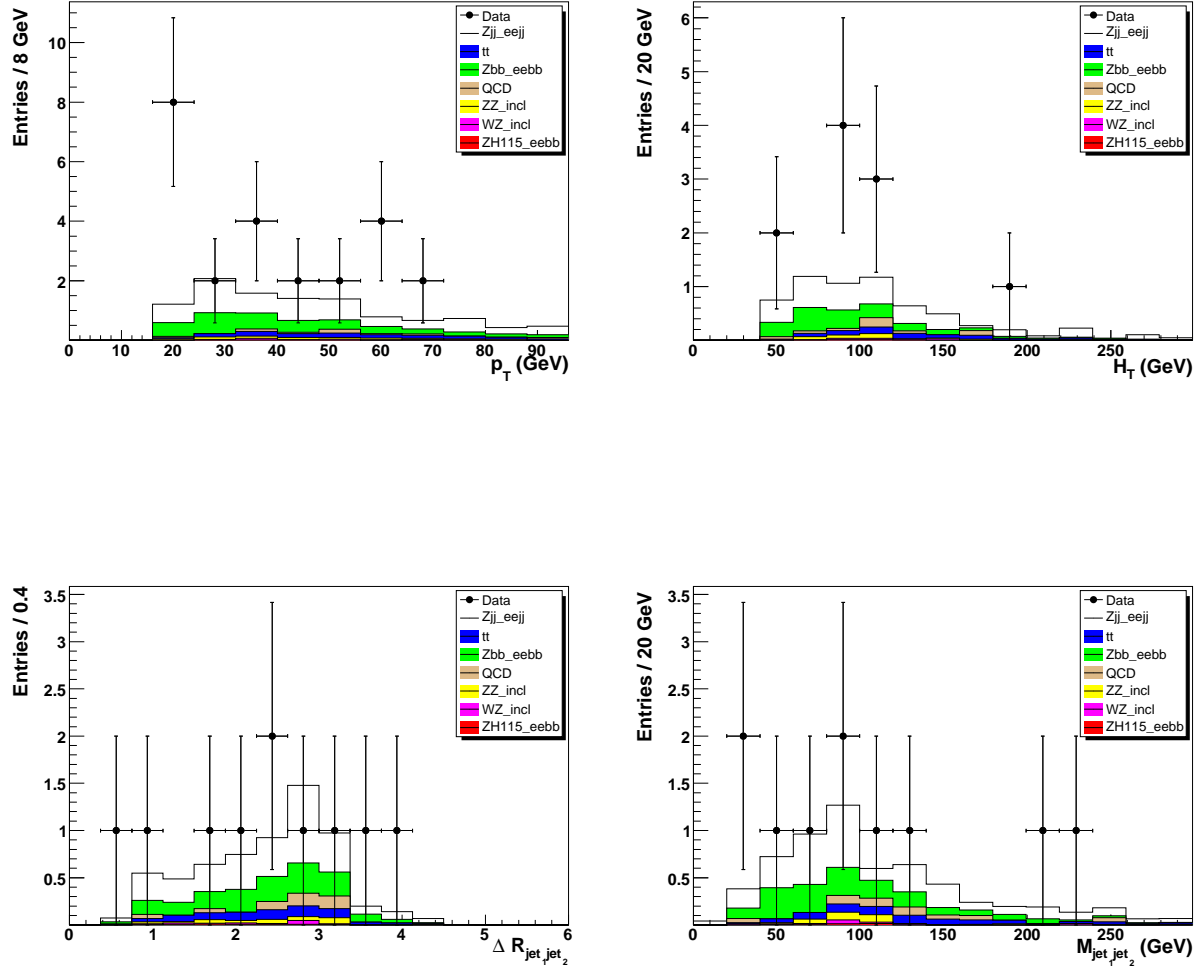


Figure 84: Distributions for the jets in the  $Z + \geq 2$  with 1 exclusive b tagged jet: a)  $p_T$  b)  $H_T$  c)  $\Delta R$  between the two leading jets d) invariant mass of the two leading jets. The simulation is normalized to the integrated luminosity of the data sample using the expected cross sections (absolute normalization). The  $Zjj$  simulation is normalized so the total number of simulated events equals the number of events in data at the  $Z + \geq 2$  jet selection cut.

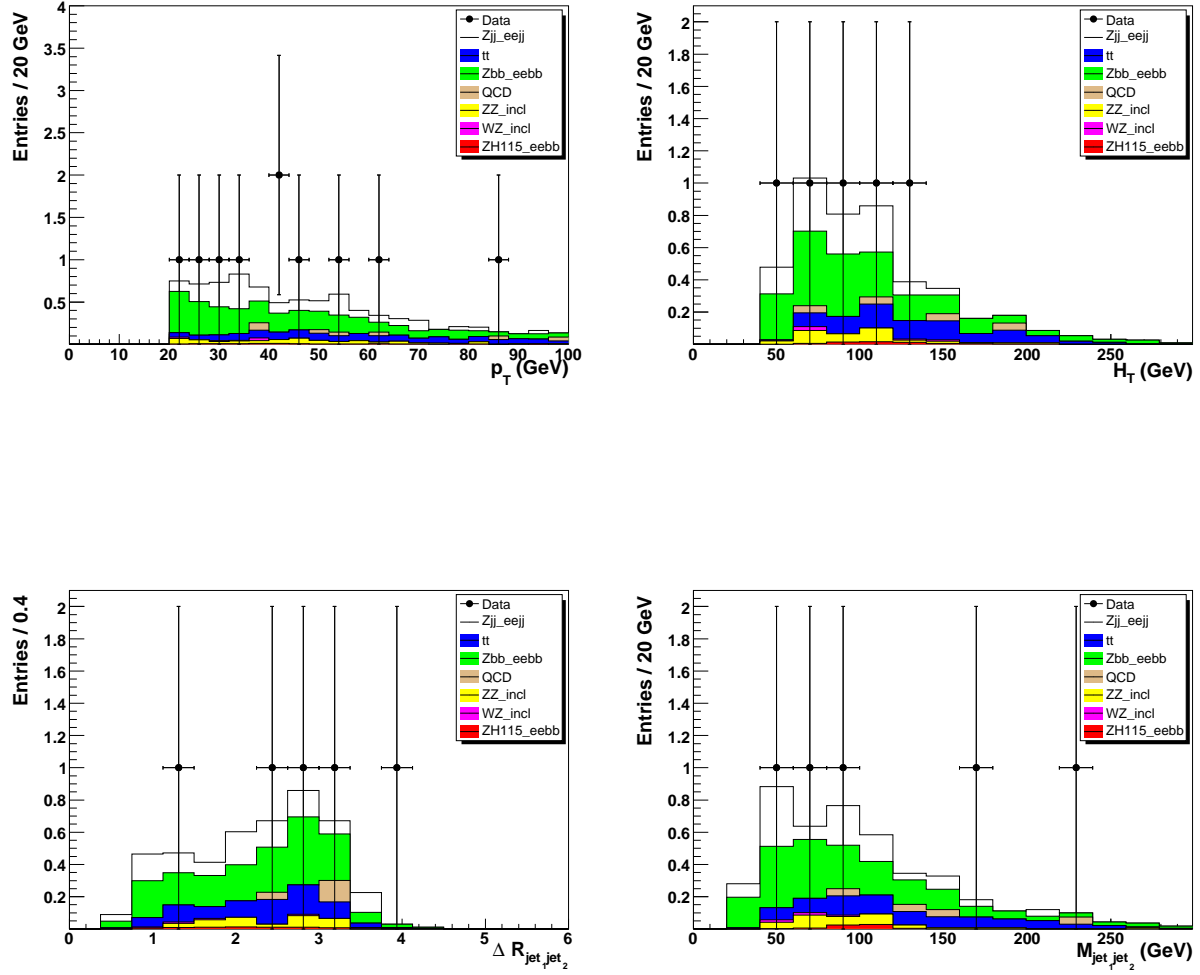


Figure 85: Distributions for the jets in the  $Z + \geq 2$  with at least 2 b tagged jets: a)  $p_T$  b)  $H_T$  c)  $\Delta R$  between the two leading jets d) invariant mass of the two leading jets. The simulation is normalized to the integrated luminosity of the data sample using the expected cross sections (absolute normalization). The  $Zjj$  simulation is normalized so the total number of simulated events equals the number of events in data at the  $Z + \geq 2$  jet selection cut.

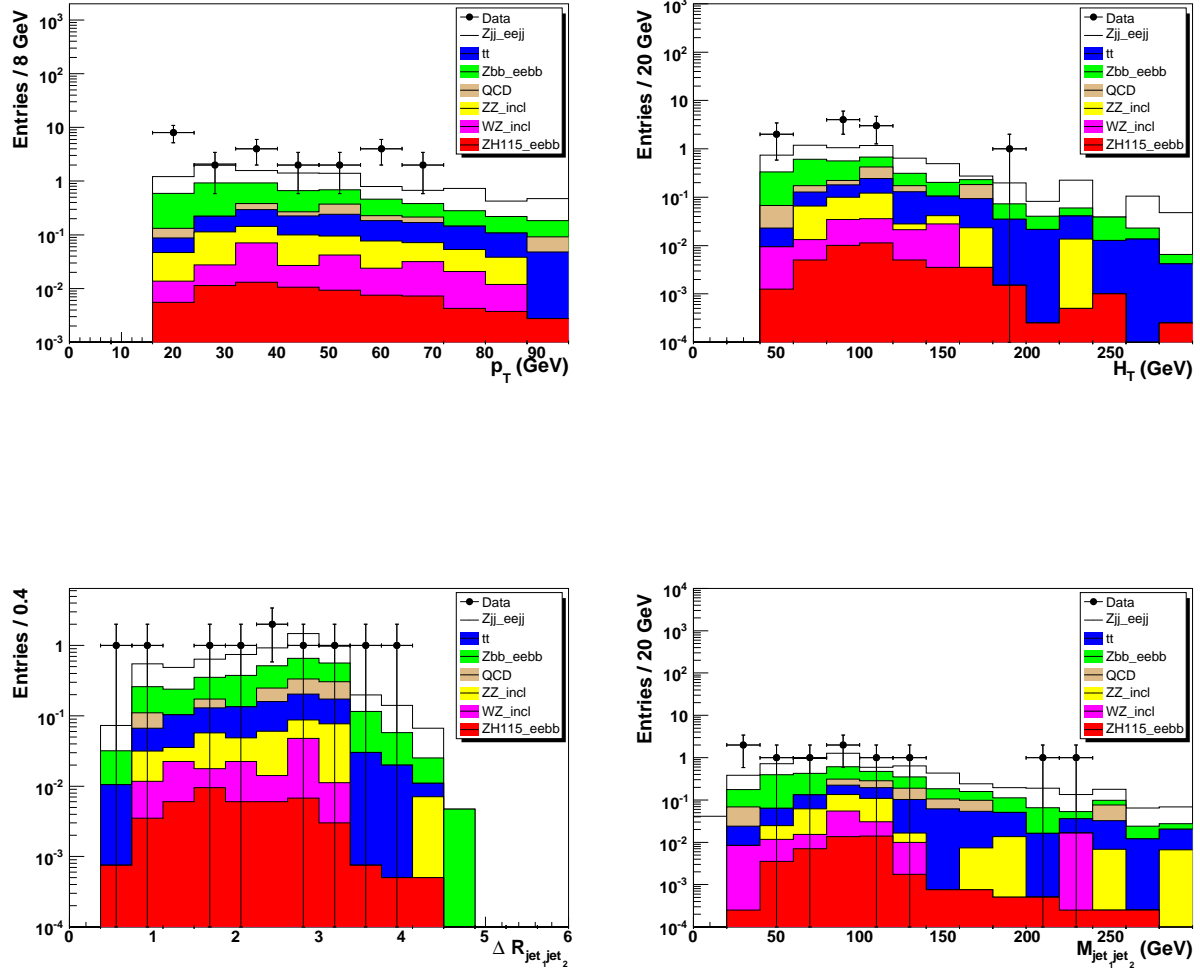


Figure 86: Distributions for the jets in the  $Z + \geq 2$  with exclusive 1 b tagged jet in the log scale: a)  $p_T$  b)  $H_T$  c)  $\Delta R$  between the two leading jets d) invariant mass of the two leading jets. The simulation is normalized to the integrated luminosity of the data sample using the expected cross sections (absolute normalization). The  $Zjj$  simulation is normalized so the total number of simulated events equals the number of events in data at the  $Z + \geq 2$  jet selection cut.

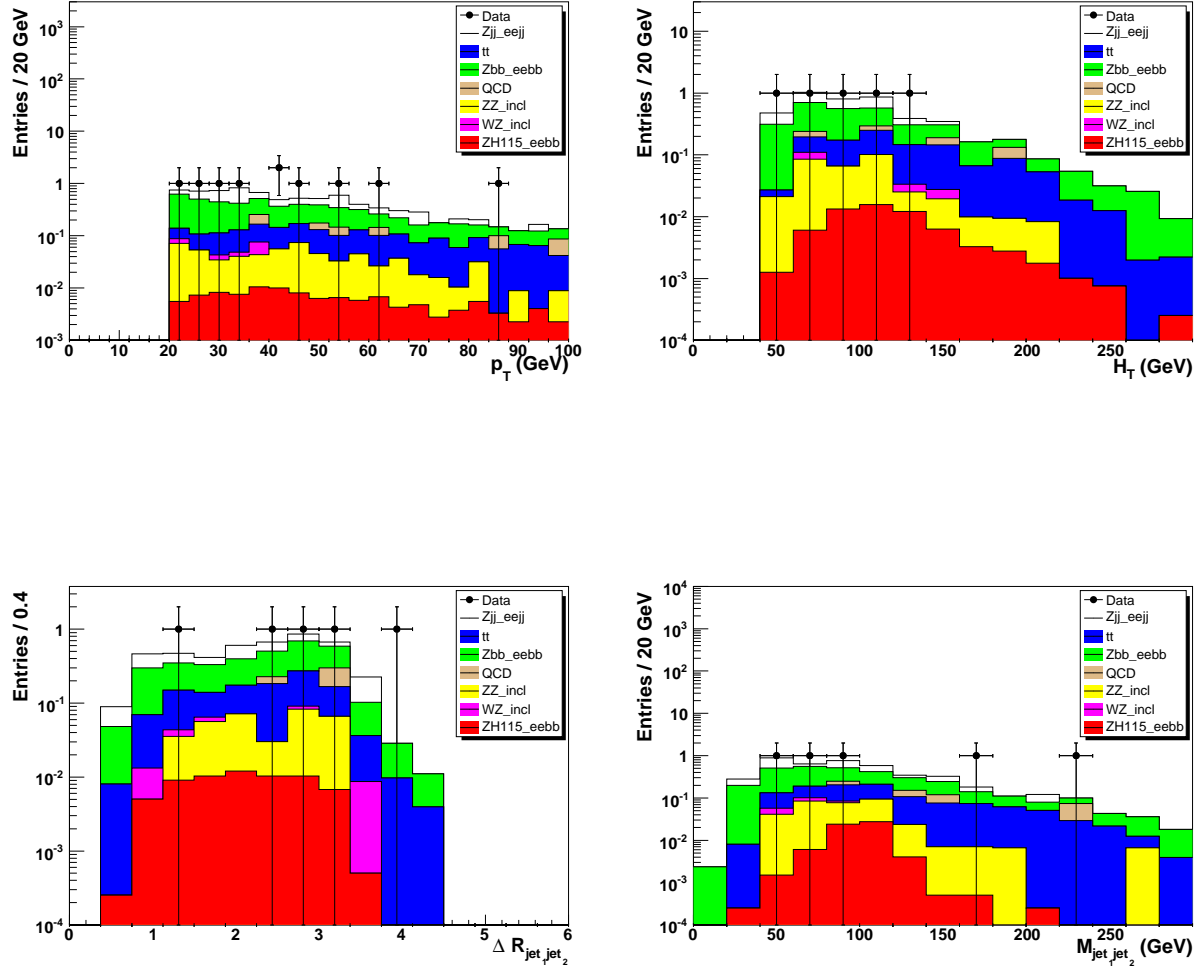


Figure 87: Distributions for the jets in the  $Z + \geq 2$  with at least 2 b tagged jets: a)  $p_T$  b)  $H_T$  c)  $\Delta R$  between the two leading jets d) invariant mass of the two leading jets. The simulation is normalized to the integrated luminosity of the data sample using the expected cross sections (absolute normalization). The  $Zjj$  simulation is normalized so the total number of simulated events equals the number of events in data at the  $Z + \geq 2$  jet selection cut.



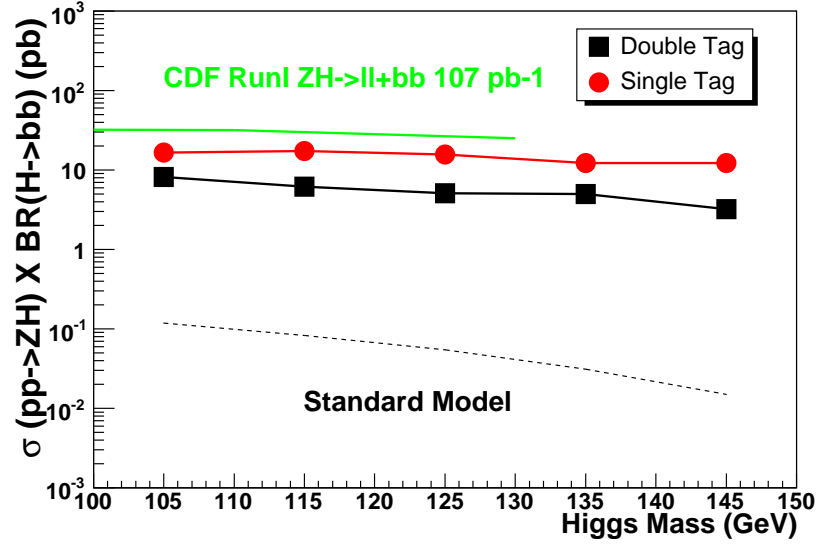


Figure 88: 95% Cross Section upper limit for exclusive single b tag and double b tag. These cross section limits are compared to standard model expectations and a CDF RunI combined lepton result.

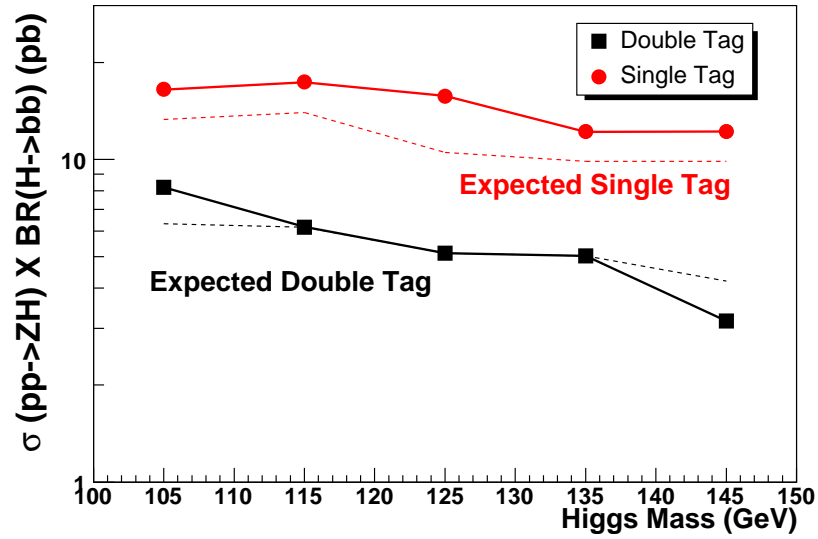
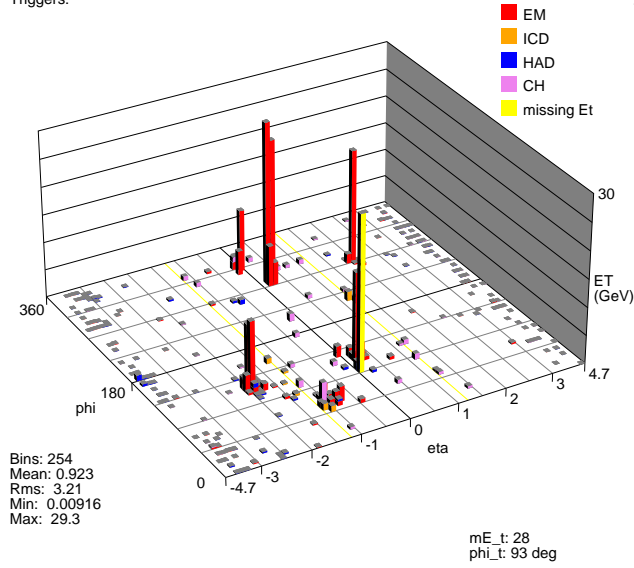


Figure 89: 95% Cross Section upper limit for exclusive single b tag and double b tag. The measured and expected confidence levels are compared.

Run 180325 Evt 6401013 Thu Aug 21 12:15:47 2003

Triggers:



Run 180325 Evt 6401013 Thu Aug 21 12:15:47 2003

ET scale: 57 GeV

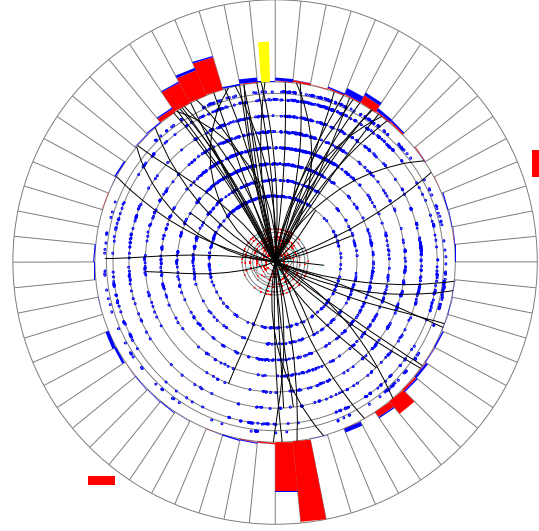
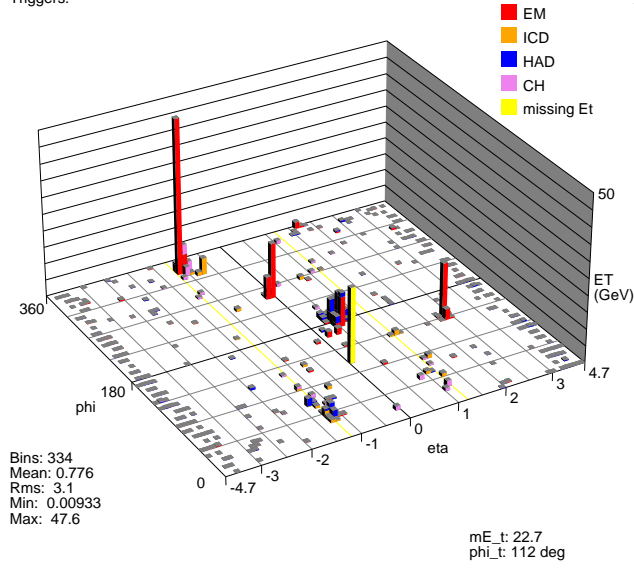


Figure 90: 1 of the 5 double b-tagged events; Di-electron Inv. Mass=100.7, Double b-jet Inv. Mass=59.3;  
 Electron1:  $p_T = 74.2$ ,  $\eta_{detector} = 0.20$ ,  $\phi_{detector} = 4.82$ , no track match;  
 Electron2:  $p_T = 30.4$ ,  $\eta_{detector} = 1.94$ ,  $\phi_{detector} = 4.77$ , track  $p_T = 33.01$ ;  
 Jet1:  $p_T = 54.9$ ,  $\eta_{detector} = 0.17$ ,  $\phi_{detector} = 1.99$ , JLIP prob.= 0.001;  
 Jet2:  $p_T = 49.8$ ,  $\eta_{detector} = -1.92$ ,  $\phi_{detector} = 2.14$ , not taggable;  
 Jet3:  $p_T = 33.6$ ,  $\eta_{detector} = -0.91$ ,  $\phi_{detector} = 1.16$ , JLIP prob.= 0.006;  
 $E_T^{miss} = 18.4$ ,  $E_T^{miss} \phi = 1.67$ ,  $PV_Z = 17.1$

Triggers:



ET scale: 61 GeV

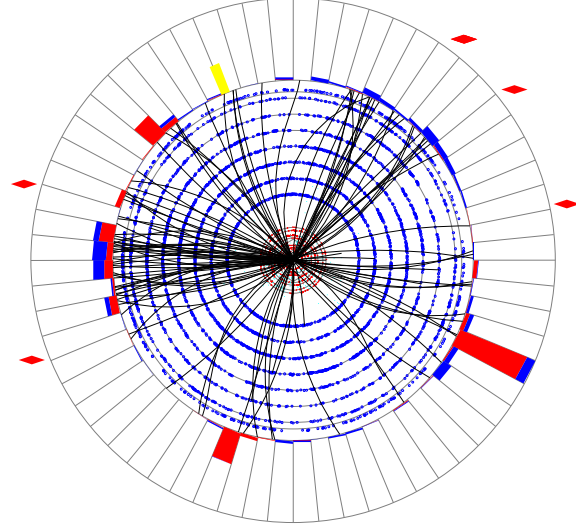
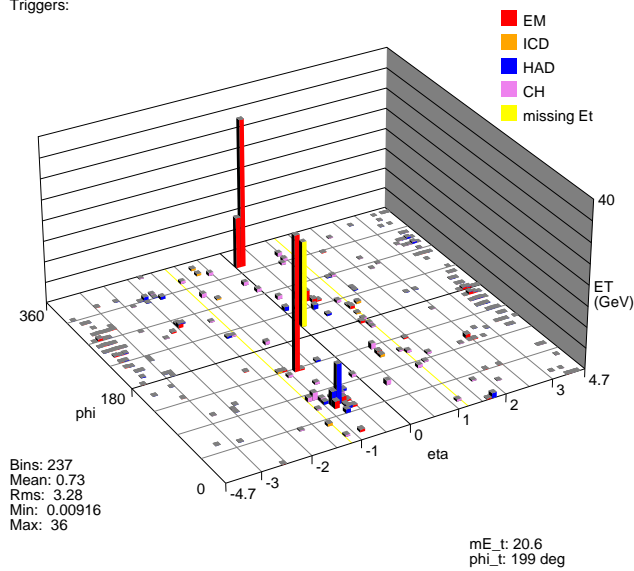


Figure 91: 2 of the 5 double b-tagged events; Di-electron Inv. Mass=87.0, Double b-jet Inv. Mass=165.4;  
 Electron1:  $p_T = 29.3$ ,  $\eta_{\text{detector}} = -0.08$ ,  $\phi_{\text{detector}} = 4.40$ , track  $p_T = 20.4$ ;  
 Electron2:  $p_T = 22.8$ ,  $\eta_{\text{detector}} = 2.37$ ,  $\phi_{\text{detector}} = 2.37$ , track  $p_T = 4.88$ ;  
 Jet1:  $p_T = 120.0$ ,  $\eta_{\text{detector}} = -1.09$ ,  $\phi_{\text{detector}} = 5.99$ , not taggable;  
 Jet2:  $p_T = 86.9$ ,  $\eta_{\text{detector}} = 0.50$ ,  $\phi_{\text{detector}} = 3.23$ , JLIP prob. = 0.001;  
 Jet3:  $p_T = 41.1$ ,  $\eta_{\text{detector}} = -1.18$ ,  $\phi_{\text{detector}} = 0.91$ , JLIP prob.= 0.001;  
 $E_T^{\text{miss}} = 21.7$ ,  $E_T^{\text{miss}} \phi = 2.15$ ,  $PV_Z = -25.6$

Triggers:



ET scale: 51 GeV

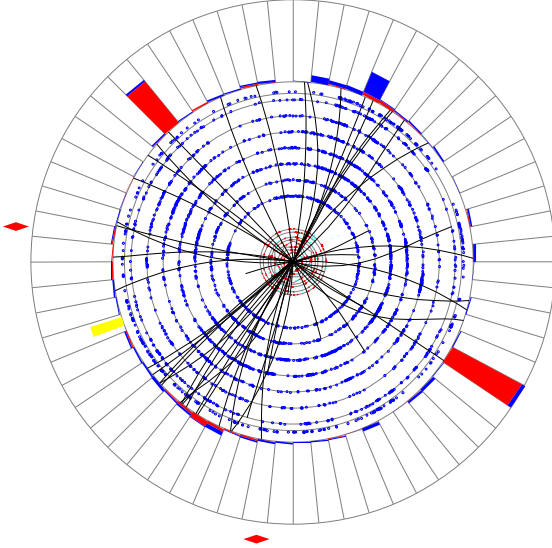
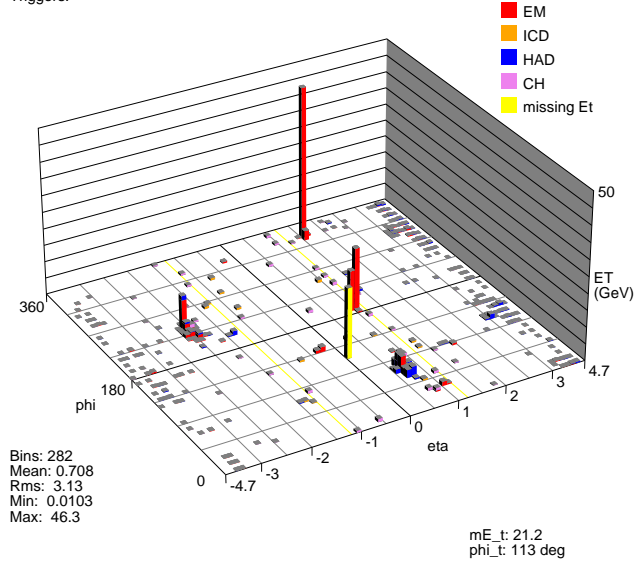


Figure 92: 3 of the 5 double b-tagged events; Di-electron Inv. Mass=88.7, Double b-jet Inv. Mass=83.8;  
 Electron1:  $p_T = 53.2$ ,  $\eta_{\text{detector}} = 0.10$ ,  $\phi_{\text{detector}} = 5.72$ , track  $p_T = 35.5$ ;  
 Electron2:  $p_T = 31.6$ ,  $\eta_{\text{detector}} = -0.83$ ,  $\phi_{\text{detector}} = 2.31$ , track  $p_T = 23.9$ ;  
 Jet1:  $p_T = 43.3$ ,  $\eta_{\text{detector}} = -0.72$ ,  $\phi_{\text{detector}} = 1.21$ , JLIP prob.= 0.002;  
 Jet2:  $p_T = 28.9$ ,  $\eta_{\text{detector}} = 0.48$ ,  $\phi_{\text{detector}} = 4.25$ , JLIP prob.= 0.026;  
 $E_T^{\text{miss}} = 10.4$ ,  $E_T^{\text{miss}} \phi = 3.01$ ,  $PV_Z = 29.9$

Run 195216 Evt 4668207 Fri Jul 16 13:10:55 2004

Triggers:



Run 195216 Evt 4668207 Fri Jul 16 13:10:55 2004

ET scale: 49 GeV

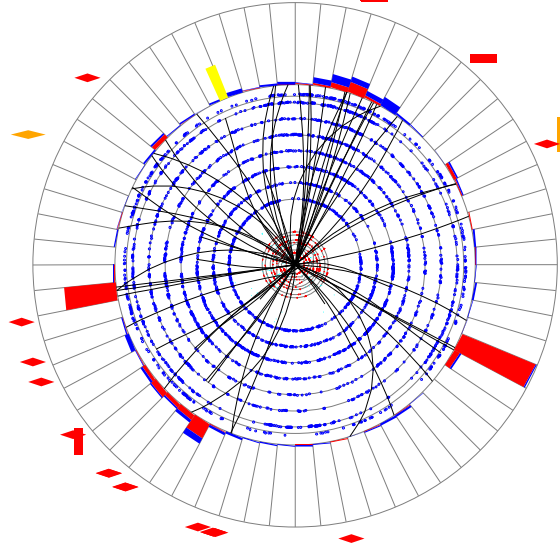
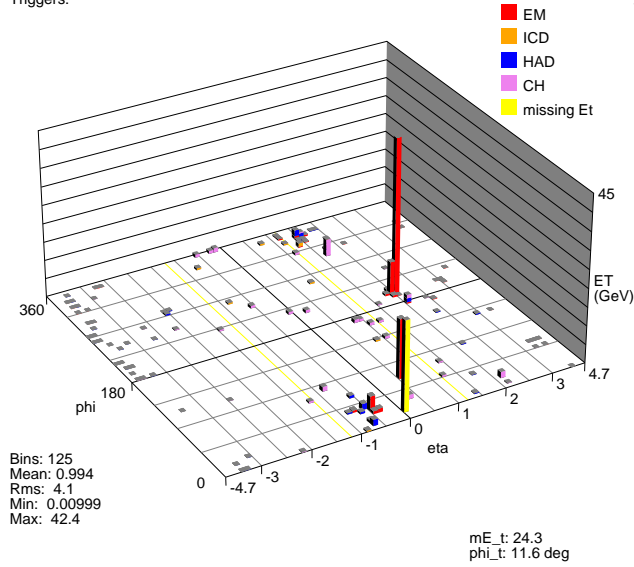


Figure 93: 4 of the 5 double b-tagged events; Di-electron Inv. Mass=85.3, Double b-jet Inv. Mass=223;  
 Electron1:  $p_T = 52.5$ ,  $\eta_{detector} = 1.55$ ,  $\phi_{detector} = 5.81$ , tracks  $p_T = 34.4$ ;  
 Electron2:  $p_T = 34.8$ ,  $\eta_{detector} = 1.00$ ,  $\phi_{detector} = 3.28$ , track  $p_T = 26.3$ ;  
 Jet1:  $p_T = 63.0$ ,  $\eta_{detector} = 0.69$ ,  $\phi_{detector} = 1.29$ , JLIP prob.= 0.006;  
 Jet2:  $p_T = 44.8$ ,  $\eta_{detector} = -2.01$ ,  $\phi_{detector} = 4.17$ , JLIP prob.= 0.036;  
 $E_T^{miss} = 14.7$ ,  $E_T^{miss} \phi = 2.07$ ,  $PV_Z = -3.2$

Run 164383 Evt 3680302 Fri Sep 20 00:34:16 2002

Triggers:



Run 164383 Evt 3680302 Fri Sep 20 00:34:16 2002

ET scale: 53 GeV

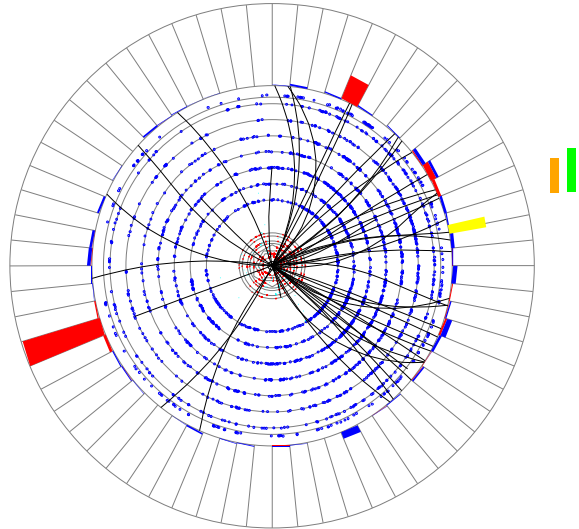


Figure 94: 5 of the 5 double b-tagged events; Di-electron Inv. Mass=89.6, Double b-jet Inv. Mass=65.4;  
 Electron1:  $p_T = 62.7$ ,  $\eta_{detector} = 2.02$ ,  $\phi_{detector} = 3.49$ , track  $p_T = 433$ ;  
 Electron2:  $p_T = 20.0$ ,  $\eta_{detector} = 0.55$ ,  $\phi_{detector} = 1.13$ , track  $p_T = 19.2$ ;  
 Jet1:  $p_T = 26.2$ ,  $\eta_{detector} = -0.52$ ,  $\phi_{detector} = 0.61$ , JLIP prob.= 0.020;  
 Jet2:  $p_T = 20.7$ ,  $\eta_{detector} = 1.51$ ,  $\phi_{detector} = 6.03$ , JLIP prob.= 0.026;  
 $E_T^{miss} = 18.6$ ,  $E_T^{miss} \phi = 0.96$ ,  $PV_Z = 12.4$

## 7 Conclusion

We have searched for the SM Higgs boson in the channel  $ZH \rightarrow e^+e^-b\bar{b}$  using 452  $\text{pb}^{-1}$  of data taken between April 2002 and August 2004. The number of events with a  $Z$  boson and at least two taggable jets in which one of the jets has been b-tagged has been measured with the Jet Lifetime Probability (JLIP) algorithm, yielding 10 events with an expectation from SM processes of  $6 \pm 1$  events. The exclusive single b-tag production rate is consistent with the simulated expectation and the kinematic distributions of these events are reasonably described by the simulation.

The number of events with a  $Z$  boson and two b-tagged jets has been measured, yielding 5 events with an expectation from SM processes of  $4 \pm 1$ . The double b-tag production rate is consistent with the simulated expectation, and the kinematic distributions of these events are reasonably described by the simulation.

The 95% C.L. upper limit on the Higgs boson cross section,  $\sigma(p\bar{p} \rightarrow ZH) \times \text{B}(H \rightarrow b\bar{b})$ , in which the two b jets are required to have  $p_T > 20 \text{ GeV}$ ,  $\eta < 2.5$ , and a dijet mass window of  $\pm 1.5\sigma \text{ GeV}$  around the reconstructed Higgs mass is between 3.2 and 8.2 pb (double tagged) and 12.2 to 17.4 pb (exclusive single tagged) for Higgs masses between 105 and 145 GeV.

## 8 Acknowledgments

We would like to thank the Higgs convenors Gregorio Bernardi and Su Yong Choi for their guidance. We appreciate the fruitful discussions with Kazu Hanagaki and his contributions throughout this analysis. We would also like to thank Su Yong Choi for the Athena rootuple maker and months of collaboration on this analysis. We are deeply indebted to Marc Buehler whose polished analysis code and tools were the foundation of this analysis.

## References

- [1] ALEPH Collaboration et al.: “Precision Electroweak Measurements on the Z Resonance”, hep-ph/0509008.
- [2] Anderson, Barberis, et al. DØ Note 5060.
- [3] Suyong. [http://www-d0.fnal.gov/~suyong/d0\\_private/athenaweb/athena.htm](http://www-d0.fnal.gov/~suyong/d0_private/athenaweb/athena.htm).
- [4] Luminosity ID group:[http://www-d0.fnal.gov/phys\\_id/luminosity/data\\_access](http://www-d0.fnal.gov/phys_id/luminosity/data_access).
- [5] Anderson, Barberis, et al. DØ Note 4116.
- [6] Top Production Group. “Measurement of the  $t\bar{t}$  Production Cross-section at  $\sqrt{s} = 1.96$  TeV in the Muon+jets Final State using a Topological Method” 09 Aug 2004.
- [7] <http://www-d0.fnal.gov/Run2Physics/cs/index.html>.
- [8] Trigger lists: [http://www-d0.fnal.gov/trigger\\_meister/private/www/tl\\_desc/global.html](http://www-d0.fnal.gov/trigger_meister/private/www/tl_desc/global.html).
- [9] MCFM - Monte Carlo for FeMtobarn processes: <http://mcfm.fnal.gov>.
- [10] MCFM Cross-Sections for CAPS Production: [http://www-clued0.fnal.gov/~nunne/cross-sections/caps\\_xsect.html](http://www-clued0.fnal.gov/~nunne/cross-sections/caps_xsect.html).
- [11] MCFM Cross Sections: [http://www-clued0.fnal.gov/~nunne/cross-sections/mcfm\\_cross-sections.html](http://www-clued0.fnal.gov/~nunne/cross-sections/mcfm_cross-sections.html).
- [12] M. Ciccolini, S. Dittmaier, M. Kramer: Electroweak Radiative Corrections to Associated WH and ZH Production at Hadron Colliders, hep-ph/0306234.
- [13] M.Mangano et al.: ALPGEN, a generator for hard multiparton processes in hadron collisions, hep-ph/0206293.
- [14] Vlimant, Bassler, Bernardi, Trincaz-Duvoid, DØ Note 4146.
- [15] Busato, Andrieu, DØ Note 4457 13 AUG 2004.
- [16] Stone. <http://www-clued0.fnal.gov/~alstone/D0Work/Athena/lumi/lumi.html>.
- [17] Jain, DØ Note 4402.
- [18] Agelou *et al.*, DØ Note 4419.
- [19] Mrenna. [http://cepa.fnal.gov/personal/mrenna/Matched\\_Dataset\\_Description.html](http://cepa.fnal.gov/personal/mrenna/Matched_Dataset_Description.html).
- [20] Casilum, Hirosky, DØ Note 3324.
- [21] Abbott, et al. “High  $p_T$  jets in  $p\bar{p}$  collisions at  $\sqrt{s}=630$  and 1800 GeV” Fermi-Pub-00/216-E.
- [22] Rani, DØ Note 4363.

- [23] Hanagaki, DØ Note 4479.
- [24] Gollub. “Jet reco\*ID scale factor for top analyze” CALGO meeting 11 JAN 2005.
- [25] [http://dzero.phy.uic.edu/james/higgs/smear\\_track\\_pt/index.html](http://dzero.phy.uic.edu/james/higgs/smear_track_pt/index.html)
- [26] Heinmiller, DØ Note 4837.
- [27] Gerber, Chabablina, Garzon, DØ Note 4995.
- [28] [http://dzero.phy.uic.edu/james/higgs/taggability\\_study.html](http://dzero.phy.uic.edu/james/higgs/taggability_study.html).
- [29] Block, DØ Note 4069.
- [30] R. Bonciani, et al. Nucl. Physics. B 529(1998) 424, M. Cacciari, et al. JHEP 0404(2004) 068, N. Kidonakis, R. Vogt, Phys. Rev. D 68 (2003) 114014.
- [31] D. Acosta et al. (CDF collaboration), Phys. Rev. Letters 94, 211801 (2005).
- [32] J. Campbell et al., Production of a Z boson and two jets with one heavy-quark tag, hep-ph/0510362 (2005).
- [33] T. Sjostrand et al., “PYTHIA 6.3 Physics and Manual”, hep-ph/0308153 (2003).
- [34] I. Bertram et al., Fermilab-TM-2104 (2000).
- [35] ALEPH Collaboration, D. Decamp *et al.*, Phys. Lett. B **592**, 1-4 (2004).
- [36] D. Acosta *et al.*, The CDF Collaboration, “Search for Higgs Bosons Decaying into  $b\bar{b}$  and Produced in Association with a Vector Boson in  $p\bar{p}$  Collisions at  $\sqrt{s} = 1.8$  TeV”, Phys. Rev. Lett. 95, 051801 (2005).

## 9 Appendix

The two leading electrons and jets  $p_T$  distributions for a MC Higgs signal sample,  $ZH_{115}$ , and the largest background,  $Zbb$ , are shown to compare the distributions of these two samples and to estimate an event scale factor. Using the electron distributions, Figures 95 and 96, jet distributions, Figures 97 and 98, and the 1-D scale factors (versus  $p_T$ ), event scale factors can be estimated. No scale factors were applied in the electron and jet distributions. A summary of the average event scale factors from  $ZH_{115}$  and  $Zbb$  MC samples are shown in table 18.

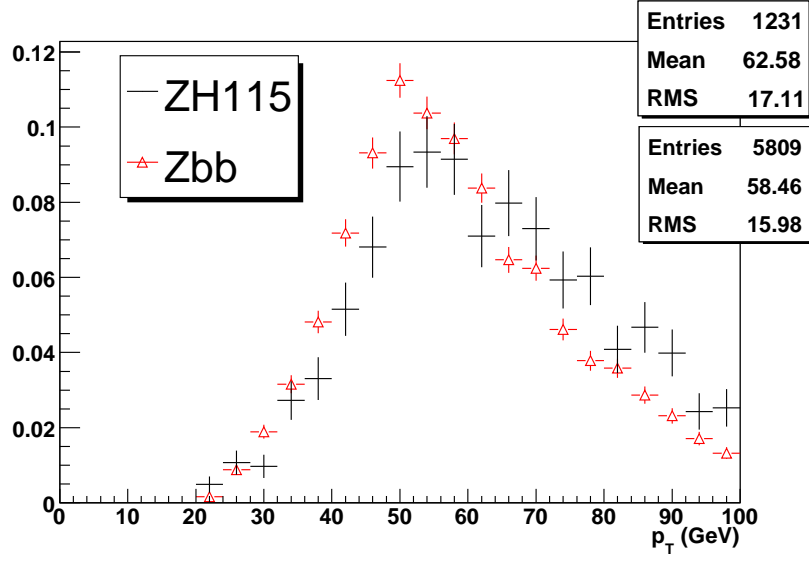


Figure 95: The leading electron  $p_T$  distribution for events with two or more jets without any scale factor applied for the signal  $ZH$ , with a Higgs mass of 115 GeV, and for the largest background  $Zbb$ . Estimated efficiencies and scale factors can be evaluated from the mean of the leading and second leading electron  $p_T$  distributions.

Selection cut	$ZH_{115}$	$Zbb$
Trigger	100%	100%
2 Electrons	89%	88%
1 Track Match	97%	97%
2 Jets	89%	83%
2 taggable	83%	77%
2 b tagged	77%	74%

Table 18: Average event scale factor for  $ZH_{115}$  and  $Zbb$ .



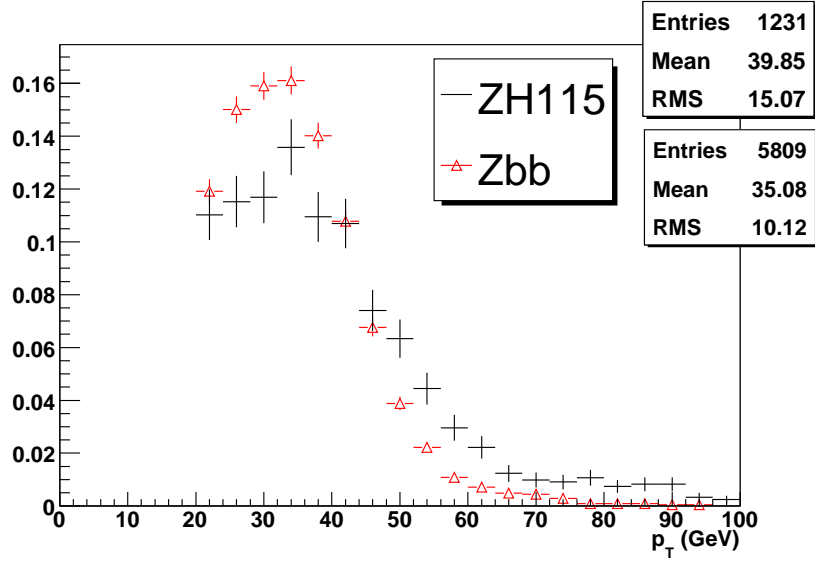


Figure 96: The second electron  $p_T$  distribution for events with two or more jets without any scale factor applied for the signal  $ZH$ , with a Higgs mass of 115 GeV, and the largest background  $Zbb$ . Estimated efficiencies and scale factors can be evaluated from the mean of the leading and second leading electron  $p_T$  distributions.

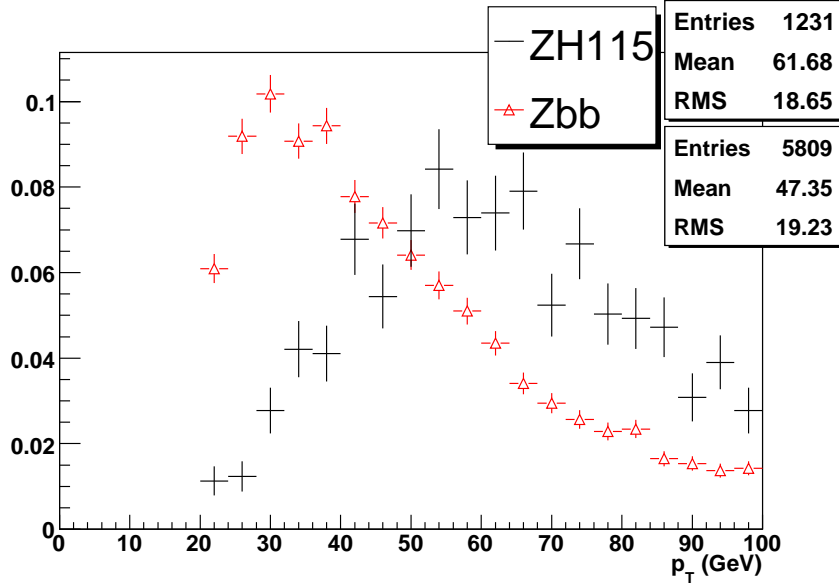


Figure 97: Leading jet  $p_T$  distributions for signal  $ZH_{115}$  MC and the largest background  $Zbb$ . The MC scale factors have not been applied and the distributions are chosen after the  $Z$  boson mass cut with two or more jets. The two distributions are normalized to unity.

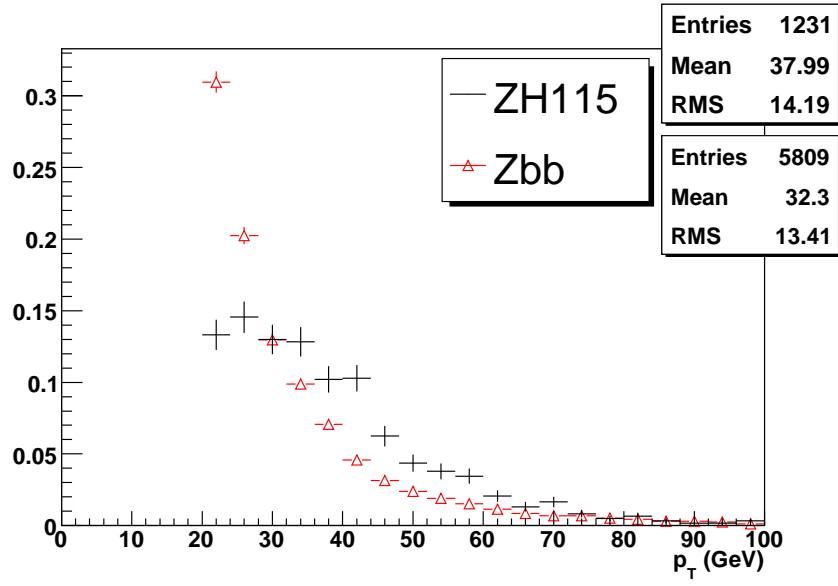


Figure 98: The second leading jet  $p_T$  distributions for signal  $ZH_{115}$  MC and the largest background  $Zbb$ . The MC scale factors have not been applied and the distributions are chosen after the  $Z$  boson mass cut with two or more jets. The two distributions are normalized to unity.